2015-05-04

Automated Brain Lesion Detection and Segmentation Using Magnetic Resonance Images

Nooshin Nabizadeh
University of Miami, nooshin.zade@gmail.com

Recommended Citation

Nabizadeh, Nooshin, "Automated Brain Lesion Detection and Segmentation Using Magnetic Resonance Images" (2015). *Open Access Dissertations*. 1409.
https://scholarlyrepository.miami.edu/oa_dissertations/1409

UNIVERSITY OF MIAMI

AUTOMATED BRAIN LESION DETECTION AND SEGMENTATION USING MAGNETIC RESONANCE IMAGES

By

Nooshin Nabizadeh

A DISSERTATION

Submitted to the Faculty
of the University of Miami
in partial fulfillment of the requirements for
the degree of Doctor of Philosophy

Coral Gables, Florida

May 2015

UNIVERSITY OF MIAMI

A dissertation submitted in partial fulfillment of
the requirements for the degree of
Doctor of Philosophy

AUTOMATED BRAIN LESION DETECTION AND SEGMENTATION USING MAGNETIC RESONANCE IMAGES

Nooshin Nabizadeh

Approved:

Miroslav Kubat, Ph.D. Associate Professor of Electrical and Computer Engineering	Kamal Premaratne, Ph.D. Professor of Electrical and Computer Engineering
Mei-Ling Shyu, Ph.D. Professor and Associate Chair of Electrical and Computer Engineering	Nigel John, Ph.D. Lecturer of Electrical and Computer Engineering
Pradip Pattany, Ph.D. Research Associate Professor of Radiology	M. Brian Blake, Ph.D. Dean of the Graduate School

NABIZADEH, NOOSHIN (Ph.D., Electrical and Computer Engineering)

Automated Brain Lesion Detection and Segmentation Using Magnetic Resonance Images (May 2015)

Abstract of a dissertation at the University of Miami.

Dissertation supervised by Professor Miroslav Kubat.
No. of pages in text. (175)

Automated segmentation of brain lesions in magnetic resonance images (MRI) is a difficult procedure due to the variability and complexity of the location, size, shape, and texture of these lesions. In this study, four algorithms for brain lesion detection and segmentation using MRI are proposed. In the ***first algorithm***, an automatic algorithm for brain stroke lesion detection and segmentation using single-spectral MRI is proposed, which is called histogram-based gravitational optimization algorithm (HGOA). HGOA is a novel intensity-based segmentation technique that applies enhanced gravitational optimization algorithm on histogram analysis results to segment the brain lesion. The ischemic stroke lesions are segmented with 91.5% accuracy and tumor lesions are segmented with 88% accuracy.

Since histogram analysis limits the extracted information to the number of pixels in specific gray levels and does not include any region based information, the accuracy of a histogram-based method is limited. In the ***second algorithm***, in order to increase the accuracy of brain tumor segmentation, a texture-based automated approach is presented. The experimental results on T1-weighted, T2-weighted, and fluid-attenuated inversion recovery (FLAIR) images on both simulated and real brain MRI data prove the efficacy of our technique in successfully segmentation of brain

tumor tissues with high accuracy ($95.9 \pm 0.4\%$ for database of simulated MR images, and $93.2 \pm 0.3\%$ for database of real MR images).

In order to reduce the computational complexity and expedite the segmentation algorithm, and also to improve the system performance, some modifications are applied in the algorithm presented in previous algorithm. In the ***third algorithm***, we present a fully automatic tumor system which is combination of texture-based and contour-based algorithms. Skippy greedy snake algorithm is capable of segmenting the tumor area; however, the algorithm's accuracy and performance depends significantly on its initial points. Here, we modify the previous algorithm to automatically find proper initial points which not only obviates the requirement of manual interference, but also increase the accuracy and speed of optimization convergence. Comparing with previous method, this method achieves higher accuracy in tumor segmentation ($96.8 \pm 0.3\%$ for database of simulated MR images, and $93.8 \pm 0.1\%$ for database of real MR images) and lower computational complexity.

The intensity similarities between brain lesions and some normal tissues result in confusion within segmentation algorithms, specially in the database of real MR images. In order to improve the system performance for this database, a multi-spectral approach based on feature-level fusion is presented in ***forth algorithm***. Even though using multi-spectral MRI has several drawbacks and limitations, since it makes use of complementary information, it increases the accuracy of the system. Here, a feature-level fusion technique based on canonical correlation analysis (CCA) is proposed. It is worth mentioning that for the first time CCA is applied for combining MRI sequences in order to segment tumors. Even though data fusion increases computational com-

plexity of the segmentation algorithm, it results in a higher accuracy ($95.8 \pm 0.2\%$ for database of real MR images).

Dedicated to Francis,

Peanut, Badoum and April

Acknowledgements

I would like to thank my advisor Dr. Miroslav Kubat and my co-advisor Dr. Nigel John who supported me in the past few years through the research and completion of my degree. I believe their personality and technical capability was an indispensable factor for me to finish this endeavor.

NOOSHIN NABIZADEH

University of Miami

May 2015

Table of Contents

List of Figures

List of Tables

CHAPTER 1

Introduction

Computer vision and machine learning is concerned with the theory of artificial systems and the extraction of information from various images. The image data which is processed by the computer can take many forms, such as video sequences or images. As a technological discipline, computer vision seeks to apply its theories and models to the construction of computer vision systems to allow it to see as a person would see. In other words, to recognize objects, to know where it is and to interpret actions. While this may be an easy task for a human to perform, it is a highly complicated thing for a machine, computer or robot. Image segmentation is one of the most challenging topics in computer vision and machine learning. It is defined as manually or automatically partitioning the image into a set of relatively homogeneous regions with similar properties, each of which can be tagged with a single label [4]. As an application of image segmentation in biomedical research is to localize some specific cells and tissues, *e.g.*, tumor or stroke, in MR images [5]. Medical image segmentation helps physicians to find these lesions more accurately, and in emergency cases that specialist is not available, can be great source of information. Therefore, it is an important and crucial process in computerized medical imaging.

In this research, machine learning and computer vision techniques are used to develop some approaches to automatically segment brain tumors and stroke lesions in MR images. The importance of this study is obvious, since stroke and brain tumors are among first five leading causes of death in the United States. According to a statistical report published by the central brain tumor registry of the United States (CBTRUS), 285,294 primary brain and central nervous system tumors were newly diagnosed in period between 2004 to 2008 [6]. Eighty-five percent of brain and central nervous system tumors occurred in the persons of white race. The same report indicates that the incidence rate of primary brain tumors, whether benign or malignant, with 95 percent certainty is 19.82 cases per 100,000 persons per year [6]. Based on American heart and stroke association report, about 795,000 Americans suffer a new or recurrent stroke each year. That means a stroke occurs every 40 seconds on average. Stroke kills more than 137,000 people a year. It's the number four cause of death. On average, every 4 minutes someone dies of stroke. The 2006 stroke death rates per 100,000 population for specific groups were 41.7 for white males, 41.1 for white females, 67.7 for black males and 57.0 for black females [7].

Stroke/tumor management is a critical phase in which accurate detection and segmentation of brain tumor and stroke lesions in medical images have a great influence on clinical diagnosis, predicting prognosis, and treatment of these ailments. Additionally, it is beneficial for general modeling of pathological brains and the anatomical construction of brain atlases [8]. The detailed information about the location and volume of brain lesions is essential to number of researches in this field, such as identifying chronic functional deficits, or sleep problem analysis of stroke patients [9].

Typical medical imaging techniques are ultrasonography, computed tomography (CT), positron emission tomography (PET), and magnetic resonance images (MRI). Among them, MRI is the most widely used. One reason is being highly sensitive to local changes in tissue water since changes in tissue water reflect physiologic alterations that can be visualized by MRI. In addition, it is a non-invasive procedure, which unlike other medical imaging techniques enables the differentiation of soft tissues with high resolution. Another advantage of MRI is that it produces multiple images of the same tissue with different contrast visualization via the application of different image acquisition protocols and parameters [10]. These multiple MR images provide additional useful anatomical information for the same tissue. Complementary information from multiple contrast mechanisms helps researchers study the brain pathology more precisely.

Brain lesion detection and segmentation can happen either manually or automatically. In manual segmentation, the lesion areas are manually located on all contiguous slices in which the lesion is considered to exist. Manual segmentation is very expensive, time consuming, and generally suffers from the lack of permanent availability, reliability and reproducibility [11]. It is because of their reliance upon subjective judgments, which raises the possibility that different observers will reach different conclusions about the presence or absence of lesions, or even that the same observer will reach different conclusions on different occasions [12, 13]. Therefore, an effective automatic brain lesion segmentation algorithm is clinically beneficial and desirable.

Although there are several general segmentation methods such as thresholding [14], region growing [15], and clustering [16–19], they are not easily applicable on the brain lesion identification domain. The reason for this is the intensity similarities between brain lesions and some normal tissues, which can result in confusion within the algorithm. For example, if the lesion is inside the white matter (WM), there is overlapping intensity distributions between white matter lesion (WML) and grey matter (GM). Non-parametric or multi-parametric statistical classification techniques are not able to discriminate some areas of the WML from GM [10]. This is because of the limited resolution of the MR images and complex shapes of the brain tissues that impact a large number of the voxels located on the borders of various tissues. The border voxels are generally known as partial volume voxels and contain a mixture of tissues [10]. Therefore, there is an inherent uncertainty referred to as partial volume effect where individual voxels contain more than one tissue type . In addition, the image intensity in the center of a brain lesion is usually different from its periphery. Therefore, the image intensity at the borders of the brain lesions may be the same as GM. This phenomenon may cause confusion and misclassification of the peripheral regions of the lesions as GM. The same problem occurs at the edge of the brain, where the cerebrospinal fluid (CSF) and GM are averaged together and may present the voxel intensities which are typical to brain lesions [10].

In order to overcome this problem, many researchers use multi-spectral MR images for lesion identification [20–29]. However, applying multi-spectral MR images has four main difficulties. First, acquiring such data is not always feasible due to patient condition severity and time shortage [9,12]. Second, collection of multi-spectral MR images is expensive. Third, they can bring a lot of redundant information that increase the data processing time and segmentation errors [14]. And finally, multi-spectral MRI data suffers from inconsistency and misalignment, which requires image registration and bias correction prior to applying the segmentation algorithm [30]. Note that, any inaccuracy in registration or bias correction stages will directly affect the precision of the lesion segmentation. Owing to these limitations, detection and segmentation of the brain lesion based on single contrast mechanism MR images is desirable.

This study consists of three phases for brain lesion detection and segmentation. In ***chapter 4***, a new algorithm called histogram-based gravitational optimization algorithm, which is based on brain histogram analysis and an enhanced gravitational optimization algorithm is proposed. It presents a new way of histogram analysis to segment the brain. The algorithm is implemented for brain tumor and stroke detection and segmentation. The proposed algorithm begins with three main stages, which result in generation of several brain segments. These stages are: first, application of a weighted average technique on the brain histogram; second, convolution of a rectangular window with the histogram maximum bars; and third, connection of the cutoff borders after thresholding. After these steps, an enhanced optimization algorithm called n-dimensional gravitational optimization algorithm (NGOA) is applied to achieve the desired number of brain segments. The n-dimensional gravitational optimization algorithm is based on the principle of gravitational fields. It is motivated by the idea of gravitational forces between several masses and Newtonian laws of motion [31]. The objective function is a non-linear function of variables, which are called masses and defined based on brain image histogram analysis. The value of the objective function determines the movements and new locations of the masses. The masses are the length of the averaging window, the length of a rectangular convolution window, and the threshold of cutoff borders. The algorithm is iterated until a predefined iteration number or convergence is met.

It is important to consider that in previous studies, one method is applied for lesion detection and a different method is used for lesion segmentation, but here, a single algorithm is used for lesion detection and segmentation at the same time, which makes it more computationally efficient. The other contribution of the proposed algorithm is that it is independent of atlas registration, control groups, and prior anatomical knowledge. Furthermore, it uses single-spectral MRI for brain lesion analysis. Its importance comes from the fact that collection of multi-spectral MR images is time and cost consuming, and acquisition of just one spectral MR is much more practical. As another noteworthy contribution, the method is fully automatic, no need for any help of a clinician or initialization. In addition, the gravitational optimization algorithm is enhanced to extend it for n-dimension and decreased the possibility of optimization algorithm being drawn into a local optimal solution.

Four criteria as sensitivity, specificity, accuracy, and similarity index are applied to evaluate the algorithm performance. The experimental results on both synthetic and real MR images show that the proposed algorithm, provides an accuracy of almost 91.5% for stroke segmentation and 88% for tumor segmentation.

Histogram analysis limits the extracted information to the number of pixels in specific gray levels and does not include any region based information. Consequently, the accuracy of a histogram-based method is also limited. Since texture-based brain characterization has been proven to be an effective way of brain analysis, in ***chapter 5***, in order to increase the accuracy of brain tumor segmentation, a texture-based automated approach is presented. This algorithm consists of detection of tumor slices, tumor segmentation, and efficacy evaluation of feature sets. The proposed tumor slice detection technique is based on mutual information of histograms of two brain hemispheres. After detection of the slice that contains tumor, it is fed into the segmentation stage, which localizes the tumor area. The candidate tumor regions are obtained using a sliding window. This window sweeps through whole brain tissue excluding background area. A proposed post-processing method is applied to remove the false positives/negatives. The remarkable accuracy of the algorithm in tumor segmentation for database of simulated and real images is $95.9\pm0.4\%$ and $93.2\pm0.3\%$, respectively.

In this chapter, two most popular sets of well-established and competent texture-based feature extraction techniques are employed. The first set is Gabor wavelet feature extraction method that captures frequency, locality, and orientation, providing multi-resolution texture information about the spatial-domain as well as the frequency-domain [32, 33]. The second set, statistical features extraction methods, is based on applying statistical texture-based feature extraction methods, such as gray level co-occurrence matrix, histogram of oriented gradient, grey level run length matrix methods and etc. These feature extraction methods reflect the relationship between the intensity of two image pixels or groups of pixels. Furthermore, they estimate image properties related to the first- and second-order statistics [34–37]. Besides tumor detection and segmentation, a study on the effectiveness of these two feature extraction methods in this application is also offered. To reduce the possibility that the attained conclusion is only due to some idiosyncrasies of the employed machine-learning technique, the experiments are performed using several classifiers such as SVM, KNN, SRC, NSC, and k-means clustering. Two different MR single contrast mechanism as T1-weighted and FLAIR are separately used for evaluation in this study.

In ***chapter 6***, in order to reduce the computational complexity and expedite the segmentation algorithm, and also to improve the system performance, some modifications are applied in the algorithm presented in previous chapter. The algorithm modifications are applied in three main phases: feature extraction, feature selection, and tumor localization.

First, the feature extraction methods are expanded to include anisotropic Morlet complex wavelet transform (AM-CWT) and dual-tree complex wavelet transform (DT-CWT). It is worth mentioning that this is the first time that the AM-CWT and DT-CWT are applied for brain tumor segmentation purposes. These wavelets present aspects of data like trends, breakdown points, discontinuities in higher derivatives, and self-similarity, which other image analysis techniques overlook [38].

Second, in order to defy the curse of dimensionality to improve prediction performance, a novel feature selection technique based on regularized Winnow algorithm is proposed in which the regularized Winnow algorithm is modified to be applicable for non-binary inputs. While RWA classifier works with binary feature vectors, it is modified to not only work as a feature selection technique but also to be able to handle non-binary features. The presented feature selection method is fast and efficient in dealing with many irrelevant attributes.

Third, in order to localize the tumor area, the candidate tumor regions are attained using a sliding window, which sweeps through the whole brain tissue with 5 pixel steps, which decreases the computational complexity by 25 times. A tumor classification approach is then applied on every instance of the window. If the window is classified to have tumor, the central pixel of the window will be labeled as tumor. On the other hand, if it is classified as healthy, the central pixel will be labeled as healthy.

The regions determined by our method to be tumor will be used to construct the initial points for a skippy greedy snake algorithm. Specifying the appropriate initial points has a significant influence on the accuracy and the convergence speed of the skippy greedy snake algorithm. In addition, it obviates the requirement of human interference to manually specify initial points, which is one of the common limitations of the approaches using greedy Snake algorithm. Using this method, more accurate results for brain tumor segmentation ($96.8 \pm 0.3\%$ for database of simulated MR images, and $93.8 \pm 0.1\%$ for database of real MR images). It also results in lower computational complexity, since the average required time for tumor segmentation in each detected image using previous chapter method is around 2630ms, while applying the current method the average time is around 140ms.

The intensity similarities between brain lesions and some normal tissues result in confusion within segmentation algorithms, specially in the database of real MR images. In order to improve the system performance for this database, a multi-spectral approach based on feature-level fusion is presented in ***chapter 7***. Even though using multi-spectral MRI have several drawbacks and limitations, since it makes use of complementary information, it increases the accuracy of the system. Here, a feature-level fusion technique based on canonical correlation analysis (CCA) is proposed. CCA is one of the statistical methods dealing with the mutual relationships between two random vectors, and it has the same importance as principal component analysis (PCA) and linear discriminant analysis (LDA) in multivariate statistical analysis. It is one of the valuable multi-data processing methods. In recent years, CCA has been applied to several fields such as signal processing, computer vision, neural network and speech recognition. After registration of MR images to make them aligned, the slices containing tumor are recognized. After tumor slice detection, in order to populate the training data, random windows located all around the brain area are cropped. If the central pixel of the window falls in the tumor region, it is labeled as tumor and otherwise is labeled as healthy. Testing is applied on unseen slices using the sliding window approach presented in chapter 5. In this case of multiple sequences, the window selects a region of interest in corresponding sequences simultaneously. That is, for a single region of interest, there are two input images from two MR sequences. Feature vectors are extracted from corresponding regions of interest in both sequences simultaneously. In order to fuse the extracted features, CCA is applied. The fused feature vectors are fed into a support vector machines classifier and all the pixels in the brain area are labeled either healthy or tumor. A post-processing is applied on the labeled image to remove false positives and false negatives. The accuracy of the proposed algorithm is calculated by comparing the resulting label image with the golden label provided by the database.

It is worth mentioning that for the first time CCA is applied for combining information extracted from MRI sequences in order to segment tumors. Even though data fusion increases computational complexity of the segmentation algorithm, it results in higher accuracy (95.8 ± 0.2 for the database of real MR images).

CHAPTER 2

Magnetic Resonance Imaging

MRI is the imaging technique that has most benefited from technological innovation. The many advances have led to improvements in quality and acquisition speed. MRI is a medical imaging technique used in radiology to visualize detailed internal structures. MRI makes use of the property of nuclear magnetic resonance (NMR) to image nuclei of atoms inside the body [39].

An MRI machine uses a powerful magnetic field to align the magnetization of protons in the body, and radio frequency fields to systematically alter the alignment of this magnetization. This causes the protons to produce a rotating magnetic field of larger frequency detectable by the scanner and this information is recorded to construct an image of the scanned area of the body [40]. Strong magnetic field gradients cause nuclei at different locations to rotate at different speeds. 3D spatial information can be obtained by providing gradients in each direction.

MRI provides good contrast between the different soft tissues of the body, which make it especially useful in imaging the brain, muscles, the heart, and cancers compared with other medical imaging techniques such as computed tomography (CT) or X-rays. Unlike CT scans or traditional X-rays, MRI is noninvasive since uses no ionizing radiation.

An MRI sequence is an ordered combination of radio frequency (RF) and gradient pulses designed to acquire the data to form the image. The data to create an MR image is obtained in a series of steps. First the tissue magnetization is excited using an RF pulse in the presence of a slice select gradient. The other two essential elements of the sequence are phase encoding and frequency encoding, which are required to spatially localize the protons in the other two dimensions. Finally, after the data has been collected, the process is repeated for a series of phase encoding steps. The MRI sequence parameters are chosen to best suit the particular clinical application.

2.1 Gradient Echo

The gradient echo (GE) sequence is the simplest type of MRI sequence. It consists of a series of excitation pulses, each separated by a repetition time (TR). Data is acquired at some characteristic time after the application of the excitation pulses and this is defined as the echo time (TE). The contrast in the image will vary with changes to both TR and TE. Advantages of this sequence are fast imaging, low flip angle and less RF power. The disadvantages are difficulty to generate good T2 contrast, sensitivity to B0 inhomogeneities and sensitivity to susceptibility effects.

2.2 Spin Echo

The spin echo (SE) sequence is similar to the GE sequence with the exception that there is an additional 180 degree refocusing pulse present. The nuclear magnetic resonance signal observed following an initial excitation pulse decays with time due to both spin relaxation and any inhomogeneous effects which cause different spins in the sample to process at different rates. The first of these, relaxation, leads to an irreversible loss of magnetization. However, the inhomogeneous dephasing can be removed by applying a 180 degree inversion pulse that inverts the magnetization vectors [41]. Examples of inhomogeneous effects include a magnetic field gradient and a distribution of chemical shifts. If the inversion pulse is applied after a period t of dephasing, the inhomogeneous evolution will rephase to form an echo at time $2t$. In simple cases, the intensity of the echo relative to the initial signal is given by $e^{2t/T2}$ where $T2$ is the time constant for spin-spin relaxation.

2.3 Inversion Recovery

Inversion recovery (IR) sequence is usually a variant of a SE sequence in that it begins with a 180 degree inverting pulse. This inverts the longitudinal magnetization vector through 180 degree. When the inverting pulse is removed, the magnetization vector begins to relax back to B0. A 90 degree excitation pulse is then applied after a time from the 180 degree inverting pulse known as the TI (time to inversion). The contrast of the resultant image depends primarily on the length of the TI as well as the TR and TE. The contrast in the image primarily depends on the magnitude of the longitudinal magnetization (as in spin echo) following the chosen delay time TI.

Inversion recovery is used to produce heavily T1-weighted images to demonstrate anatomy. The 180 degree inverting pulse can produce a large contrast difference between fat and water because full saturation of the fat or water vectors can be achieved by utilizing the appropriate time to inversion.

2.4 Fluid Attenuated Inversion Recovery

Fluid-attenuated inversion recovery (FLAIR) is a pulse sequence and another variation of the inversion recovery sequence used in magnetic resonance imaging which was invented by Dr. Graeme Bydder. FLAIR can be used with both three-dimensional imaging as 3D FLAIR or two dimensional imaging as 2D FLAIR. FLAIR has the capability to allows a better detection of small hyperintense lesions.

In FLAIR, the signal from fluid *e.g.* CSF is nulled by selecting a TI corresponding to the time of recovery of cerebrospinal fluid (CSF) from 180 degree inversion to the transverse plane. The signal from CSF is nullified and FLAIR is used to suppress the high CSF signal in T2 and proton density weighted images so that pathology adjacent to the CSF is seen more clearly. A TI of approximately 2000 ms achieves CSF suppression at 3.0 T. In FLAIR, bright signal of the CSF (cerebrospinal fluid) is suppressed which allows a better detection of small hyperintense lesions.

2.5 T1-Weighted

To demonstrate T1-weighted images (T1-w), specific values of TR and TE are selected for a given pulse sequence. The selection of appropriate TR and TE weights an image so that one contrast mechanism predominates over the other two. A T1-weighted image is one where the contrast depends predominantly on the differences in the T1 times between tissues *e.g.* fat and water. Because the TR controls how far each vector can recover before it is excited by the next RF pulse, to achieve T1-weighting the TR must be short enough so that neither fat nor water has sufficient time to fully return to B0. If the TR is too long, both fat and water return to B0 and recover their longitudinal magnetization fully. When this occurs, T1 relaxation is complete in both tissues and the differences in their T1 times are not demonstrated on the image. In T1-w images, tissue with short T1 relaxation time appears brighter (hyperintense).

2.6 T2-Weighted

A T2-weighted image is one where the contrast predominantly depends on the differences in the T2 times between tissues *e.g.* fat and water. The TE controls the amount of T2 decay that is allowed to occur before the signal is received. To achieve T2 weighting, the TE must be long enough to give both fat and water time to decay. If the TE is too short, neither fat nor water has had time to decay and therefore the differences in their T2 times are not demonstrated in the image. In T2-w images, tissue with long T2 relaxation time appears brighter (hyperintense).

2.7 Proton Density

A proton density (PD) image is one where the difference in the numbers of protons per unit volume in the patient is the main determining factor in forming image contrast. Proton density weighting is always present to some extent. In order to achieve proton density weighting, the effects of T1 and T2 contrast must be diminished, so that proton density weighting can dominate. A long TR allows tissues e.g. fat and water to fully recover their longitudinal magnetization and therefore diminishes T1 weighting. A short TE does not give fat or water time to decay and therefore diminishes T2 weighting. Fig. 2.1 shows a comparison of T1, T2, FLAIR and PD. In Table 2.1, TR and TE for T1, T2, and PD weighted sequences are compared.

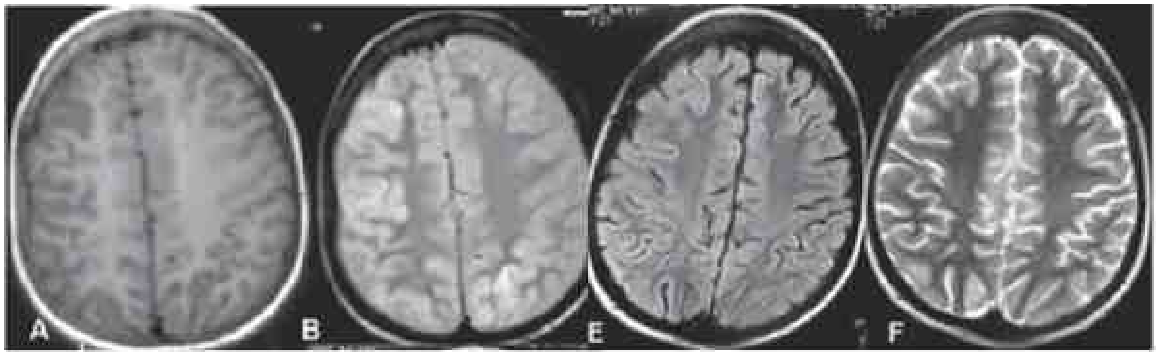

Figure 2.1: Samples of four MRI images: (A)T1-weighted, (B)PD, (E)FLAIR, and (F)T2 weighted axial brain images

Table 2.1: Comparing TR and TE for T1, T2, and PD weighted sequences

Sequences	T1	T2	PD
TR	Short ($< 750ms$)	Long ($> 1500ms$)	Long ($> 1500ms$)
TE	Short ($< 40ms$)	Long ($> 75ms$)	Short ($< 40ms$)

CHAPTER 3

Related Work

Developing an automatic system for processing MRI data and automatic brain lesion segmentation is necessary to reduce both human errors and workload. But it is still a challenging task. Many studies and methods are reported and proposed for solving this problem during recent decades.

Considering the existing literature, a generic typical computer aided diagnosis (CAD) system for brain lesion segmentation consists of following steps: image acquisition, pre-processing, feature extraction, normalization, classification, post-processing and evaluation. The general structure of the CAD system is presented in Fig 3.1. The brain lesion segmentation techniques can be categorized into four categories as: (1) data-driven, (2) statistical, (3) intelligent, and (4) deformable models [10]. Here each category is briefly described.

Data-Driven Methods: If a method is about thresholding, region growing, and other spatial approaches, it is categorized into the data-driven group. [42], [43], and [44] are few examples of studies applied data-driven methods.

Another category of the data-driven methods are hierarchical techniques. Pachai et al. [45] proposed an automatic segmentation algorithm based on a multi-resolution

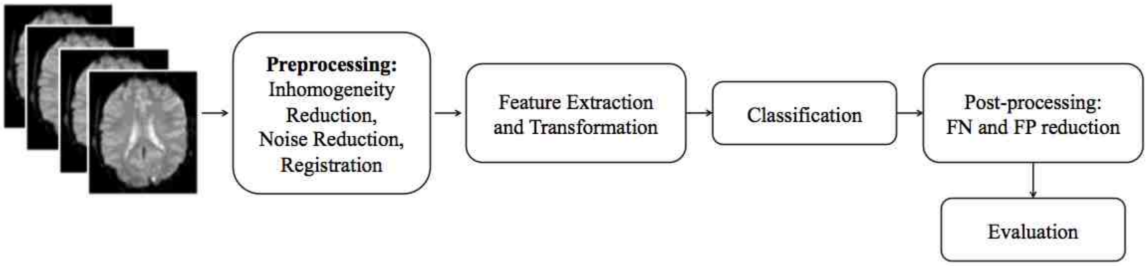

Figure 3.1: Flowchart of a typical CAD system for brain lesion

approach using pyramidal data structure. First, a pyramidal Gaussian decomposition is constructed. This pyramid is a data structure which contains different resolutions of the image at different levels. The base of the pyramid is the original image, and other levels are filled with down-sampled and low-pass-filtered versions of the original image using the kernels. This reduces the size of the original image by a factor of 2 in each level. From this pyramid, an expanded Gaussian pyramid is built by bringing back the reduced size images in each level to their original size. A Laplacian pyramid is generated by successive subtraction of the image in each level of the expanded pyramid from the original image. The enhanced features of the pyramid are much easier to detect than the intensities in the original image. The Laplacian pyramid is automatically and locally thresholded.

Statistical Methods: In case the method concerns estimation of probability density functions, it is classified into the statistical group. Statistical methods can be grouped into two main categories: non-parametric probability map model-based techniques and parametric model-based techniques. These two kinds of techniques are combined to generate combinational techniques. Anbeek et al. [46, 47] used kNN classification to determine the lesion probability per voxel. The learning set consist of

5 voxel intensities of T1-w, T2-w, PD-w, IR, and FLAIR MR Images, in addition to the (x, y, z) coordinates of each voxel. Then a lesion probability map is constructed based on the number of lesion voxels among the k neighbors. Finally, the map is thresholded to generate a binary segmentation of the lesions.

Another category of statistical methods are parametric model-based techniques. Kamber et al. [48, 49] used mixture Gaussian model for lesions and tumors detection. Lesions are assumed as outliers of the global intensity distribution assuming that lesion voxels are distinctly different from normal tissue characteristics. Leemput et al. [17, 24] developed automatic segmentation of MR images of normal brains by statistical classification, using a stochastic model for normal brain which detects multiple sclerosis (MS) lesions as outliers. Brain tumors however, cannot be simply modeled as intensity outliers due to overlapping intensities with normal tissue and/or significant size.

Warfield et al. [50, 51] combined elastic atlas registration with statistical classification. Elastic registration of a brain atlas helped to mask the brain from surrounding structures. “distance from brain boundary” is used as an additional feature for separation of clusters. Initialization of probability density functions still requires a supervised selection of training regions. Freifeld et al. [52] used a probabilistic model named constrained Gaussian mixture model (CGMM) based on a mixture of multiple Gaussian distribution for each brain tissue from T1-weighted, T2-weighted and proton density weighted (PD) modalities. The parameters of this model were estimated using the EM method. MS lesions were recognized as outlier Gaussian components and were grouped to form a new class besides other tissues. Wells [53] introduced expectation maximization (EM) as an iterative method that interleaves classification with bias filed correction. Menze et al. [54] applied a generative model based on an improved multivariate expectation maximization algorithm for tumor segmentation on multi-model image volumes.

Some researchers use a combination of parametric and non-parametric model-based techniques to benefit from both techniques. Sajja et al. [22] use a combined algorithm of parametric and non-parametric techniques to reduce the number of false MS classification. A similar approach is employed by Datta et al. [23].

SVM and Markov random field (MRF) are also categorize into statistical method. Ruan et al. [55] identified tumor regions by training a support vector machine on mean and variance extracted from small patches of multi-parametric MRI images. Lao et al. [56] used SVM for white matter lesions segmentation. Chen et al. [57] and Lee et al. [58] used MRF and SVM based conditional random fields for tumor segmentation, respectively. In an adaptive training framework proposed by Zhang et al. [59], multi-kernel support vector machine was trained to do tumor classification.

Intelligent Methods: If the method involves fuzzy logic and/or neural networks, it is categorized into the intelligent group. Zijdenbos et al. [28, 49] applied ANN for quantification of white matter lesion and multiple sclerosis lesion. Admasu et al. [60] suggested an improvement to the Udupas approach by using an ANN, instead of user, to make decision about the void pixels. [61], [62], and [63] applied ANN for brain segmentation of multi-modal medical images.

Others introduced knowledge-based (KB) techniques to make more intelligent classification and segmentation decisions. One of the knowledge-based systems is based on fuzzy techniques. Fuzzy connectedness is a method proposed by Udupa et al. [29]. based on this principle that the object information in images is fuzzy and has a special connectedness which is also fuzzy. Shen et al. [9] used a fuzzy c-mean (FCM) for stroke lesion detection based on single-spectral MRI. Fuzzy membership functions are calculated for four categories. The tissue probability map is also calculated using SPM5. Inconsistencies greater than a threshold between pixel intensities and probabilities detects the brain lesion. In [64] and [65], fuzzy rules were applied to make initial classification decisions, then clustering (initialized by the fuzzy rules) was used to classify the remaining pixels.

More explicit knowledge has been used in the form of frames [66] or tissue models [67], [48]. Clark et al. [20] showed that a combination of KB techniques and multispectral analysis (in the form of unsupervised fuzzy clustering) could effectively detect pathology and label normal brain tissues.

Deformable Methods: In case the method concerns volume estimation and also shrinking or increasing of the estimated volume, it is classified into the deformable group [10]. Metaxas et al. [68] proposed a hybrid deformable method, composed of several deformable models such as shape model, texture integration model and graphical model is proposed in . Cai et al. [69] discriminated all the existing tissues such as edema, white matter, grey matter, and cerebrospinal fluid using probability map, which can also predict tumor growth at the same time.

Cuadra et al. [70] used a priori models of lesion growth in order to segment large brain tumors in T1-weighted images. It categorized into deformable models. The disadvantage of this method is that it is semi-automatic and requires a seed voxel within the tumor to be chosen manually. In addition, anatomical and biological knowledge of tumor growth is needed to select the seed appropriately. Yang et al. [71]

presented a combination of deformable contours and FCM techniques, but still the performance is lower than that of the statistical methods.

Comparison of Four Methods: With comparison between different brain lesion segmentation techniques, it can be seen that the data-driven methods generate the lowest accuracies. In this category, the thresholding methods do not consider the overlaps among the intensity ranges of different tissues and do not therefore benefit from the spatial information. Also, the selection of appropriate thresholds can be complicated. The region growing and the edge detection methods work based on the gradient of the intensities and thus are very sensitive to noise. Successful region growing, however, requires precise anatomical information to locate single or multiple seed pixels for each region [10].

Statistical methods such as the expectation maximization (EM) algorithm and non-parametric methods such as Parzen window and kNN are commonly used for image classification. In brain MRI segmentation applications, a disadvantage of the EM algorithm is the assumption of normal distributions for the intensity variations of the brain tissues, which is almost inaccurate especially for brain lesions. kNN suffers from the excessive calculation time which severely affects the training stage.

Intelligent methods are also used for the segmentation of brain images and brain lesions. ANN, FCM, fuzzy connectedness, fuzzy inference systems (FIS) are commonly used methods in this category. ANN presents a good accuracy but it needs a good estimate of the number of layers and the number of nodes in each layer. Also, excessive training time is another issue in this type of classifiers. FCM was shown to be superior on normal brain images, but worse on abnormal brain images. A shortcoming of FCM is its over-sensitivity to noise, which is also a flaw of many other intensity-based segmentation methods [10].

Deformable techniques usually benefit from matching the MR images with an atlas, to locate the lesions. The philosophy of these methods is choosing a seed voxel of lesions manually. Thus, this selection should be based on an anatomical and biological knowledge of lesion growth.

The most popular methods are EM, and then kNN together with FCM [10]. However, FCM cannot individually attain good results and needs to be complemented by another segmentation method. However, the combination often increases the computation time of the method. In addition, kNN has the problem of high memory capacity for storing the model parameters. ANN is another popular method which sometimes suffers from a long training procedure. The major problem with kNN in the brain lesion CAD systems is its long time training. This problem can be solved through an automated selection of training samples from non-rigidly registered MR data with a tissue probability atlas.

Using Atlas Registration: Some approaches use geometric prior information for MR brain image/brain lesion segmentation based on atlas-based registration. A fully labeled template MR volume is registered to an unknown dataset. High dimensional warping results is a one-to-one correspondence between the template and subject images, resulting in a new, automatic segmentation. These methods require elastic registration of images to account for geometrical distortions produced by pathological processes. Such registration remains challenging and yet not solved for the general use.

Methods Using Single-Spectral MR Images: Majority of studies use multi-spectral MR images. However, applying multi-spectral MR images has four main difficulties [12]. First, acquiring such data is not always feasible due to patient condition severity and time shortage. Second, collection of multi-spectral MR images is expensive. Third, they can bring a lot of redundant information that increase the data processing time and segmentation errors [30]. And finally, multimodal MRI data suffers from inconsistency and misalignment, which requires image registration and bias correction prior to applying the segmentation algorithm [14]. Note that, any inaccuracy in registration or bias correction stages will directly affect the precision of the lesion segmentation. A few studies have addressed the brain lesion segmentation using single-spectral MR images [70, 72–78].

Prakash et al. [72] used ratio of intensity probability density functions (pdf) as a divergence measure for stroke lesion segmentation on diffusion-weighted magnetic resonance imaging.

Prastawa et al. [78] proposed a tumor segmentation method based on outlier detection using the T2 MR image channel. The segmentation framework is composed of three stages. First, abnormal regions are detected using a registered brain atlas as a model for healthy brains. Then the robust estimates of the location and dispersion of the normal brain tissue intensity clusters are made to determine the intensity properties of the different tissue types. In the second stage, it is determined whether edema appears together with tumor in the abnormal regions using the T2 image intensities . Finally, geometric and spatial constraints are applied to detected tumor and edema regions.

Cuadra et al. [70] used a priori models of lesion growth to segment large brain tumors. However, it is a semiautomatic approach where a seed voxel of tumors has to be chosen manually. The selection thus requires anatomical and biological knowledge of tumor growth.

Kennedy et al. [79] presented a computational system called WebParc that measures the stroke lesion volume and provides the location information with respect to canonical forebrain neural systems using DWI images. WebParc is implemented in the template registration style of localization analysis, and it is a data management system that segments the lesion manually with the clinician help. Afterward, it extracts the lesion information with respect to a set of co-registered anatomical templates of detailed brain structures. The setback of this system is that the lesion is segmented manually. Moreover, it depends on registration and anatomical templates.

Mah et al. [80] introduced a simple unsupervised lesion segmentation algorithm based on Zeta using DWI images. Zeta is a recently proposed general measure of statistical abnormality, i.e., an abnormality score. The algorithm identifies the parameters of lesions within a brain image using a reference set of normal brain images. To determine the abnormality of a single image, it is compared to the k instances within the reference set that resembles it most closely. The drawback of this method is that the first step in Zeta segmentation relies on the image registration, which is the drawback of most voxel-wise algorithms. Moreover, Zeta requires a set of normal images to use as a standard reference. In addition, the Zeta abnormality score is a continuous variable with no a priori criterion on which one could discretize it.

Mujumdar et al. [81] applied combined information from DWI-(b=2000), DWI-(b=1000) and the apparent diffusion coefficient (ADC) map to segment stroke lesions.

Regarding the fact that DWI with higher b-values (b=2000) provides improved sensitivity, higher conspicuity and reduced artifacts, it improves the detectability of smallest infarcts than conventional DWI-(b=1000). However, in most cases, DWI with higher b-values (b=2000) is not available and it causes an impactful restriction.

Hevia Monteil et al. [82] segmented the stroke lesions applying nonparametric density estimation based on mean shift algorithm and edge confidence map using DWI images. Briefly, the edge confidence map is computed from the data to be segmented. Afterward, filtering happens by applying a weighted mean shift procedure; and subsequently, region adjacency analysis, transitive closure operations, and pruning are used to segment stroke lesion. The drawback of this method is its inability to accurately handle low resolution and noisy data, particularly for the small-sized lesions.

Stamatakis et al. [73] presented a statistical method to identify brain abnormalities using T1-weighted images. Every image is compared to a normal control group and the detected structure differences between the image and the control group is identified as an abnormality. Srivastava et al. [74] used a similar statistical approach to detect focal cortical dysplastic lesions from a lesion-specific feature map using T1-weighted images. However, the disadvantage of the above-mentioned methods is that the choice of a control group (e.g., group size) can affect segmentation results [83]. In addition, the test data and the control group should be prepared using the same scanner machine, same parameters and coils, otherwise it causes further bias.

Li et al. [84] presented a multi-stage process for stroke lesion segmentation on DWI images. The process consists of image preprocessing, global and local registration between the anatomical brain atlas and the patient, and finally segmenting stroke lesion based on region splitting and merging and multi-scale adaptive statistical classification. The drawback of this method is that it relies on the registration, and also is computationally expensive.

In a overall view, most of the lesion segmentation techniques discussed and reported in the literature have a few main limitations. These limitations can be concisely listed as: reliance on multi-spectral MRI [85, 86], dependencies on preprocessing for bias-correction, or local or global registration of brain images to an anatomical atlas [85–87], requiring conformances to the initial assumption such as number of tissue classes [84, 88], dependency on high resolution and low noise data [82], and not being fully automatic [79, 84]. Finding a method to address these limitations and gaining high accuracy is our desirable goal in this study.

CHAPTER 4

Stroke Lesion Detection Using Histogram-Based Gravitational Optimization Algorithm

4.1 System Approach

“It was an usual day, a few weeks after my fifteenth birthday. That day, I remember that I had soreness down the left side of my body, along with what I thought was a bad headache. I didnt feel quite right, but I thought that this was nothing to get concerned about. Neither did my parents. The headache, along with other symptoms, which I now realize were warning signs of stroke, were things I had experienced before. Then the pains had disappeared after a few hours. I put these down to crankiness, eye-strain, or teenage growing pains. That night, I went off to bed, thinking that I would feel fine in the morning. The next thing I remember was waking up in the intensive care ward at the local hospital. I was eventually moved out of intensive care into a ward. I was paralysed down the left side of my body, and had a bandage around my head. Then came the day when the doctors explained what had happened to me. I was told that I had suffered a massive stroke.” A stroke survivor shares his experience of the tragic incidence [89, 90].

Stroke is one of the most important causes of mortality and morbidity in human being. Stroke is defined as a sudden development of a neurological deficit [12]. It can be further divided into two major categories of ischemia with approximately 85% to 90% and haemorrhage with 10% to 15% of diversities. Cerebral ischemia happens as a result of the bursting or blocking of an artery stops or interrupts the brain blood supply. This damaged artery leads to an insufficient blood flow in either a global or a focal fashion, resulting in an infarct in the brain, which encompasses dead tissues [9]. An accurate detection and diagnosis of ischemic lesion is extremely essential for clinical prognosis, treatment, and also stroke related research [9]. Regarding to time importance in stroke diagnosis and limitations of access to specialist, an effectual automatic stroke lesion detection algorithm is clinically useful and desirable.

Here a new algorithm for stroke detection and segmentation is proposed. The algorithm is called *histogram-based gravitational optimization algorithm (HGOA)* [91]. The algorithm is based on brain histogram analysis and an enhanced gravitational optimization algorithm. The algorithm is implemented for brain tumor and stroke detection and segmentation. The advantage of the proposed algorithm is that it is independent of multi-spectral MRI data, atlas registration, control groups, and prior anatomical knowledge. Since collection of multi-spectral MR images is time and cost consuming, acquisition of just single MR sequence is more practical. The other contribution is its computational efficiency. It is important to consider that in previous studies, one specific method is applied for lesion detection and another different method is used for segmentation, but in this work, a single algorithm is used for lesion detection and segmentation at the same time. As another noteworthy contribution, our method is fully automatic, no need for any help of a clinician or ini-

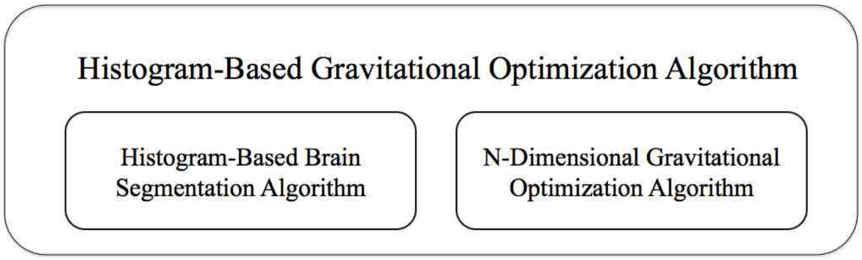

Figure 4.1: Histogram-based gravitational optimization algorithm

tialization. Moreover, the gravitational optimization algorithm is enhanced to extend for n-dimension. Also with formulae modifications, the possibility of optimization algorithm being drawn into a local optimal solution is decreased.

This algorithm can be divided into two parts as “histogram-based brain segmentation algorithm” and “n-dimensional gravitational optimization algorithm” (see Fig. 4.1). The HGOA is summarized as follows:

- Select the desired number of brain segments
- Select the number of initial generation and the iteration.
- Run n-dimensional gravitational optimization algorithm. The fitness value is defined as the squared difference between the desired number of segments and the achieved number of segments. There are three variables that influence the fitness value. These are the length of averaging window in step two, the length of convolution window in step four, and the threshold value in step five, which will be explained in the following section. The objective function of the optimization algorithm with respect to each single set of variables is calculated using result

of histogram-based brain segmentation algorithm, which includes seven steps as following:

- Step1: Calculate the image intensity histogram
- Step2: Apply a weighted averaging technique on the image histogram
- Step3: Extract the local maximum from the averaged image histogram
- Step4: Convolve a rectangular window with the intensity histogram peaks obtained from step 3
- Step5: Obtain the lower and the upper cutoff borders for all segments using a threshold value
- Step 6: Connect the upper cutoff border of n^{th} segment to the lower cutoff border of $(n+1)^{th}$ segment proportionally to the distribution value of the calculated intensity histogram from step 4 (In this step the number of achieved segments are equal to the total number of low or up cutoff borders.)
- Step 7: Allocate a specific intensity value to each generated segment.

To evaluate the performance of the lesion segmentation algorithm, a standard is required to assess it with. Here the standard is the manual tracing of each lesion by a trained operator: this is considered the gold standard in the field [21]. What is needed to determine is therefore the correspondence between two binary volume images. In line with established practices, [28, 47], the following summary measures are used:

$$Sensitivity = \frac{TruePositives}{TruePositives + FalseNegatives} \times 100\% \tag{4.1}$$

$$Specificity = \frac{TrueNegatives}{TrueNegatives + FalsePositives} \times 100\% \tag{4.2}$$

$$Accuracy = \frac{TruePositives + TrueNegatives}{TP + TN + FP + FN} \times 100\% \tag{4.3}$$

$$SimilarityIndex = \frac{2(TruePositives)}{2(TP) + FalsePositives + FalseNegatives} \times 100\% \tag{4.4}$$

where True Positives (TP) are voxels correctly identified as part of a lesion, True Negatives (TN) are voxels correctly identified as healthy, False Positives (FP) are voxels incorrectly identified as part of a lesion, and False Negatives (FN) are voxels incorrectly identified as healthy.

4.2 Histogram-Based Gravitational Optimization Algorithm

As mentioned earlier, HGOA is separated into two parts as *histogram-based brain segmentation algorithm* and *n-dimensional gravitational optimization algorithm*. The histogram-based brain segmentation algorithm starts by building the image intensity histogram. It is assumed that the local maximums of the histogram are potentially representatives of various segments in the brain. Therefore, the number and the intensity value of the histogram local maximums can be related to the number and the center value of segments, respectively. Even though in MRI each pixel is actually a

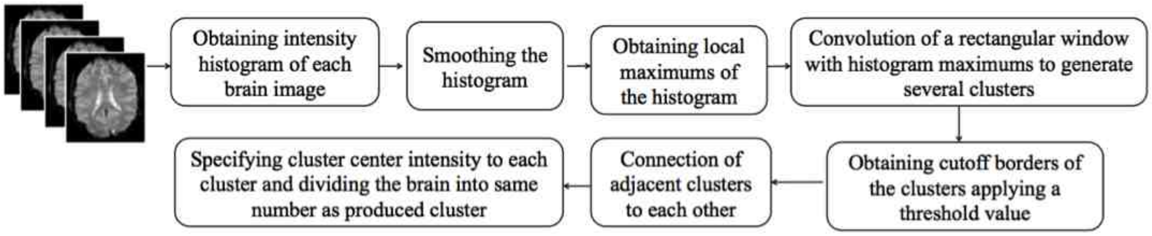

Figure 4.2: Flowchart of the seven steps histogram-based brain segmentation algorithm

voxel, each pixel is treated as belonging to one segment. The reasons for this assumption are computational simplicity as well as its practical medical use. Therefore, the distance from one local maximum to another one is equally or proportionally divided between the two local maximums to cover the whole intensity range. If it is divided proportionally, then the local maximum value affects the width of each segment. Doing so, the brain can be segmented to the same number of segments as its histogram local maximums. However, if the desired number of brain segments is different from the total number of brain histogram local maximums, a modified optimization algorithm called n-dimensional gravitational optimization algorithm helps to dynamically segment the brain into the desired number of segments. For this purpose, it is necessary to define an optimization process in which the objective function is created from the brain histogram analysis. An optimization process is defined to minimize the difference between the achieved number of segments and the desired number of segments. The optimization process works based upon an iterative calculation of an objective function, which is created from histogram-based brain segmentation algorithm.

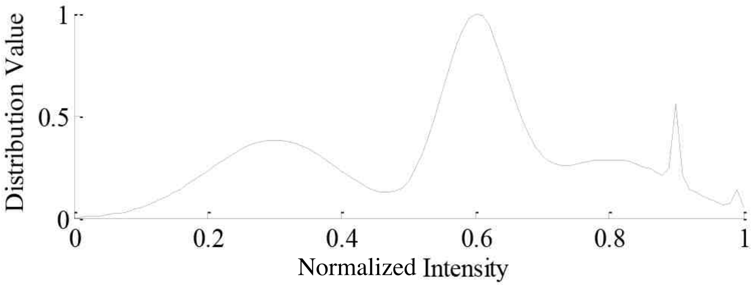

Figure 4.3: The histogram of the preprocessed DWI image

4.2.1 Histogram-based Brain Segmentation Algorithm

The histogram-based brain segmentation algorithm can be described in seven steps as shown in Figure 4.2 and detailed as follows:

Step1: the image intensity histogram is calculated. Let f be a given image represented as a matrix of integer pixel intensities ranging from 0 to $L-1$. L is the number of possible intensity values, often 256. Let $H[n]$ denote the normalized histogram of f with a bin for each possible intensity [92]. So

$$H[n] = \frac{number of pixels with intensity n}{total number of pixels} \qquad n = 0, 1, , L-1 \tag{4.5}$$

Noise reduction is an important step to increase image quality and to improve the performance of quantitative imaging analysis tasks. A low pass Gaussian filter is applied for noise removal. Figure 4.3 shows one example of histogram of a normalized and denoised DWI image.

Step2: In order to smooth the histogram $H[n]$, local weighted averaging technique is applied over the histogram using the following equation:

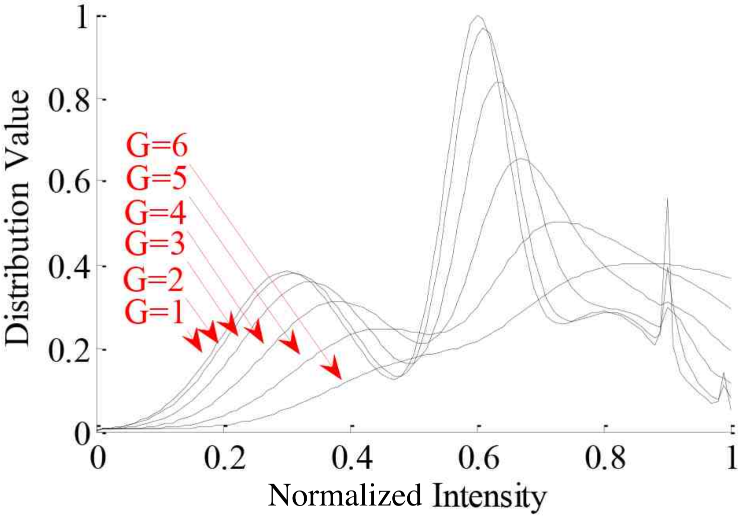

Figure 4.4: The averaging of the image histogram shown in figure 4.3

$$\bar{H}[n_i] = \sum_{i}^{i+G} w_i.H[n_i]/G$$
$$w_i = \sum_{i}^{i+G} \|n_i - M_w\|^2 \tag{4.6}$$

where $H[n_i]$ is the histogram distribution value of i^{th} bin, w_i is the weight corresponding to the i^{th} bin, and G is the length of averaging window. M_w is the average of the intensities in the window, n_i is the pixel intensity for the i^{th} element, and $\bar{H}[n_i]$ is local average value of the histogram. It is obvious the greater the G, the smother the averaged histogram will be. Figure 4.4 shows the average image histogram of Figure 4.3 for different values of G. This part helps to control the number of local maximums and local minimums of the intensity histogram.

Step3: the local maximums of smoothed histogram are simply calculated by:

$$H_{max-Local}[n] = \bar{H}[n_i] | (\bar{H}[n_i] > \bar{H}[n_{(i+1)}]) \bigcap (\bar{H}[n_i] > \bar{H}[n_{(i-1)}]) \tag{4.7}$$

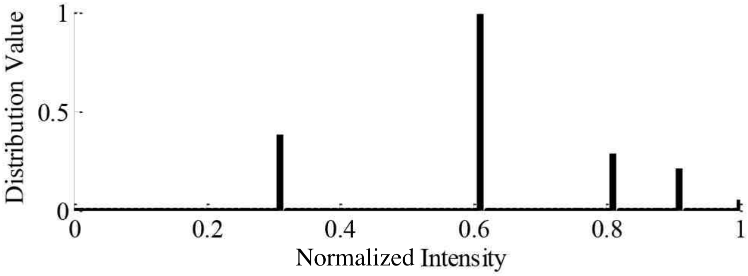

Figure 4.5: Extraction of local maximums from figure 4.4 and $G = 1$

By applying equation 4.7 on Figure 4.4 with $G = 1$, the local maximums are derived as represented in Figure 4.5.

Step4: a rectangular window is convolved with the histogram local maxima calculated from step 3. It is assumed that the number and intensity location of the local maxima of the histogram can be an indication of different segments in the brain image. Therefore, the key idea for brain image segmentation is to automatically grow a local maximum of the smoothed histogram toward its neighbor local maximum with respect to its amplitude, location, and anticipated number of brain segments. To do this, the convolution of $H_{max-Local}[n]$ and a rectangular window is employed to connect the local maximums that are in each others neighborhood. Let W be the length of a rectangular window called Win, and M be the length of $H_{max-Local}[n]$, then $Y[n]$ is the vector of length $M + W - 1$ whose n^{th} element is calculated by:

$$Y[n] = Win[n] * H_{max-Local}[n] = \sum_{j} Win[j] H_{max-Local}[n-j] \tag{4.8}$$

The function $Y[n]$ potentially has several discriminative segments. A narrower convolved window obviously produces higher number of segments, and vice versa, a wider convolved window results in lower number of segments. The application of

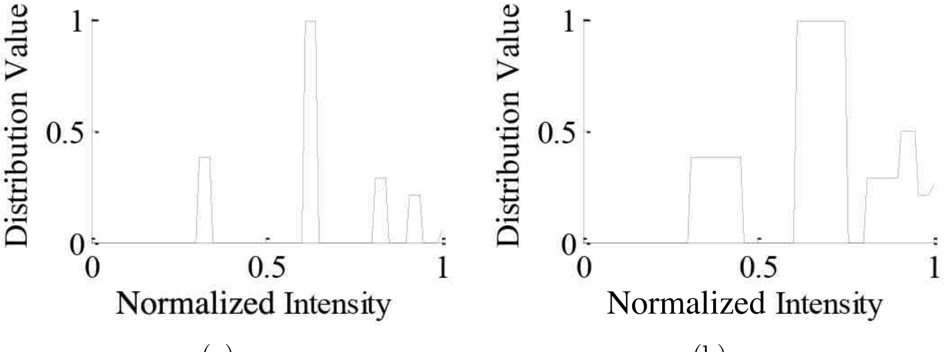

(a) (b)

Figure 4.6: Connection of local maximum from Fig. 4.5 with using two different convolving window sizes, (a) narrow window $n = 4$, (b) wide window $n = 14$

equation 4.8 on Fig. 4.5 for a narrow and a wide window is depicted in Fig. 4.6. A narrower window obviously yields higher numbers of segments.

Step5: the lower and upper cutoff boundaries for all segments are obtained using a threshold value. In order to create continuous and discriminative segments, convolution of $H_{max-Local}[n]$ and a rectangular window, Win, was calculated, which result in $Y[n]$. A threshold value as Thr controls the cutoff boundaries and removes the values smaller than the specified threshold value in the distribution. Also it helps to increase the flexibility of optimization method because changing the threshold level would change the number of remained segments. The cutoff boundaries of $Y[n]$ are calculated as:

$$X_{low}[n_i] = \{n | Y[n_{(i+1)}] > Thr \bigcap Y[n_{(i-1)}] < Thr\} \tag{4.9}$$

$$X_{high}[n_i] = \{n | Y[n_{(i-1)}] > Thr \bigcap Y[n_{(i+1)}] < Thr\} \tag{4.10}$$

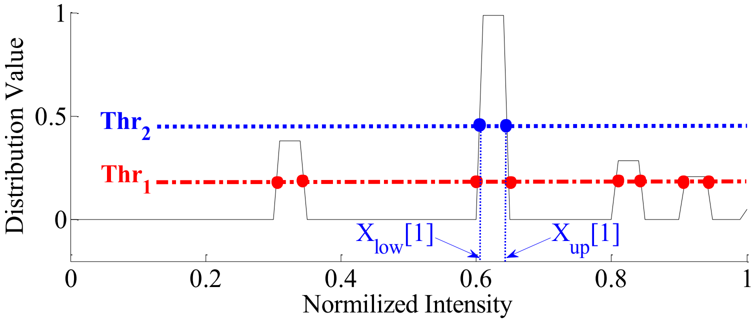

Figure 4.7: Extraction of local maximums from figure 4.4 and $G = 1$

The number of the segments which are visible in histogram data is the same as the total number of lower or upper cutoff boundaries of the function $Y[n]$. The value of the selected threshold has a great influence on the final number of created segments. The application of equations 4.9 and 4.10 on the results illustrated in Fig. 4.6 is depicted in Fig. 4.7. Significant impact of specified threshold value on the number of generated segments is clearly seen. For example Thr_2 only results in one segment, however, Thr_1 leads to four segments.

Step 6: the upper cutoff border of n^{th} segment is connected to the lower cutoff border of $(n+1)^{th}$ segment based on equation 4.11. The reason is to cover all intensity bins and fill up the gaps between $X_{high}[n_s]$ and $X_{low}[n_{(s+1)}]$. Moreover, every pixel needs to be assigned to a single segment. In this step, upper cutoff border of one segment reaches to the lower cutoff border of the next one based on the following rule.

$$X_{up-new}[s_n] = X_{low-new}[s_{n+1}] = X_{up}(s_n)+(X_{low}(s_{n+1})-X_{up}(s_n))\times\frac{LM(s_n)}{LM(s_n)+LM(s_{n+1})} \tag{4.11}$$

where the s_n is the index of the n^{th} segment, $LM(s_n)$ is the local maximum amplitude of the segment s_n , and $LM(s_{n+1})$ is the local maximum amplitude of the segment s_{n+1}.

Step 7: one specific intensity value is specified for each generated segment. All intensity values between lower and upper cutoff borders of one segment would be represented by one intensity value named $X_{center}(s_n)$. The intensity of the s_n^{th} segment is defined as:

$$X_{center}(s_n) = \frac{X_{low-new}(s_n) + X_{up-new}(s_n)}{2} \tag{4.12}$$

The brain is segmented according to the number of generated segments, the intensity of center of the generated segment, and the cutoff borders of the generated segments. In order to automate this process, an optimization process is applied to minimize the difference between the achieved number of brain segments and the desired number of brain segments. The objective function is described as squared difference between the desired number of brain segments and the achieved number of brain segments. That is, if the brain needs to be segmented into four segments, the desired number of brain segments would be four. Here, there are three variables that influence the objective function. These are the length of averaging window described in step two (G), the length of convolution window described in step four (W), and the threshold value described in step five (Thr). In next section, the n-dimensional gravitational optimization algorithm is explained.

4.2.2 N-Dimensional Gravitational Optimization Algorithm

The second part of our proposed algorithm is an enhanced optimization algorithm called *n-dimensional gravitational optimization algorithm (NGOA)*. In order to achieve the desired number of the brain segments, NGOA is applied on the results of histogram-based brain segmentation algorithm, which produce the objective function value. The goal of optimization algorithm is minimization of the objective function.

NGOA utilizes the principles of gravitational field. Similar to the space gravitational algorithm [31], this algorithm is motivated by a simulation of several space masses to search for the heaviest mass. In this paper, the search is expanded over the n-dimensional search space while in [31] masses are modeled in 2-D. Some formulae modifications are considered in this work. According to the Newtons law of gravity, the strength of gravity existing between particles depends on the mass of particles and the gravitational acceleration rate and the inverse squared distance of the particle masses. Moreover, Einstein's general theory of relativity confirms that the particle will be able to accelerate toward the heavy mass around it by the changes in the geometry of space-time. It means that if K particles with different masses are left in a free space, the particles have a tendency to move toward each other. While the heavy particles have slight movements, the movement of lighter particles is more than that of the heavier ones. Therefore, the lighter particles move towards heavy ones and then keep exploring for other heavy particles around. This is very desirable in development of optimization algorithms.

The NGOA is initialized by random selection of K sets of n-dimensional masses and the iteration number. In other words, for the n-dimensional search space, the position, velocity, and acceleration of i^{th} mass can be represented by n-dimensional vectors as follows:

$$\begin{aligned} X_i &= [x_{i1}, x_{i2}, \ldots, x_{in}]^T \\ V_i &= [v_{i1}, v_{i2}, \ldots, v_{in}]^T \\ a_i &= [a_{i1}, a_{i2}, \ldots, a_{in}]^T \end{aligned} \tag{4.13}$$

Therefore the total size of population is a $(K \times N)$ matrix. In NGOA, the gravitational force on the i^{th} object is calculated as:

$$F_i = \frac{\prod_{j \neq i} m_i.m_j.(K \times X_i(t) - \sum_{j \neq i} X_j(t))}{\sum_{j \neq i}((x_{i1} - x_{j1})^2 + ... + (x_{in} - x_{jn})^2) + I_\epsilon} \tag{4.14}$$

where m_i is defined by the value of the inverse objective function value in a minimization problem, equation 4.15. In a maximization objective function, there is no need to invert the objective function value. In equation 4.15, I_ϵ is added to denominator to prevent dividing by zero when the distance between masses becomes zero.

$$m_i = \frac{1}{ObjectiveFunctionValue_i + I_\epsilon} \tag{4.15}$$

Following the calculation of the gravitational force on the i^{th} mass, assuming a unit time length, the new speed of the object is:

$$V(t+1)_i = \frac{g a_i}{min(a_j|_{j=1:K})} + V(t) \tag{4.16}$$

The function a_i represent the acceleration of mass X_i, and the function $min(a_j|_{j=1:K})$ finds the minimum acceleration between all masses. Here, g is the gravity constant.

Having the speed of the system at $t + 1$ and the previous location of the i^{th} mass at $X_i(t)$, the position in the next iteration is adjusted by:

$$X(t+1)_i = V(t+1)_i + X(t)_i \tag{4.17}$$

It is worthy to mention that adding a random movement of the particles up to a specific iteration number adds a randomization factor and speeds up the convergence rate. This is done by adding a random vector to some of the worst variables. In addition, replacing the worst variables of each iteration with the best of all past generations moves the average of all point toward the optimal points.

In this application $N = 3$, which corresponds to the three variables derived from the histogram-based brain segmentation algorithm. These three variables are G, i.e., the length of the averaging window, W, i.e., the length of a rectangular convolution window (Win), and Thr, i.e., the threshold of cutoff borders as explained in section II. The equations 4.14 to 4.17 are iteratively calculated until the objective function or the iteration number is met or the $V(t+1)_i$ becomes lower than a threshold value.

4.2.3 Convergence of N-Dimensional Gravitational Optimization Algorithm

The initial population and the number of iterations are two factors that affect the convergence rate in the evolutionary optimization algorithms. In gravitational optimization algorithm the gravity constant, g, controls the acceleration rate of the optimization. The higher value of g, the higher the acceleration rate will be.

In spite of all of these considerations, one may not see the objective value satisfaction since the convergence rate is also dependent to the nature of the objective

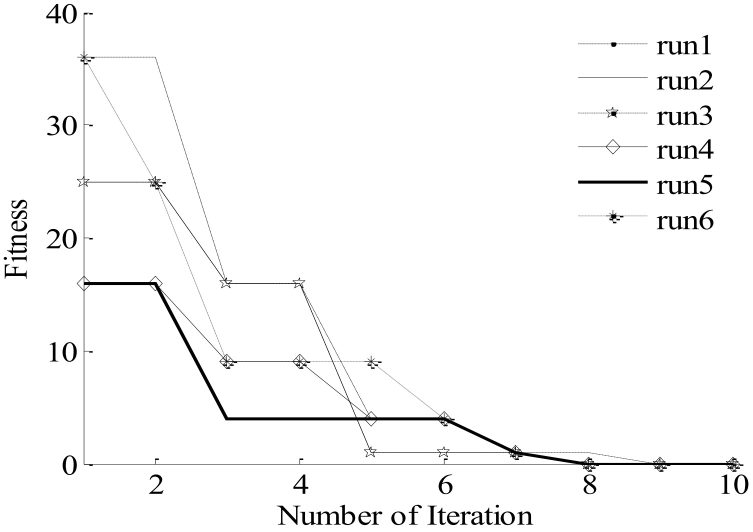

Figure 4.8: Convergence of n-dimensional gravitational optimization for six successive runs

function. For example, strictly speaking, a second order function has only one local and global maximum. However, summing this function with a low value random function increases the number of local maximums or minimums. This idea is employed here to increase the chance of convergence. In other words, the convergence of the optimization algorithm is not guaranteed but adding a low value random function I_r, with a growing rate g_r, to the preprocessed function I_O, during the optimization process increases the convergence chance. The size of I_r will be the same as function I_O. The initial amplitude of the I_r is about one percent of I_O values. This leads to a random but slight movement of local maximums along the intensity vector. These movements increase the chance of optimization convergence immensely. Fig. 4.8 illustrates convergence of n-dimensional gravitational optimization algorithm for several different runs. The whole procedure for brain lesion segmentation is summarized in Fig.4.9.

4.3 Experimental Results

4.3.1 Database and Image Acquisition

For stroke lesion analysis, 12 subjects (6 with stroke and 6 healthy, female 5, mean age of 57.23, and age standard deviation of 10.9, less than one months after stroke) were scanned in this study. All MR images were attained on a 3T Siemens Avanto scanner (Germany). High-resolution 3-D FLAIR brain MRI images were acquired, with the following characteristics: repetition time (TR) = $6000ms$, echo time (TE) = $128ms$, inversion time = $2200ms$, one acquisition, flip angle = $90\circ$, field of view (FOV) = $71mm$, 46 slices, voxel size = $1mm \times 1mm \times 1mm$, and in-plane matrix = 256×256. Prior to scanning, all participants gave written informed consent according to the guidelines of the University of Miami Institutional Review Board. Participants were not paid for participation.

The ground truth is prepared by labeling the ischemic stroke lesion by an expert. In this study the DWI sequences are used for this purpose. Cerebral ischemia pathophysiology involves variation of brain water volume even in its earliest steps, and DWIs sensitivity to changes in tissue water content allows the detection of ischemic damage to the brain even within one hour after onset [93].

Here, sequences with stroke lesion and tumor lesion are called SL and TL, respectively. The sequences without lesion, which are healthy, are called HD for DWI and HT for T1-w.

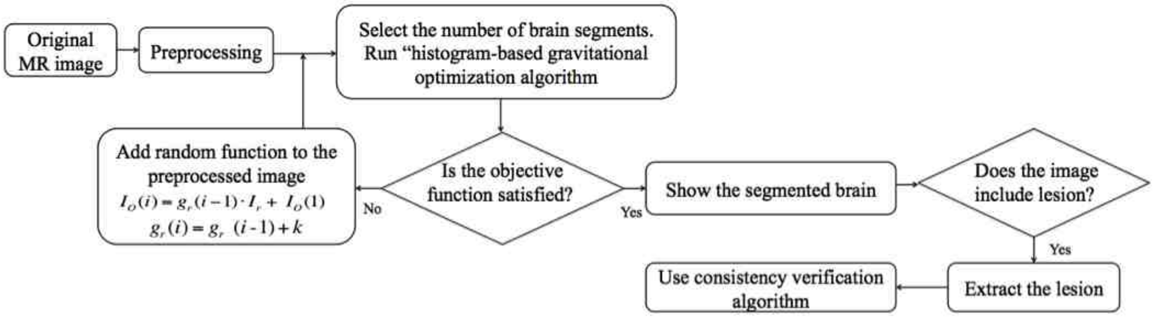

Figure 4.9: Flowchart of the lesion detection

4.3.2 Pre-processing

Preprocessing includes three parts: noise reduction using low pass filter (Gaussian filter), background segmentation, and normalization.

Noise Reduction: Gaussian Filter is a low-pass spatial frequency filter where all elements in this filter are weighted according to a Gaussian (Normal) distribution. Depending on the mean and the variance value, (μ, σ), in the Gaussian distribution, the convolution of this kernel with the image results in a smooth image [92]. Results of applying Gaussian filters with different variance values are represented in Fig. 4.10. *SL1* is filtered out using the Gaussian filter using two different σ that are depicted in Fig. 4.10. It is seen that higher value for sigma (such as $\sigma = 4$) blurs the image more; therefore, the low value for σ is preferred.

Background Segmentation: Due to the prior knowledge of the background intensity values, which is zero here, it is necessary to exclude the background from the calculations wherever the histogram of the image is evaluated. The reason for doing this is that the background normally has much higher number of pixels than the brain. Using Gaussian filter in previous step helps to remove zero intensity values inside the brain part. Therefore, background separation is done excluding pixels with zero intensity from intensity histogram.

Normalization: In order to achieve dynamic range consistency, the image is normalized using the following equation.

$$I_N = (I - Min)/(Max - Min) \tag{4.18}$$

in which Max and Min are maximum and minimum of image intensity [92].

4.3.3 Brain MRI Segmentation

Original image of *SL1 with stroke lesion* is represented in Fig. 4.10(a). The segmentation of *SL1* into two, three and four segments is depicted in Fig. 4.11. Correspondingly, Fig. 4.12 displays the segmentation of *SL1* into five, six and twelve segments. It is seen that after two levels of segmentation the stroke lesion appears in the segmented image. In addition, after three levels of segmentation the tumor lesion appears in the segmented image. It is also met that in high levels of segmentation some of the segments are visually indiscriminative; however, there is still a clear appearance of the lesion in the segmented image. Figure 4.14 illustrates the original image of *SL2 with stroke lesion* and its segmentation into three and four segments. Figure 4.13 and 4.15 show the original healthy image of *HD1* and *HD2* and their segmentation into three and four segments, correspondingly.

Figure 4.16, 4.17, 4.18, and 4.19 show the results of five steps of histogram-based brain segmentation algorithm for segmentation of DWI image of *SL1 with stroke lesion* into three, four, five, and twelve segments, respectively. In these diagrams, part (a) corresponds to image histogram after step 2. Part (b) shows the local maximums of the histogram in step 3. Part (c) illustrates the results of step 4. Part (d) displays the results of step 5 and 6. In all these Figures, red dots are initial lower and upper cutoff borders, which are the results of step 5, and black dots are final lower and upper cutoff borders, which are the results of step 6 of histogram-based brain segmentation algorithm. Figure 4.20 and 4.21 show the similar results for segmentation of DWI image of *HD1 which is healthy* into three and four segments. Part (a) to (d) illustrate the same steps as mentioned above.

4.3.4 Stroke Lesion Detection

Comparing the of positions of cutoff borders in part (d) of Fig. 4.16, 4.17, 4.20, and 4.21, it is clear that the last segment's intensity width differs for healthy and lesion slices. The brain images, which include lesions are called lesion slices in this paper. After segmentation of the brain into L segments, L^{th} segment's intensity width for lesion slices is much smaller than the healthy ones. The following criterion is defined as the first condition for stroke lesion slice detection:

$$[X_{up-final}(L) - X_{low-final}(L)] < q \tag{4.19}$$

Equation 4.19 is interpreted as if L^{th} segment's width is less than q, the slice is considered as lesion slice and vise verse as healthy one. Here, q is selected as 1.8.

Comparing part (d) of Fig. 4.16 with 4.20, and also 4.17 with 4.21, one can see the obvious difference in movements of $(L-1)^{th}$ segment's initial and final lower and upper cutoff borders in healthy and lesion slices. Initial and final cutoff borders are shown with red dots and black dots, respectively. After segmentation of the brain into L segments, following criterion is defined as the second condition for non-stroke slice detection:

$$[X_{up-final}(L-1)-X_{low-final}(L-1)] > P.[X_{up-initial}(L-1)-X_{low-initial}(L-1)] \quad (4.20)$$

Equation 4.20 is interpreted as if the intensity width of final segment is larger than P times of the initial segment's intensity width. Here, P is selected as 1.2. The results show that for higher number of segments the movement of cut-off borders at segment $(L-1)$ is more discriminative than that of the lower number of segmentation. Therefore, for detection of the stroke lesion slice the high number (> 5) of segmentation is preferred. For example, the brain can be segmented into eight or twelve segments. However, for lesion extraction from a detected lesion slice, the lower number (< 5) of segmentation is more preferable since it covers wider intensity range around the stroke with a distributed intensity. Our experiments show that for stroke lesion extraction, $L = 3$ is satisfactory. All in all, for a complete stroke lesion detection and segmentation two separate segmentations are needed. Initially, the brain image is segmented into a high number of segments (here 12) and the slice including stroke lesion is detected. After stroke lesion detection, the brain image is segmented into three segments and the last segment is chosen to be the stroke lesion. Here, considering logical OR between condition one and condition two, slices including stroke lesion are detected with 94.7% accuracy.

4.3.5 Stroke Lesion Segmentation

After detection of slices including stroke lesion, the brain image is segmented into three segments or four segments. Because of high intensity of stroke lesion, the stroke

Table 4.1: Result of lesion segmentation using histogram-based gravitational optimization algorithm

Num of Segms	Accuracy	Specificity	Sensitivity	Similarity index	Accuracy after CV
3 segments/Stroke	89.4 ± 1.6	78.4 ± 1.1	91.1 ± 1.3	85.7 ± 1.4	91.5 ± 1.2
4 segments/Stroke	86.1 ± 1.5	90.4 ± 1.2	75.8 ± 0.8	81.1 ± 2.1	88.7 ± 1.1
4 segments/Tumor	85.2 ± 1.1	93.7 ± 0.9	92.5 ± 1.6	74.1 ± 1.7	88.1 ± 0.9
5 segments/Tumor	82.3 ± 2.2	88.8 ± 1.2	87.3 ± 2.0	70.1 ± 1.9	86.2 ± 1.8

normally is positioned in the last segment and therefore with extracting the last segment, the stroke lesion can be extracted. The results show that the stroke lesion extracted with segmenting the brain into four segments has smaller area than the labeled lesion, and includes less false positives. However, lesions extracted with brain segmentation into three segments are closer to the labeled lesion but include more false positives. Performance of histogram-based gravitational optimization algorithm is quantified using four commonly used performance criteria: sensitivity, specificity, accuracy, and similarity index (as explained in Section 4.1), which is presented in Table4.1. Table 4.1 shows it is indicated that segmenting the brain into three segments for stroke lesion segmentation provides us with higher accuracy. Results of the segmentation for two different stroke lesion samples are shown in Fig. 4.22, 4.23, 4.24 and 4.25.

4.3.6 Decreasing False Positives

The misclassification of the pixels is an important problem in the segmentation of in MR Images. This misclassification creates false negatives and false positives, which are mostly due to the partial volume effect [10]. The border voxels are generally known as partial volume voxels and contain a mixture of tissues. This effect is generated by the low spatial resolution of the MRI and makes determining the boundaries of the brain tissues very difficult. The misclassified pixels can be grouped into the following groups [10]:

- The false negatives which are in the boundary of the lesions and the grey matter. Overlapping of the intensities of the lesions and grey matter causes the lesions to appear as grey matter where no grey matter is expected. This problem is more severe for the small lesions.
- The false positives which are in the boundary of the brain. Averaging the intensities of CSF and grey matter in the boundary of the brain makes pixels with intensities similar to those of the lesions, especially in T2-weighted and proton density-weighted images.
- The false negatives which are in the boundary of the brain. The same problem causes small lesions missed in the grey matter.
- The false negatives which are in the vicinity of the ventricles. Because the intensities of the brain lesions in the vicinity of the ventricles are similar to those of the CSF, these periventricular lesions may be misclassified as CSF in T1-w, T2-w and PD-w images, not in FLAIR images.

A consistency verification (CV) algorithm is used to remove the false positives and false negatives [94, 95]. That is, we use a majority filter to alter the pixel labels that are not consistent with their neighbor labels in a certain neighborhood. For instance, if the center pixel of a window is labeled as tumor while the majority of the surrounding pixels are labeled as healthy, the center pixels label is simply switched to healthy. On the other hand, if a pixel inside the tumor area is mistakenly labeled as healthy, since the majority of the surrounding labels are tumor, it will switch to tumor. Here, consistency verification is applied in a 5×5 neighborhood window. The results of applying consistency verification algorithm are depicted in part (d) of Fig. 4.22, 4.23, 4.24 and 4.25. Furthermore, lesion segmentation accuracy after using consistency verification algorithm is presented in Table 1. Despite using consistency verification algorithm, we still have false positives, which reduce the recognition rate in the tumor lesion segmentation. As another limitation, our method cannot detect very small lesions ($< 1cm^3$). Further algorithm refinement to address those drawbacks comes at the expense of computational cost. However, higher recognition rate can outweigh the additional computational burden in non-online procedures, which can be considered in future research. Table 4.2 compares the limitations of the state-of-the-art algorithms [9, 79–82, 84, 86–88, 96] with this proposed method.

4.3.7 Tumor Lesion Detection and Segmentation

We implement our proposed method, histogram-based gravitational optimization algorithm, on T1-weighted MR images including tumor lesions. Some examples of this implementation are presented here. Original image of *TL1 with tumor lesion* is depicted in Fig. 4.26(a). The segmentation of *TL1* into two, three and four segments is depicted in Fig.4.27. Fig. 4.28 display the segmentation of *TL1* into five, six and twelve segments. It is seen that after three levels of segmentation the tumor lesion appears in the segmented image. Figure 4.29 and 4.30 show the original image of

TL2 with tumor lesion and *HT1 which is healthy* and their segmentation into four and five segments, correspondingly.

Figure 4.31 and 4.32 show the results of five steps of histogram-based brain segmentation algorithm for T1-w image of *TL1 with tumor lesion* for four and five levels of segmentation, respectively. Figures 4.33 and 4.34 show the similar results for segmentation of T1-w image of *HT1 which is healthy* for four and five levels of segmentation, respectively. Part (a) to (d) illustrate the results of the same steps as mentioned above. Likewise, red dots are initial lower and upper cutoff borders, which are results of step 5, and black dots are final lower and upper cutoff borders, which are results of step 6.

For tumor slice detection, positions of cutoff borders in the second segment differ for healthy and lesion slices when brain is divided into four segments. The following criterion is defined as the condition for tumor lesion detection:

$$T = [X_{low}[2] < q_1 \bigcap X_{up}[2] < q_2] \tag{4.21}$$

where $X_{low}[2]$ refers to the lower cutoff boundary of second segment, and $X_{up}[2]$ refers to the upper cutoff boundary of second segment. q_1 is specified as 2.25, and q_2 is specified as 4.85. The slices including tumor lesion are detected with 89.3% accuracy.

For tumor lesion segmentation, the brain is segmented into four segments or five segments. Here, the tumor is positioned in the second segment. Therefore, tumor lesion can be segmented with extracting the second segment. Performance of the proposed algorithm in tumor lesion segmentation is presented in Table 4.1. Table 4.1

shows that segmenting the brain into four segments for tumor lesion segmentation provides us with higher accuracy, which is 86.2%. Histogram analysis limits the extracted information to the number of pixels in the specific gray levels and does not include any region-based information. Consequently, the accuracy of a histogram-based method is also limited. Since we are looking for higher accuracy in tumor lesion segmentation, a texture-based method is investigated.

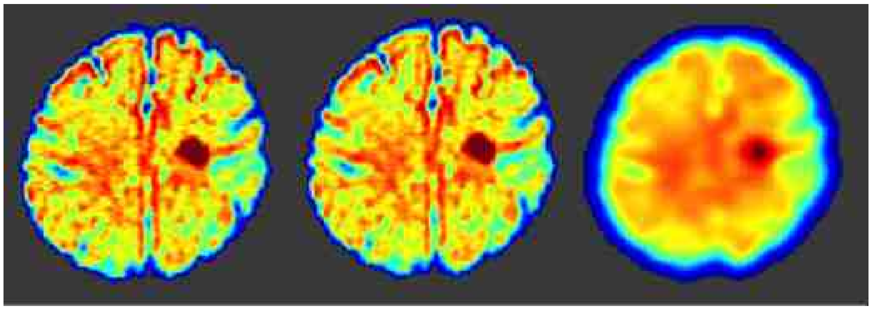

Figure 4.10: Stroke lesion: (a) original image, (b) filtered image using Gaussian filter with $\sigma = 0.1$, (c) filtered image using Gaussian filter with $\sigma = 4$

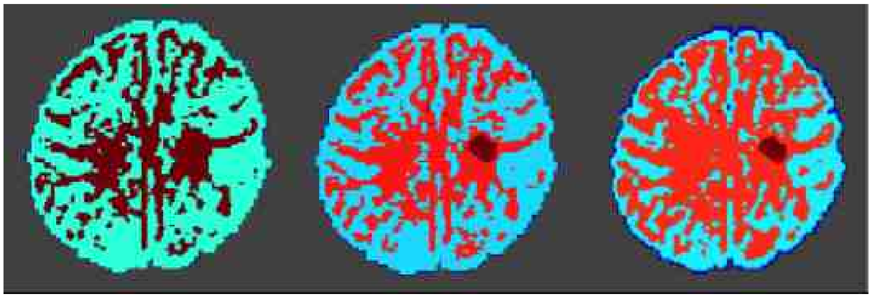

Figure 4.11: Stroke lesion SL1: dividing into two (a), three (b), and four (c) segments

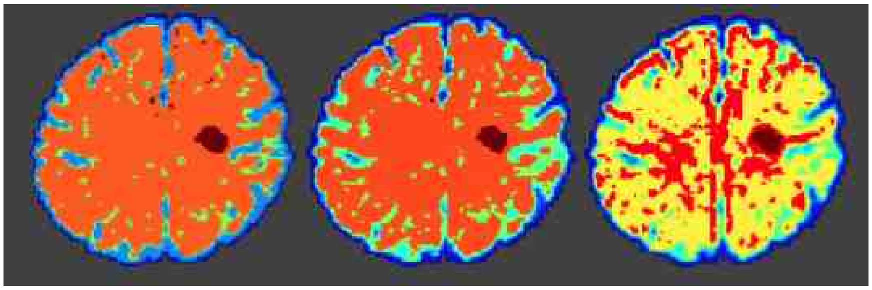

Figure 4.12: Stroke lesion SL1: dividing into five (a), six (b), and twelve (c) segment

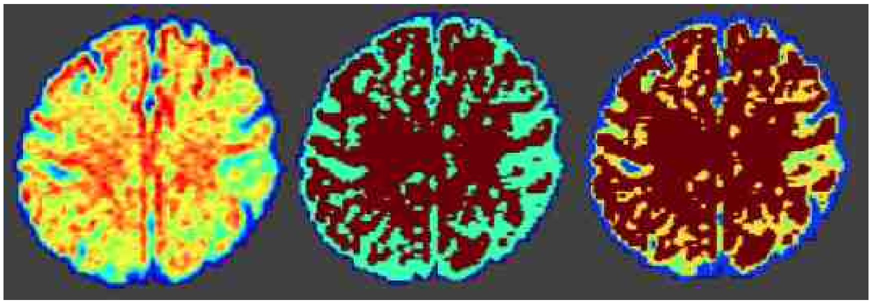

Figure 4.13: Healthy HD1: original image (a), its dividing into three (b), and four (c) segments

Figure 4.14: Stroke lesion SL2: original image (a), its dividing into three (b), and four (c) segments

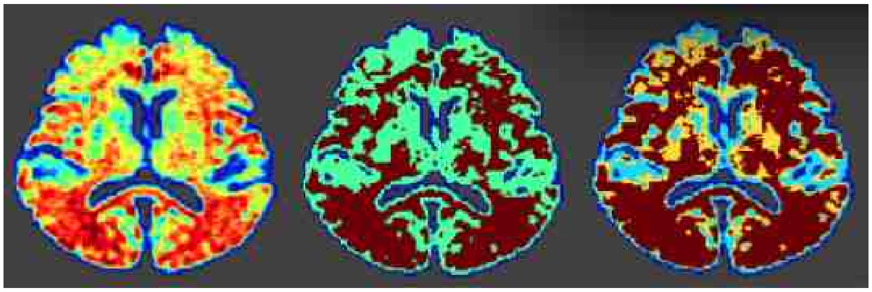

Figure 4.15: Healthy HD2: original image (a), its dividing into three (b), and four (c) segments

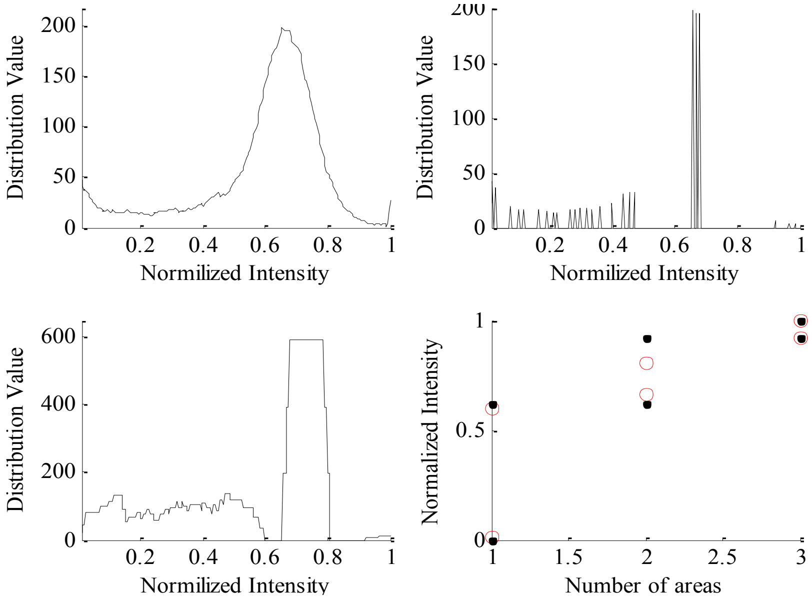

Figure 4.16: 3 level segmentation of SL1 (with stroke lesion): (a) intensity histogram after step 2, (b) the local maximums of the histogram in step 3, (c) results of step 4, (d) results of step 5 and 6

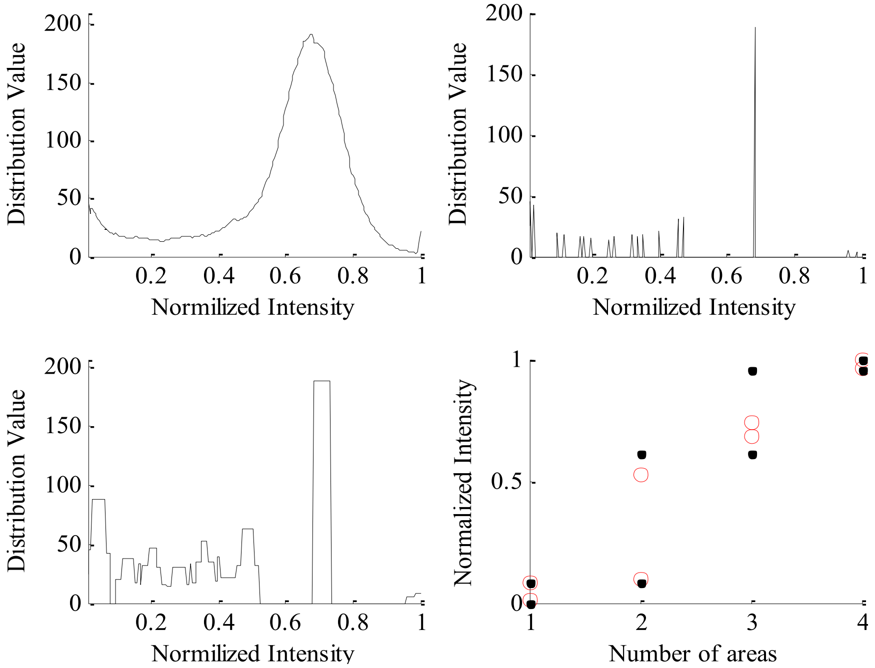

Figure 4.17: 4 level segmentation of SL1 (with stroke lesion): (a) intensity histogram after step 2, (b) the local maximums of the histogram in step 3, (c) results of step 4, (d) results of step 5 and 6

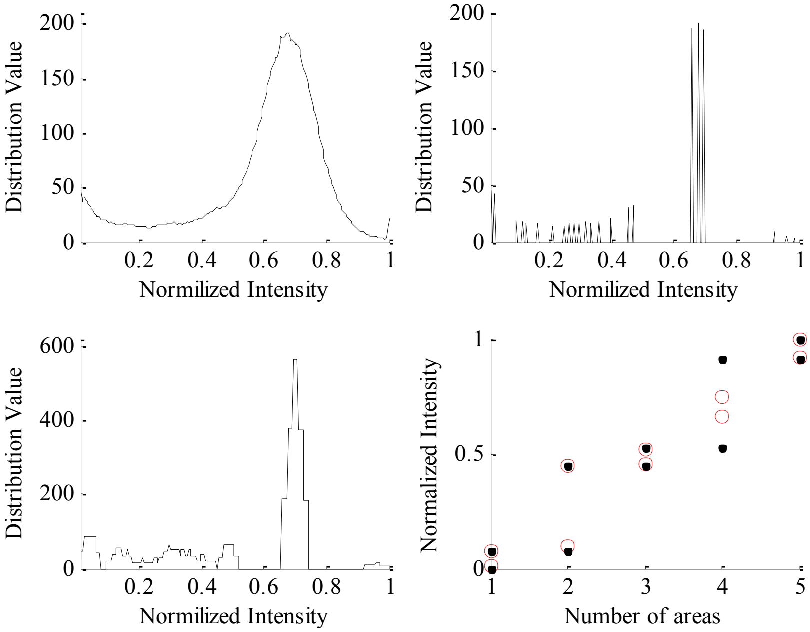

Figure 4.18: 5 level segmentation of SL1 (with stroke lesion): (a) intensity histogram after step 2, (b) the local maximums of the histogram in step 3, (c) results of step 4, (d) results of step 5 and 6

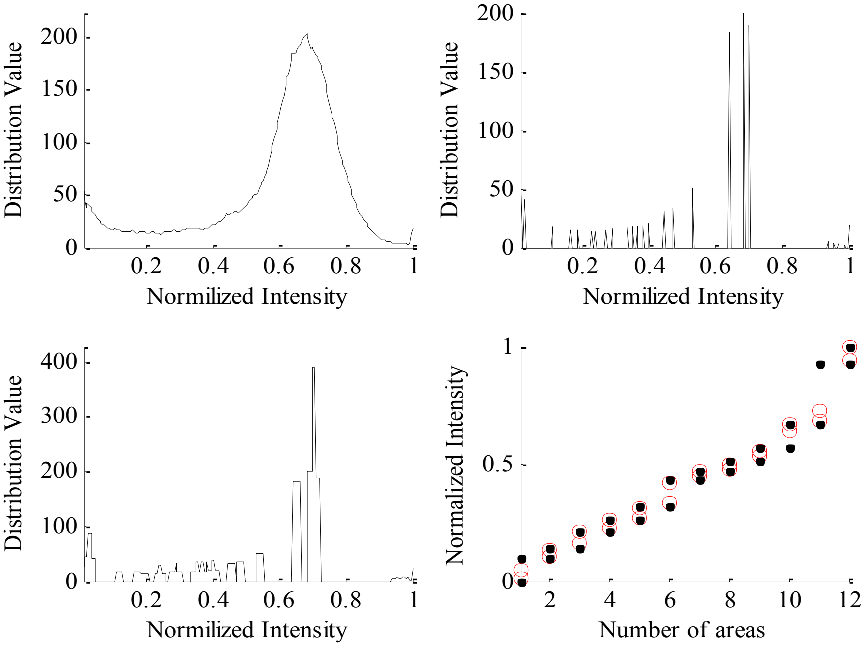

Figure 4.19: 12 level segmentation of SL1 (with stroke lesion): (a) intensity histogram after step 2, (b) the local maximums of the histogram in step 3, (c) results of step 4, (d) results of step 5 and 6

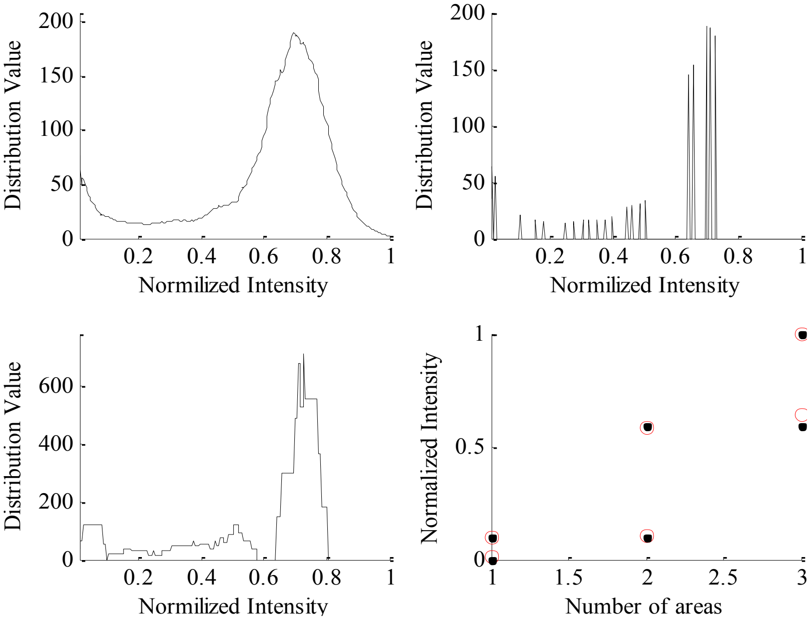

Figure 4.20: 3 level segmentation of HD1 (Healthy): (a) intensity histogram after step 2, (b) the local maximums of the histogram in step 3, (c) results of step 4, (d) results of step 5 and 6

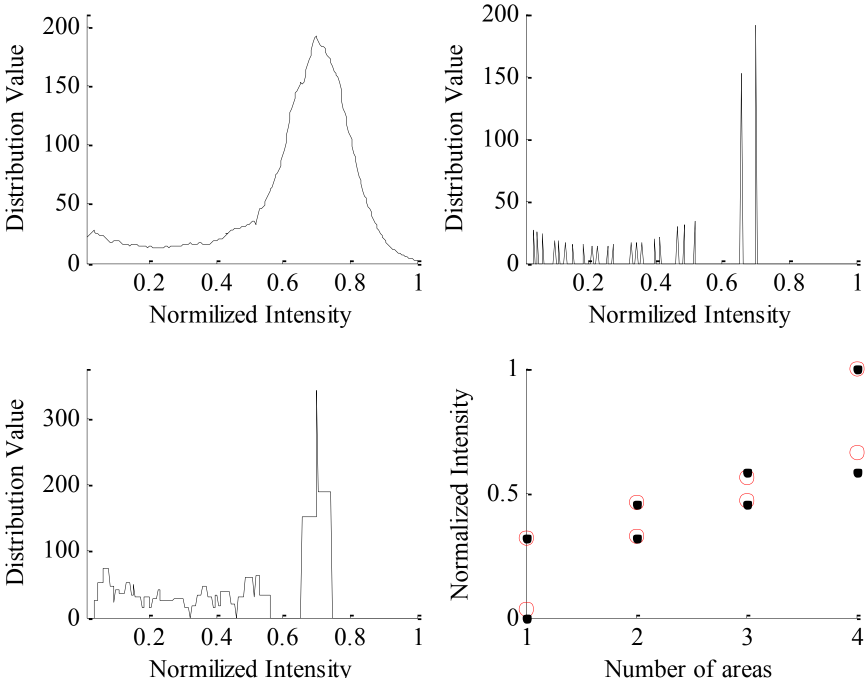

Figure 4.21: 4 level segmentation of HD1 (Healthy): (a) intensity histogram after step 2, (b) the local maximums of the histogram in step 3, (c) results of step 4, (d) results of step 5 and 6

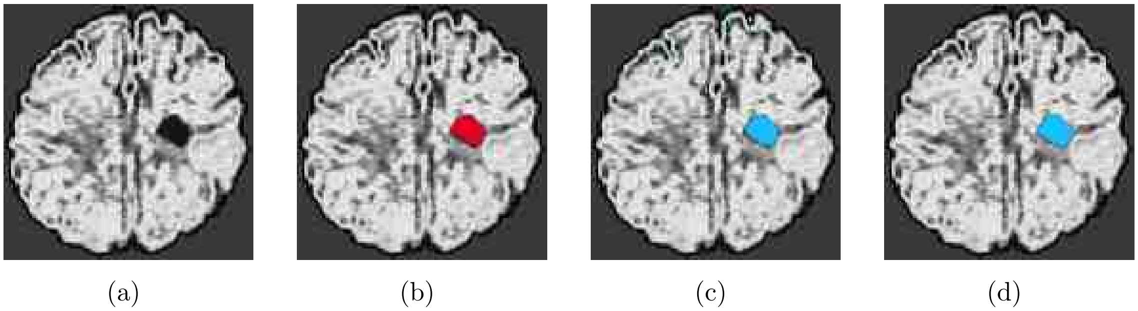

(a) (b) (c) (d)

Figure 4.22: Stroke lesion SL1: original image (a), extracted stroke lesion manually (b), extracted stroke lesion after three levels of segmentation (c), extracted stroke lesion after consistency verification (d)

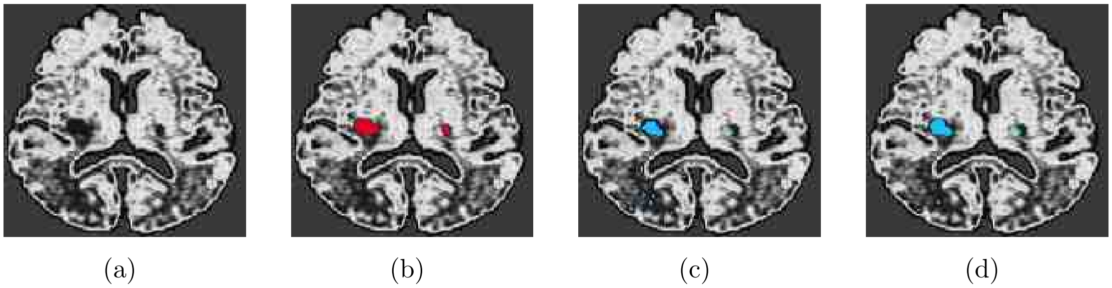

(a) (b) (c) (d)

Figure 4.23: Stroke lesion SL2: original image (a), extracted stroke lesion manually (b), extracted stroke lesion after three levels of segmentation (c), extracted stroke lesion after consistency verification (d)

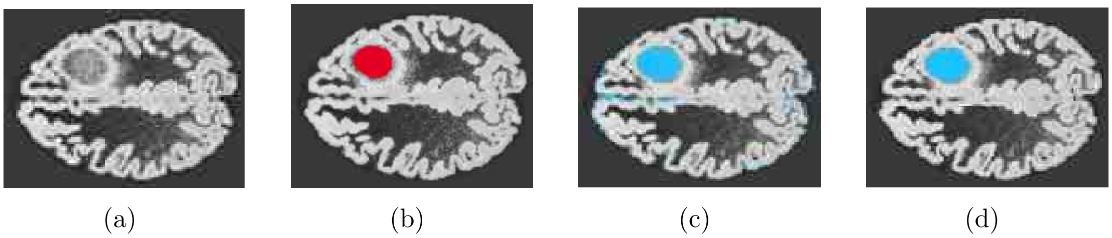

(a) (b) (c) (d)

Figure 4.24: Tumor lesion TL1: original image (a), extracted tumor lesion manually (b), extracted tumor lesion after four levels of segmentation (c), extracted tumor lesion after consistency verification (d)

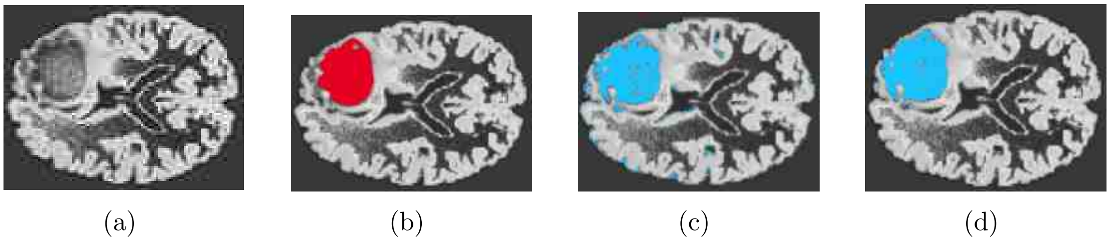

Figure 4.25: Tumor lesion TL2: original image (a), extracted tumor lesion manually (b), extracted tumor lesion after four levels of segmentation (c), extracted tumor lesion after consistency verification (d)

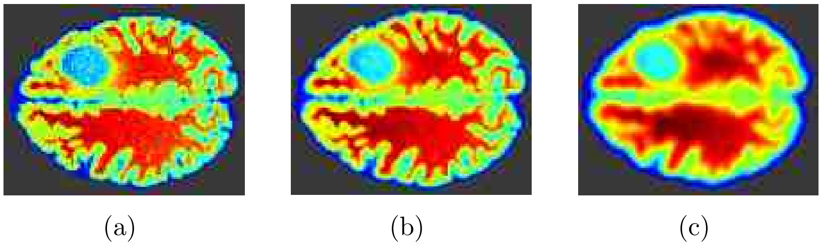

Figure 4.26: Tumor lesion: (a) original image, (b) filtered image using Gaussian filter with $\sigma = 0.1$, (c) filtered image using Gaussian filter with $\sigma = 4$

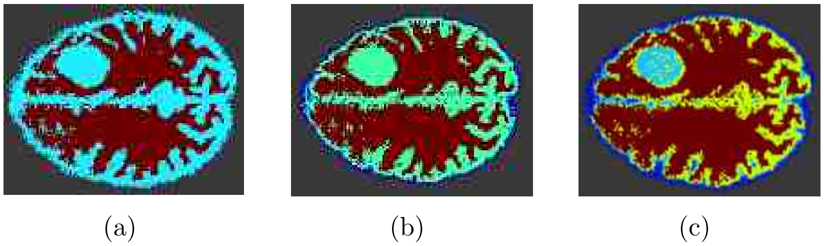

Figure 4.27: Tumor lesion TL1: dividing into two (a), three (b), and four (c) segments

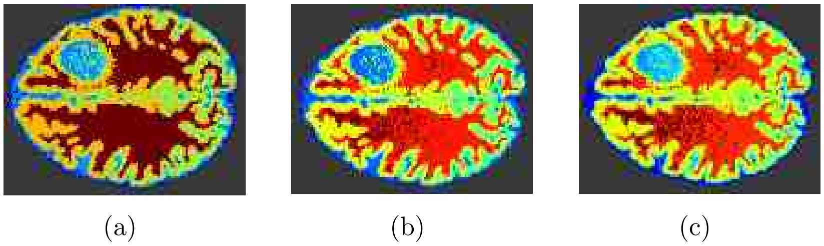

Figure 4.28: Tumor lesion TL1: dividing into five (a), six (b), and twelve (c) segments

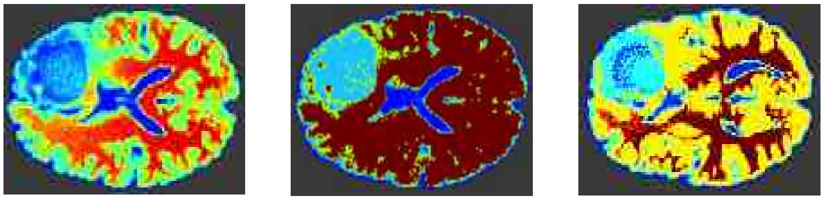

(a) (b) (c)

Figure 4.29: Tumor lesion TL2: original image (a), its dividing into four (b), and five (c) segments.

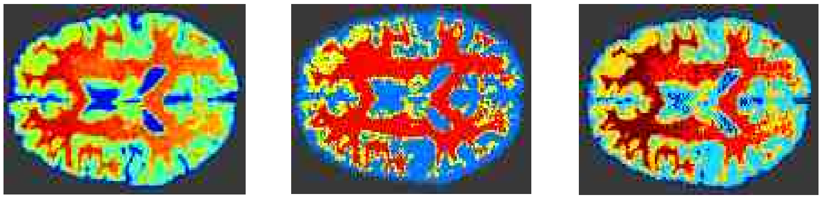

(a) (b) (c)

Figure 4.30: Healthy HT1: original image (a), its dividing into four (b), and five (c) segments

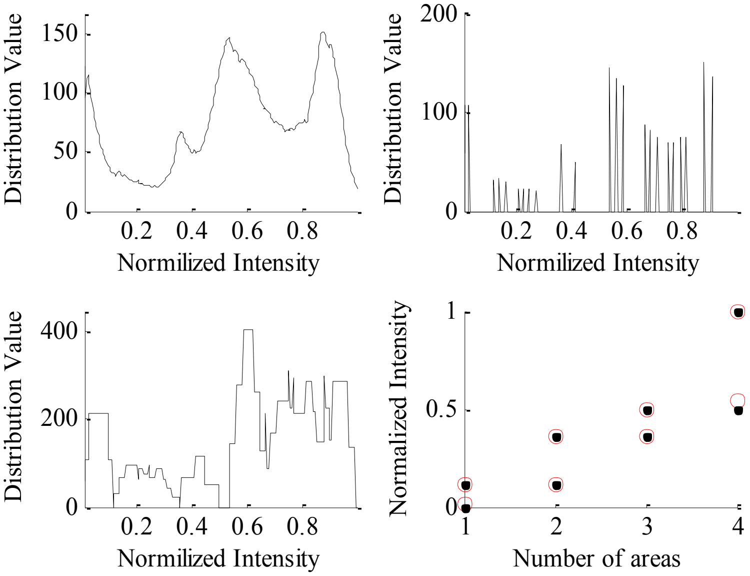

Figure 4.31: 4 level segmentation of TL1 (with tumor lesion)): (a) intensity histogram after step 2, (b) the local maximums of the histogram in step 3, (c) results of step 4, (d) results of step 5 and 6

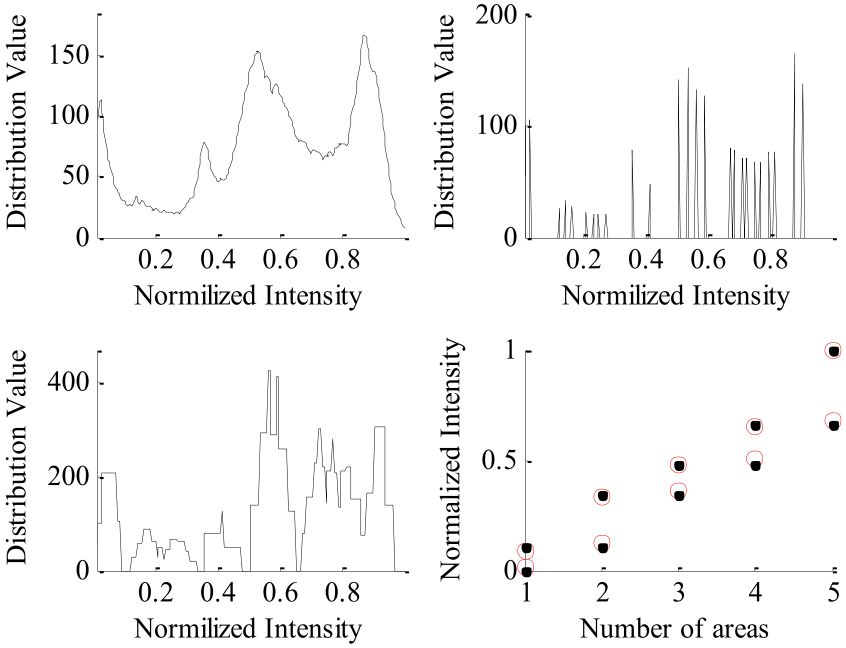

Figure 4.32: 5 level segmentation of TL1 (with tumor lesion)): (a) intensity histogram after step 2, (b) the local maximums of the histogram in step 3, (c) results of step 4, (d) results of step 5 and 6

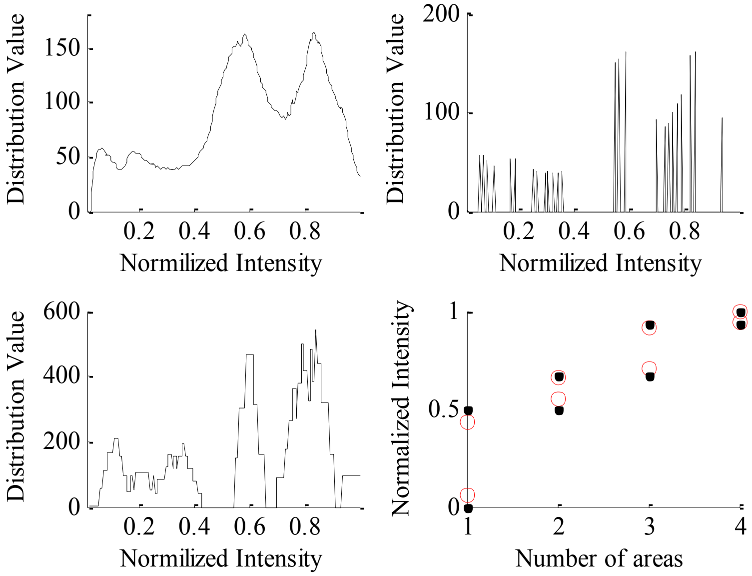

Figure 4.33: 4 level segmentation of HT1 (healthy)): (a) intensity histogram after step 2, (b) the local maximums of the histogram in step 3, (c) results of step 4, (d) results of step 5 and 6

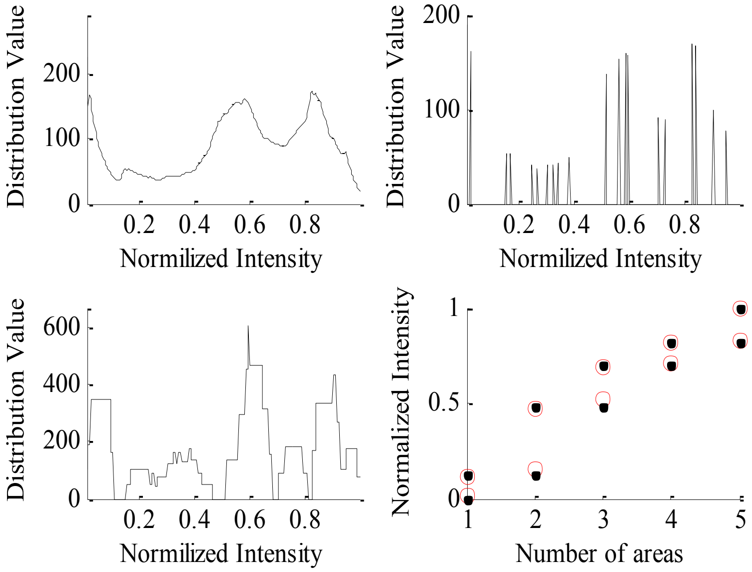

Figure 4.34: 5 level segmentation of HT1 (healthy)): (a) intensity histogram after step 2, (b) the local maximums of the histogram in step 3, (c) results of step 4, (d) results of step 5 and 6

Table 4.2: Comparing HGOA with other methods

Algorithm / Dep. on	[96]	[86]	[87]	[80]	[88]	[84]	[82]	[81]	[9]	[79]	HGOA
Bias correction	√	√	√	-	-	-	-	-	-	-	-
Registration	√	√	√	√	√	-	-	-	-	-	-
Multi-spectral MRI	√	√	-	-	-	-	-	-	-	-	-
Initial assumptions	-	-	-	√	√	√	-	-	-	-	-
High quality data	-	-	-	-	-	-	√	√	√	-	-
Manual intervention	-	-	-	-	-	-	-	-	-	√	-
Multiscale classification	-	-	-	-	√	√	-	-	-	-	-
Size of lesion	-	-	-	-	-	-	-	-	√	-	√
High computational complexity	-	-	-	-	-	-	√	√	√	√	-

4.4 Conclusion

In this work, a novel method for stroke and tumor lesion detection and segmentation in the brain MR images is presented. The method is called the histogram-based gravitational optimization algorithm, which is based on applying enhanced gravitational optimization algorithm on histogram analysis results. This algorithm uses histogram-based techniques to determine the initial set of brain segments, then applies a gravitational optimization based algorithm to reduce the number of segments, and finally uses thresholding to detect the tumor or stroke lesions. New set of formulae are designed to extend the old space gravitational optimization from 2D to ND, and also to decrease the chance of optimization algorithm to be drawn into local optimal solutions. Another advantage of the proposed method is that it is independent of atlas registration, prior anatomical knowledge, or bias corrections that restrict the general application of many state-of-the-art methods. Reliance on atlas registration in other algorithms implies that their accuracy is dependent on the how well the atlas is constructed and how well the registration algorithm can register the test data to the atlas. Prior anatomical knowledge dependence implies that such algorithms must be trained to incorporate such information, which can lead to error. The need for bias correction in many other algorithms also introduces errors into the data to be analyzed, and thus adds inaccuracy and difficulties with consistence of the final results. As this algorithm has no reliance on any of these, it does not suffer from inherent errors.

The other contribution of this method is in the use of single-spectral MRI. While using multi-spectral MR images address the intensity similarities between lesion and healthy tissues, in some of the practical clinical situations only one type of anatomical MR image is collected due to time and cost and patient situation limitations [9,12]. In addition, use of multi-spectral data implies the need to ensure that each of the spectra must be properly registered. Failure to do the registration can result in misalignment of suspected lesions in the different spectra.

The algorithm is also fully automatic and computationally light as it involves the application of a single algorithm for both lesion detection and segmentation. Additionally, despite some other methods' need to have the initial assumptions, such as a given number of tissue classes or a multi-scale classification, there is no requirement for such information. This makes the proposed algorithm much more robust and more general than other methods.

The experimental results on both synthetic and real MR images show that the proposed algorithm, when applied by itself, provides an accuracy of almost 90% for stroke lesions and 85% for tumor. With the application of a consistency verification algorithm to reduce the false-positives, the accuracy rates climb to 91% and 88% respectively. This compares well with other algorithms without suffering from some of the drawbacks as stated earlier. The accuracy and computational simplicity of the proposed method make it suitable as an additional tool for the clinician. Moreover, the automated segmentation can be used to more consistently calculate the lesion volumes and track them in the treatment progress.

The major shortcoming of the presented algorithm is that it is incapable of detection of hardly visible lesions. Another shortcoming is the presence of false positives, which affects the recognition rate, especially in the tumor lesion segmentation. In spite of the fact that this algorithm is fast and computationally efficient, the histogram analysis limits the extracted information to the number of pixels in the specific gray levels and does not include any region-based information. Consequently, the accuracy of histogram-based methods is limited. In order to improve the obtained tumor segmentation accuracy, another method is suggested in the next chapter, which is based on brain texture analysis.

CHAPTER 5

Tumor Lesion Detection and Segmentation Using Texture-Based Statistical Characterization

5.1 Overview

As it was mentioned earlier, segmentation is one of the key challenges in machine learning and computer vision realm. In medical diagnostics field, brain tumor segmentation is an important and demanded application, as it provides medical experts the information associated to lesions, which helps to control and diminish the effects of the disease. There are intensity similarities between brain lesions and some normal tissues that can result in confusion within the algorithm. For example, in T1-weighted MR images, a tumor lesion has similar intensities to those of GM or CSF [4]. Owing to this fact, general image segmentation methods are not easily applicable on the brain lesion identification domain. In order to overcome intensity similarities problem, one general solution is using multi-spectral MR images for lesion identification [20–24]. However, as it was mentioned earlier, applying multi-spectral MR images has its own limitations and difficulties [9, 12]. Because of these impediments, brain lesion detection and segmentation using single-spectral anatomical MRI is desirable.

The achieved accuracy of a histogram-based method is limited due to not including any region based information by histogram analysis. Since texture-based brain characterization has been proven to be an effective way of brain analysis, in this chapter, in order to increase the accuracy of brain tumor segmentation, an automated algorithm is proposed for tumor detection and segmentation based on local texture analysis using single contrast MR mechanism. This algorithm includes tumor slice detection, tumor segmentation, and efficacy evaluation of two main feature sets. After dividing the brain into two hemispheres using longest brain diameter, slices containing tumor are detected based on thresholding the mutual information of the histograms of two divided brain hemispheres. The advantage of this technique is its robustness against head rotation. After detecting the image containing tumor, it is fed into the segmentation stage, which localizes the tumor area. The candidate tumor regions are acquired using a sliding window, which sweeps through the whole brain tissue. Using a texture-based classification, the window center is labeled as healthy or tumor. A proposed post-processing method is applied to remove the false positives/negatives. The algorithm is evaluated on NCI-MICCAI database on real and simulated T1-weighted, T2-weighted, and FLAIR MR images separately. The overall process is depicted in Fig. 5.1.

It is obvious that characterization of brain image that differentiates various type of tissue including tumor is very important and depends to a great extent on the choice of extracted features to describe the region of interest or its quasi-homogenous regions [97]. Vast variety of tumors in location, size, shape, and texture makes feature extraction a perplexing task. Moreover, in the MR brain images various tissues such as the white matter, the gray matter, and cerebrospinal fluid have complicated

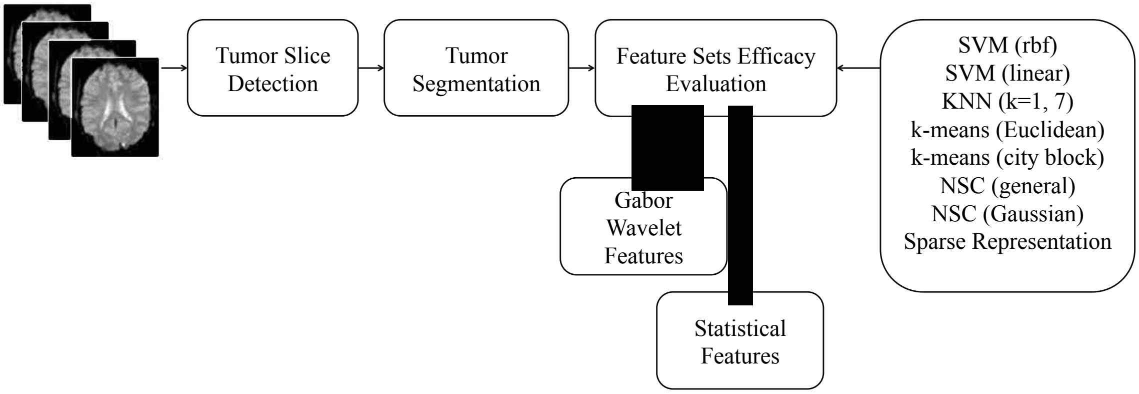

Figure 5.1: Framework of the proposed system

structures that increase difficulty of efficient feature extraction step. In spite of all the studies focusing on extraction of features that might be found useful in tumor segmentation [98–103], the relevant literature has not given a comparison on which feature extraction technique is more efficient in this kind of applications. In this chapter, two most popular main sets of well-established and competent texture-based feature extraction techniques are applied. The first set is Gabor wavelet feature extraction method that is capable of capturing frequency, locality, and orientation, providing multi-resolution texture information about the spatial-domain as well as the frequency-domain [32, 33]. The second set, statistical features extraction methods, include texture-based feature extraction methods, such as gray level co-occurrence matrix (GLCM), histogram of oriented gradient (HOG), grey level run length matrix (GLRLM) methods and etc. These feature extraction methods reflect the relationship between intensity of two image pixels or group of pixels. Furthermore, they estimate image properties related to the first- and second-order statistics [34–37]. Beside the tumor detection and segmentation, another study on the effectiveness and complexity of these two feature extraction methods in this application are offered. To reduce the risk that the attained conclusion is only due to some idiosyncrasies of the employed machine learning technique, the experiments are performed using several classifiers such as SVM, kNN, SRC, NSC, and k-means clustering. Three different MR sequences, *i.e.*, T1-weighted, T2-weighted and FLAIR, are experimented in this study.

5.2 Texture-Based Feature Extraction Methods

The fundamental objective of any diagnostic imaging investigation is tissue characterization [37]. Classic methods concentrate on clustering or morphological operations. But the results are not satisfactory. The texture analysis is a useful way of increasing the information obtainable from medical images [36].

Texture is a property that represents the surface and structure of an Image. Generally speaking, texture can be defined as a regular repetition of an element or pattern on a surface [104]. Image textures can be defined as complex visual patterns composed of entities or regions with sub-patterns with the characteristics of brightness, color, shape, size, etc. An image region has a constant texture if a set of its characteristics are constant, slowly changing or approximately periodic [105]. Texture can be regarded as a similarity grouping in an image [106].

Texture analysis is a major step in texture classification, image segmentation and image shape identification tasks. Texture analysis refers to a class of mathematical procedures and models that characterize the spatial variations within imagery as a means of extracting information. Texture defines local spatial organization of spatially varying spectral values that is repeated in a region of larger spatial scale. Thus, the perception of texture is a function of spatial and radiometric scales.

Descriptors providing measures of properties such as smoothness, coarseness and regularity are used to quantify the texture content of an object. Since an image is made up of pixels, texture can be defined as an entity consisting of mutually related pixels and group of pixels. This group of pixels is called as texture primitives or texture elements, which is called texels.

Mathematical procedures to characterize texture fall into two major categories: statistical, and syntactic.

Statistical approaches compute different properties and are suitable if texture primitive sizes are comparable with the pixel sizes. These include Fourier transforms, convolution filters, co-occurrence matrix, spatial autocorrelation, fractals, etc.

Syntactic and hybrid methods are suitable for textures where primitives can be described using a larger variety of properties than just tonal properties; for example shape description. Hybrid method is combination of statistical and syntactic methods. Using these properties, the primitives can be identified and assigned a label.

Statistical methods has more prevalence and advantages over syntactic techniques. They analyze the spatial distribution of gray values, by computing local features at each point in the image, and deriving a set of statistics from the distributions of the local features [107]. The reason behind this is the fact that the spatial distribution of gray values is one of the defining qualities of texture.

Depending on the number of pixels defining the local feature, statistical methods can be further classified into first-order (one pixel), second-order (two pixels) and higher-order (three or more pixels) statistics [107]. The basic difference is that first-order statistics estimate properties (e.g. average and variance) of individual pixel values, ignoring the spatial interaction between image pixels, whereas second- and higher-order statistics estimate properties of two or more pixel values occurring at specific locations relative to each other.

5.2.1 First-Order Statistical Features

Mean, median, average contrast, intensity energy and entropy, skewness and kurtosis are useful first-order statistical features. Mean is the average value of the intensity of the image. Variance indicates the intensity variations around the mean. Skewness quantifies the symmetry of the histogram around the mean. Kurtosis is the flatness of the histogram. Entropy reveals the randomness of intensity values. These features formula are listed in the following [102] [108].

Mean

$$\mu = \sum_{i=0}^{G-1} iP(i) \tag{5.1}$$

Average contrast

$$\sigma^2 = \sum_{i=0}^{G-1} (i-\mu)^2 P(i) \tag{5.2}$$

Skewness

$$\mu_3 = \sigma^- 3 \sum_{i=0}^{G-1} (i-\mu)^3 P(i) \tag{5.3}$$

Kurtosis

$$\mu_4 = \sigma^- 4 \sum_{i=0}^{G-1} (i-\mu)^4 P(i) - 3 \tag{5.4}$$

Energy

$$E = \sum_{i=0}^{G-1} [P(i)]^2 \tag{5.5}$$

Entropy

$$H = -\sum_{i=0}^{G-1} P(i) \log_2 P(i) \tag{5.6}$$

where G is maximum gray level of the image, $P(i)$ is probability density of occurrence of the intensity levels which is obtained from:

$$P(i) = h(i)/N \tag{5.7}$$

where $h(i)$ is total number of pixels with intensity level i and N is total number of pixels in the image.

5.2.2 Grey Level Run Length Method Features

GLRLM is a spatial domain second-order statistical method that pertains a quantitative parameter to spatial domain grey level value. In GLRLM, a texture primitive called grey level run length is considered as the maximum collinear attached set of pixels with the same grey level. The grey level runs are defined through the grey level of the run, the length of the run, and the direction of the run $[109, 110]$. To calculate GLRLM, the number of grey level runs of various lengths should be figured out. In the grey level run length matrix of $R(\theta) = [r'(i,l|\theta)]$, the element $r'(i,l|\theta)$ provides an estimation of the number of times an image contains a run with length of l, for grey level i, in the direction of angle θ. The grey level run length matrices $R(\theta)$ are calculated for 0, 45, 90 and 135 degrees. The following five GLRLM features are calculated using these matrices:

1) SRE: Short Run Emphasis

$$RF_1(R(\theta)) = \frac{1}{T_P} \sum_{i=0}^{G-1} \sum_{l=1}^{N_R} \frac{r'(i,l|\theta)}{l^2} \tag{5.8}$$

2) LRE: Long Run Emphasis

$$RF_2(R(\theta)) = \frac{1}{T_P} \sum_{i=0}^{G-1} \sum_{l=1}^{N_R} j^2 r'(i, l|\theta) \tag{5.9}$$

3) GLD: Grey Level Distribution

$$RF_3(R(\theta)) = \frac{1}{T_P} \sum_{i=0}^{G-1} [\sum_{l=1}^{N_R} r'(i, l|\theta)]^2 \tag{5.10}$$

4) RLD: Run length Distribution

$$RF_4(R(\theta)) = \frac{1}{T_P} \sum_{i=0}^{N_R} [\sum_{l=1}^{G-1} r'(i, l|\theta)]^2 \tag{5.11}$$

5) RP: Run Percentage

$$RF_5(R(\theta)) = \frac{1}{T_P} \sum_{i=0}^{G-1} \sum_{l=1}^{N_R} r'(i, l|\theta) \tag{5.12}$$

in which G is the number of grey levels, N_R is the number of run lengths in the matrix, and T_P is

$$T_P = \sum_{i=0}^{G-1} \sum_{l=1}^{N_R} r'(i, l|\theta). \tag{5.13}$$

In this experiment, the above-mentioned features of GLRLM are calculated.

5.2.3 Gray Level Co-occurrence Matrix Features

Spatial gray level co-occurrence estimates image properties related to second-order statistics, reflecting the relationship among pixels or groups of pixels (usually two) [104]. The GLCM is a 2D histogram that describes the occurrence of pairs of pixels that are separated by a certain distance, d. Let $I(x, y)$ be an image with size $N \times M$, and with G gray levels, and (x_1, y_1) and (x_2, y_2) be two pixels with gray level intensities i and j, respectively. When taking $\triangle x = x_2 - x_1$ in the x direction and

$\triangle y = y_2 - y_1$ in the y direction, the connecting straight line has a direction θ which is equal to $arctan\frac{\triangle y}{\triangle x}$. The normalized co-occurrence matrix $C_{\theta,d}$ is defined as:

$$C_{\theta,d} = (Num((x_1, y_1), (x_2, y_2)) \in (N \times M) \times (N \times M)|A)/K \tag{5.14}$$

Here A is a given condition, such as $\triangle x = d \sin\theta$,$\triangle y = d\cos\theta$,$I(x_1, y_1) = i$,and $I(x_2, y_2) = j$. Further on, Num represents the number of elements in the co-occurrence matrix and K is the total number of pairs of pixels [111, 112]. Normally, $d = 1, 2$ and $\theta =$ 0,45,90,and 135 degree are used for calculation. Eight different texture features are defined using co-occurrence matrix as follows [102]:

Entropy

$$-\sum_{i=0}^{G-1}\sum_{j=0}^{G-1} C_{ij} \log C_{ij} \tag{5.15}$$

Correlation

$$\sum_{i=0}^{G-1}\sum_{j=0}^{G-1} \frac{ijC_{ij} - \mu_x\mu_y}{\sigma_x\sigma_y} \tag{5.16}$$

Homogeneity

$$\sum_{i=0}^{G-1}\sum_{j=0}^{G-1} \frac{C_{ij}}{1 + |i - j|} \tag{5.17}$$

Absolute Value

$$\sum_{i=0}^{G-1}\sum_{j=0}^{G-1} |i - j|C_{ij} \tag{5.18}$$

Inertia (Contrast)

$$\sum_{i=0}^{G-1}\sum_{j=0}^{G-1} (i - j)^2 C_{ij} \tag{5.19}$$

Inverse Difference

$$\sum_{i=0}^{G-1}\sum_{j=0}^{G-1} \frac{C_{ij}}{1 + (i - j)^2} \tag{5.20}$$

Maximum Probability

$$max_{i,j}C_{ij} \tag{5.21}$$

Angular Second Moment (Energy)

$$\sum_{i=0}^{G-1}\sum_{j=0}^{G-1}(C_{ij})^2, \tag{5.22}$$

where C_{ij} is the element of co-occurrence matrix.

5.2.4 Histogram of Oriented Gradient Features

HOG features are feature descriptors frequently used for object-detection purposes in image processing and computer vision. The rationale behind these descriptors is that local object appearance and shape can be described by the distribution of intensity gradients or edge directions. The technique sums-up incidences of gradient orientation in localized portions of an image [17, 88]. HOG is computed on a dense grid of uniformly spaced cells, and uses overlapping local contrast normalization for higher accuracy [84,88]. It divides the image into small, connected regions called cells, and for each cell compiles a histogram of gradient directions or edge orientations for the pixels inside the cell. The combination of these histograms then constitutes the descriptor. For improved accuracy, the local histograms can be contrast-normalized by calculating a measure of the intensity across a larger region, called a block, and then using this value to normalize all cells within the block. This normalization offers lower sensitivity to changes in illumination or shadowing. Eighty HOG features are derived in this work.

5.2.5 Linear Binary Pattern Features

LBP operator [113] sweeps a window over the image and gives labels to central pixel of the window by thresholding its neighborhood with the central value and specifying binary numbers to the neighbors. Then it calculates the sum of the binary numbers multiplied by powers of two increasing clockwise or counterclockwise. The histogram of these 256 different labels is used as a texture descriptor. Considered neighborhood can be in different sizes. Any radius and any number of pixels in the neighborhood can be used. In the following, the notation (P, R) will be used for pixel neighborhoods, which means P sampling points on a circle of radius of R. The value of the LBP code of a pixel (x_c, y_c) is given by:

$$LBP_{P,R} = \sum_{p=0}^{P-1} S(g_p - g_c)2^p \tag{5.23}$$

$$S(x) = \begin{cases} 1 & x \geq 0 \\ 0 & otherwise \end{cases} \tag{5.24}$$

where g is the pixel intensity value. We have chosen $P = 8$ and $R = 1$ in our experiment.

5.2.6 Gabor Wavelet Transform

Gabor wavelets capture the local structure of the image correspond to spatial frequency (scales), spatial localization, and orientation selectivity. Therefore, they are extensively applied to texture analysis and image segmentation [98]. In the spatial domain, a two-dimensional Gabor filter is a Gaussian kernel function modulated by a complex sinusoidal plane wave, defined as:

$$G(x,y) = \frac{f^2}{\pi\gamma\eta}(-\frac{x'^2+\gamma^2y'^2}{2\sigma^2})exp(j2\pi fx'+\phi) \tag{5.25}$$

where x' and y' are defined as:

$$\begin{aligned} x' &= xcos\theta + ysin\theta \\ y' &= -xsin\theta + ycos\theta \end{aligned} \tag{5.26}$$

where f is the frequency of the sinusoid, θ is the orientation of the normal to the parallel stripes of a Gabor function, ϕ is the phase offset, σ is the standard deviation of the Gaussian envelope and γ is the spatial aspect ratio which specifies the ellipticity of the support of the Gabor function. Most typically, researchers use Gabor wavelets filters in five different scales and eight orientations [113–115]. In this work, the same convention as shown in Fig. 5.2 is followed.

5.3 Experimental Setup

5.3.1 Detection of Tumor Slices

The main idea in tumor slice detection is based on histogram asymmetry between the two brain hemispheres. Dividing the brain into two hemispheres is achieved by finding the longest diameter as the brain midline. In order to find histogram asymmetry, histograms of each hemisphere is calculated. Then, using mutual information [116], the slice likely to contain the tumor is determined. The advantage of this technique is its robustness against head rotation and tilt.

The algorithm includes six steps. First step separates the brain from the background. Second uses the center-mass algorithm to find the brains center. Third finds

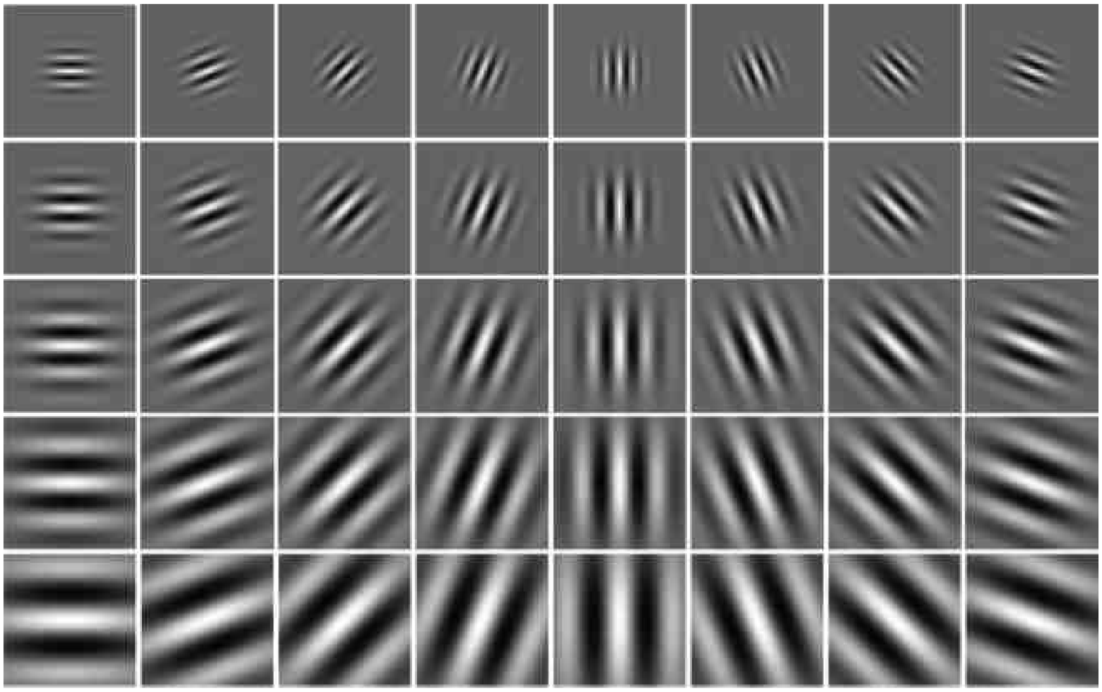

Figure 5.2: Gabor wavelet kernels in five scales and eight orientations

the brains borderline; cf. Fig. 5.3(b). Fourth finds the length of all possible brain diameters. Fifth step is finding the longest diameter as brain midline. The midline shown in Fig. 5.3(c) and Fig. 5.3(d). Sixth step finds the tumor slice based on mutual information between histograms of two brain hemispheres.

Using brain midline, the intensity histogram for each hemisphere is calculated. In both synthesized and real databases that are used, the number of slices is the same for all subjects. In this case, it can be assumed that the corresponding slices in different subjects present the same region of the brain, which have almost similar structures. This gives us the opportunity to create the standard histograms for healthy brain hemispheres for all slices using the training data; see Fig. 5.4(a). These standard histograms are compared with the histograms of the testing data in order to find the


(a) (b) (c) (d)

Figure 5.3: (a) Original Image, (b) Finding the brain borderline, (c) and (d) Example of resulted brain hemispheres

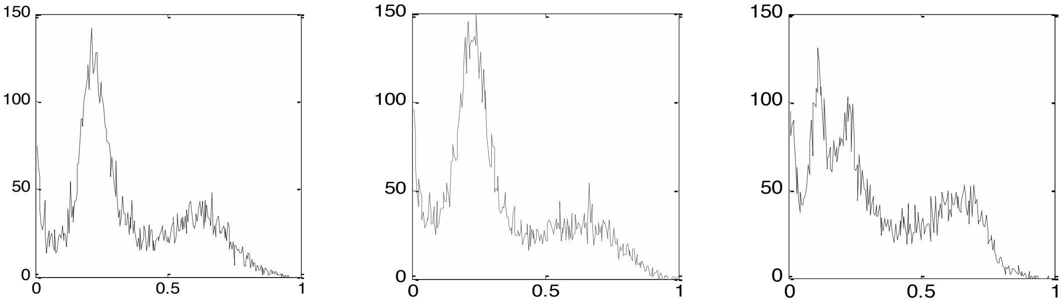

(a) (b) (c)

Figure 5.4: (a) Standard histogram of the healthy hemisphere, (b) Histogram of an example of healthy hemisphere, (C) Histogram of an example of tumor hemisphere

hemispheres containing tumor. Fig. 5.4(b) and Fig. 5.4(c) show sample histogram of healthy and tumor hemispheres. This method has the advantage of finding the exact tumor hemisphere, which facilitates the segmentation process searching only in the hemisphere of interest. If the number of slices is not consistent, another approach is to calculate the mutual information between histograms of the two hemispheres of a single brain image. In this case, the segmentation algorithm needs to search on the whole brain (not only one brain hemisphere).

The size of the tumors detectable by this method depends on the threshold for the amount of mutual information. Higher values make it easier to detect small tumors, but only at the cost of a certain percentage of false positives (healthy slices are detected to contain a tumor lesion). On the other hand, lower threshold prevents false positives, but the algorithm will not be able to detect small tumors. This is a trade-off problem as a degree of freedom for the designer depending on the application. In the experimental case, the threshold is chosen based on the observations made of the training data, tolerating the system's failure to detect very small and hardly visible tumors.

5.3.2 MRI Intensity Normalization

Due to the intra-scan and inter-scan image intensity variations, after detection of slices that include tumor, the MR image intensity [117] is normalized. Image intensity normalization is necessary in quantitative texture analysis of magnetic resonance imaging. There are six MRI intensity normalization methods: contrast stretch normalization, intensity scaling, histogram stretching, histogram normalization, Gaussian kernel normalization, and histogram equalization. Based on the result of [117], the histogram normalization method presents the best performance compared to the other normalization methods. Here histogram normalization method is applied prior to quantitative texture analysis, which is about stretching and shifting original image histogram in order to cover all the gray scale levels in the image. It is defined as:

$$f(x,y) = \frac{(GWM - BWM)}{(h_{max} - h_{min})}(h(x,y) - h_{min}) + BWM \tag{5.27}$$

where $h(x,y)$ is the original histogram of the initial image, $f(x,y)$ is new histogram, and h_{min} and h_{max} are smallest and largest gray scale level , respectively. GWM and BWM are new minimum and new maximum intensity levels.

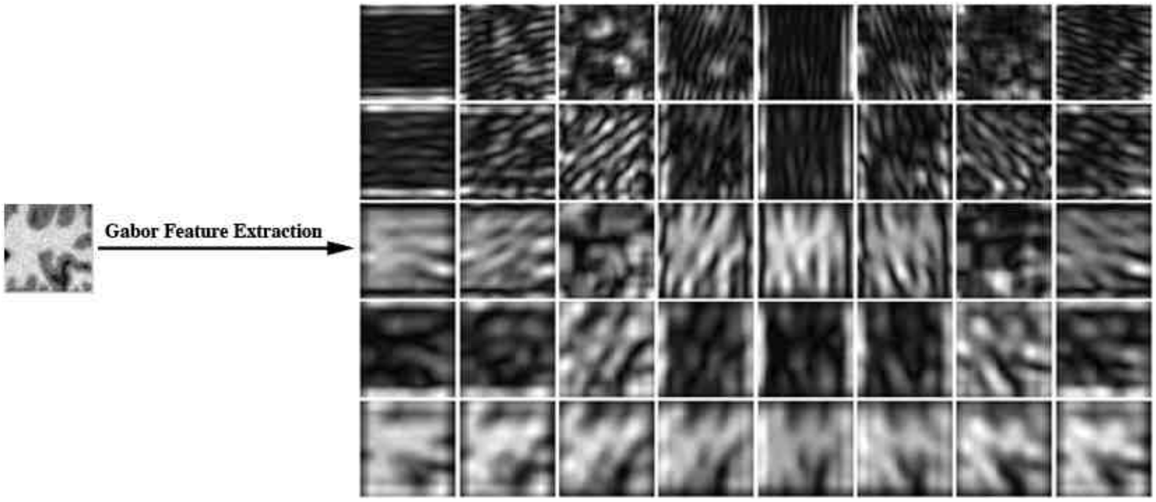

Figure 5.5: Real parts of the results of applying Gabor filters to the windowed brain image

5.3.3 Windowing

In order to create the training set, we automatically crop random windows from each selected hemisphere containing tumor. Having the brain midline and borderline helps us to restrict the windows to just cover the brain tissue and not the background. For the test step, a same size sliding window sweeps all over the brain, excluding the background area. Two sets of features are extracted using the aforementioned feature extraction methods.

5.3.4 Feature Aggregation

The Gabor wavelet features and statistical features are extracted using Gabor wavelet transform, first-order statistical descriptors, GLCM, GLRLM, HOG, and LBP methods, as described in Section 5.2.

Gabor wavelet features are extracted by applying Gabor wavelet kernels with five different scales and eight orientations on three different window sizes as 33 × 33,

45×45, and 65×65 windows. The length of Gabor feature vector is 43,560, 81,000, and 169,000, regarding to 33×33, 45×45 and 65×65 window sizes, respectively. Fig. 5.5 illustrates the real parts of the results of applying Gabor wavelet filters to a sample window in the brain MR image.

First-order statistical features include mean, median, average contrast, intensity energy and entropy, skewness and kurtosis. In our experiment, GLCM features are extracted by applying the angle $\theta = 0$, 45, 90 and 135 degrees. In each orientation, GLCM matrix and eight derived features are calculated.

GLRLM features are calculated for 0, 45, 90 and 135 degrees. Extracted features are SRE, LRE, GLD, RLD, and RP in four directions.

HOG features measure the occurrences of gradient orientations in the regional areas of the image. Using two scales and 8 orientations, eighty HOG feature values are extracted. Finally, the length of LBP features is 256. The total of seven first-order statistical features, 20 GLRLM features, 112 GLCM features, 80 HOG features, and 256 LBP features makes a 475-dimentional statistical feature vector. It is shown in Fig. 5.6.

5.3.5 Feature Dimensionality Reduction

For feature dimensionality reduction, we rely on principle component analysis (PCA). PCA is a mathematical tool that uses an orthogonal transformation to project a set of possibly correlated variables into a group of linearly uncorrelated ones that are called principle components [59]. The principal components attempt to maintain most of the variability of the data. We apply PCA to each set of extracted features, obtaining principal (feature) vectors from which we then select those with the highest

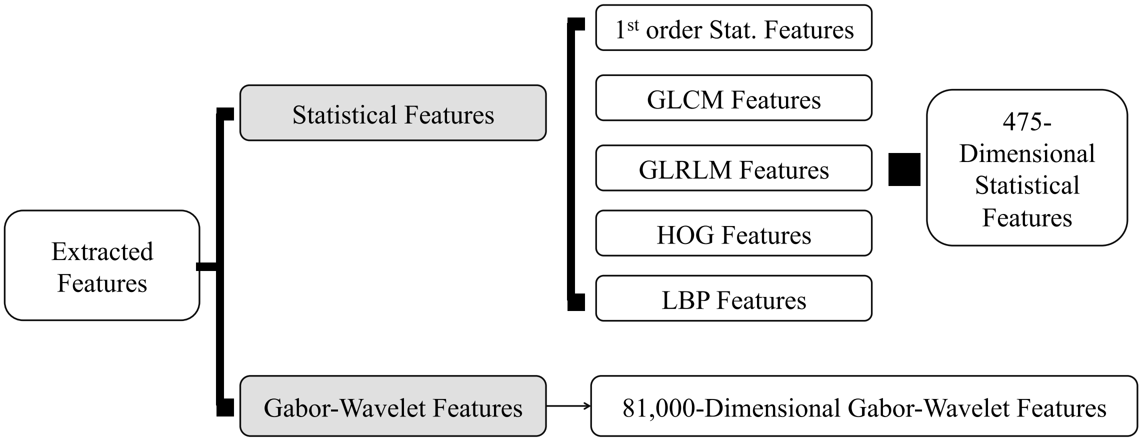

Figure 5.6: Diagram of two sets of extracted features

eigenvalues. Lets assume we have N nonzero eigenvectors as the output of the PCA. We select M eigenvectors corresponding to the highest eigenvalues. The optimal number of selected features (M) is obtained by calculating the reconstruction ratio, γ [60]. γ is defined as the ratio of the sum of the M selected eigenvalues to the sum of all eigenvalues, as:

$$\gamma = \sum_{i=1}^{M} \gamma_i / \sum_{i=1}^{N} \gamma_i \tag{5.28}$$

where γ_is are the eigenvalues sorted decreasingly. Here we chose to be 0.99. In all our cases, maximum of 20 features are satisfying the above constraint.

5.3.6 Feature Classifications

For classification, four supervised robust classification techniques are applied and the results are compared. These techniques are SVM, KNN, NSC, SRC [118] and one unsupervised clustering method, k-means.

The number of healthy windows is much higher than the number of tumor windows, which makes the training set imbalanced. To avoid the usual difficulties known to be caused by imbalanced training sets, we preferred to use the same number of healthy windows as that of tumor windows. Training samples are randomly selected. A 10-folded cross-validation is used to validate the robustness of our model. Cross validation helps also to prevent over-fitting.

After training the classifier, the recognition rate of the classifier on independent data (unseen during learning) is used as the indicator of our algorithm's performance in tumor lesion segmentation, and also each feature set's suitability for tumor lesion segmentation.

5.4 Experimental Results

5.4.1 Materials And Labeling of Training Examples

Brain tumor image data used in this work were obtained from the NCI-MICCAI 2013 Challenge on Multimodal Brain Tumor Segmentation [119] organized by K. Farahani, M. Reyes,B. Menze, E. Gerstner, J. Kirby and J. Kalpathy-Cramer . The challenge database contains fully anonymized images from the following institutions: ETH Zurich, University of Bern, University of Debrecen, and University of Utah and publicly available images from the Cancer Imaging Archive (TCIA). All in all, twenty-five real and simulated T1-w and flair MR images of the brain with high-grade glioma are applied in this study. Few examples of this data set - simulated and real T1-w, T2-w, and FLAIR - are depicted in Fig. 5.7, 5.8, 5.9, 5.10, 5.11, and 5.12, respectively.

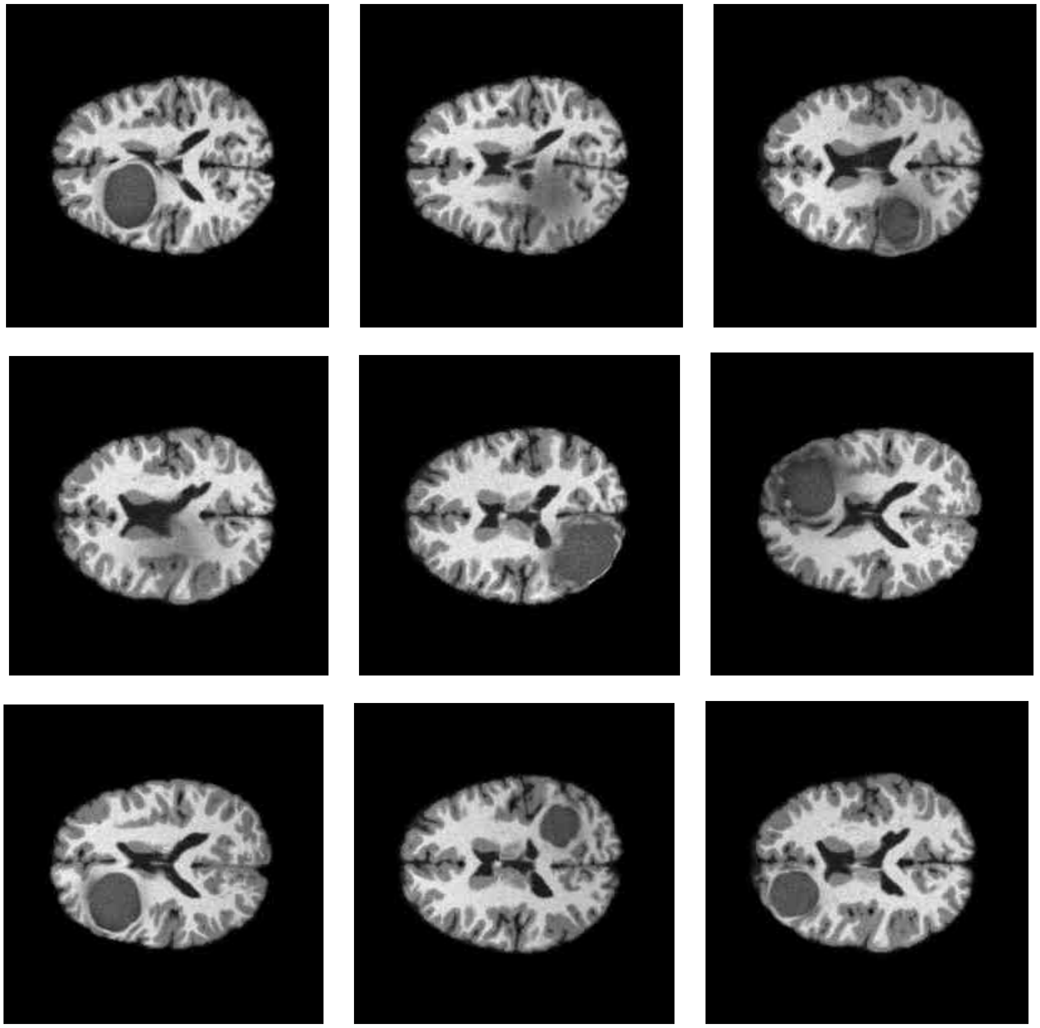

Figure 5.7: Examples of simulated T1-weighted brain MR images

Labeling: As indicated, each window was treated as a separate training example, described by a feature vector. We label the training examples as positive or negative. An example is labeled as positive if the tumor pixels cover more than half of the window. To be able to evaluate statistical significance of our results, all experiments are conducted using the 10-folded cross-validation technique, which makes it possible to use t-test.

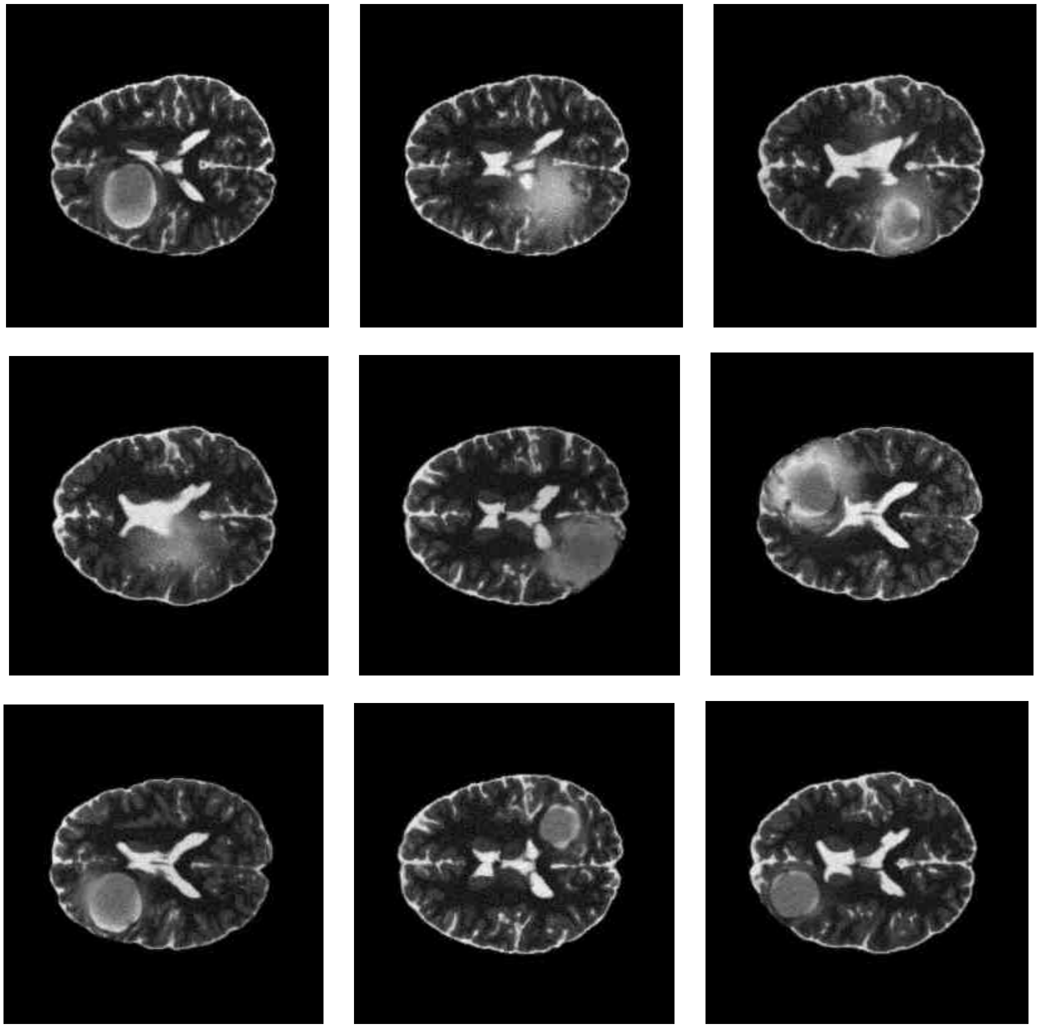

Figure 5.8: Examples of simulated T2-weighted brain MR images

5.4.2 Establishing Optimum Conditions

Before proceeding to the work, we need to answer two questions regarding the conditions used in the experiments. What is the impact of noise-reduction on texture-based feature extraction? What is the optimum size of the window?

Regarding the first question, noise in the original image is reduced by Gaussian filters. Keeping all other conditions the same, statistical feature vectors are extracted

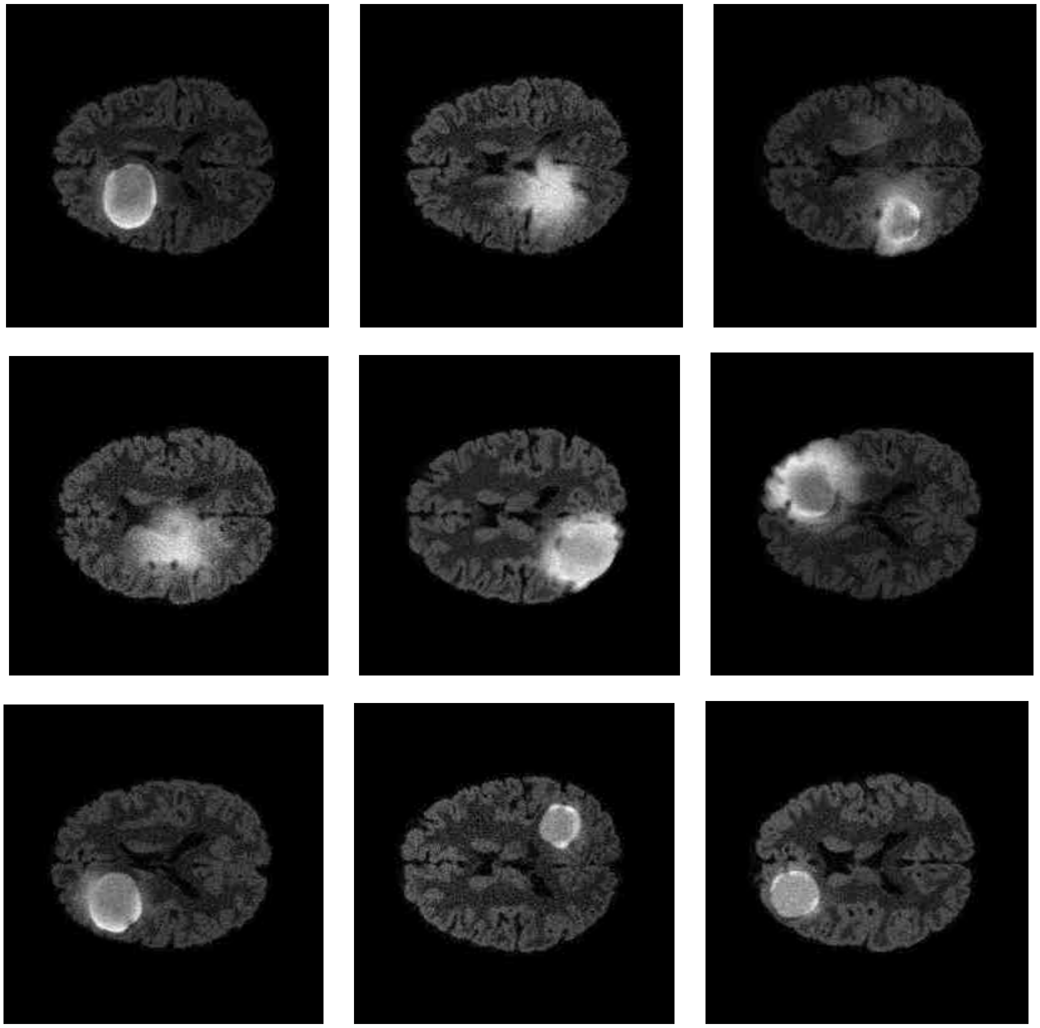

Figure 5.9: Examples of simulated FLAIR MR images

with noise reduction, and then without noise reduction. The experiments summarized in Fig. 5.13 show that noise-reduction actually impaired classification accuracy when we apply texture-based features. Therefore, we decided to avoid noise reduction.

Regarding the second question, different window-sizes are tried. The statistical feature vectors obtained from three different window-sizes (33×33, 45×45, and 65×65) are classified by several classification methods. As shown in Fig. 5.14, the

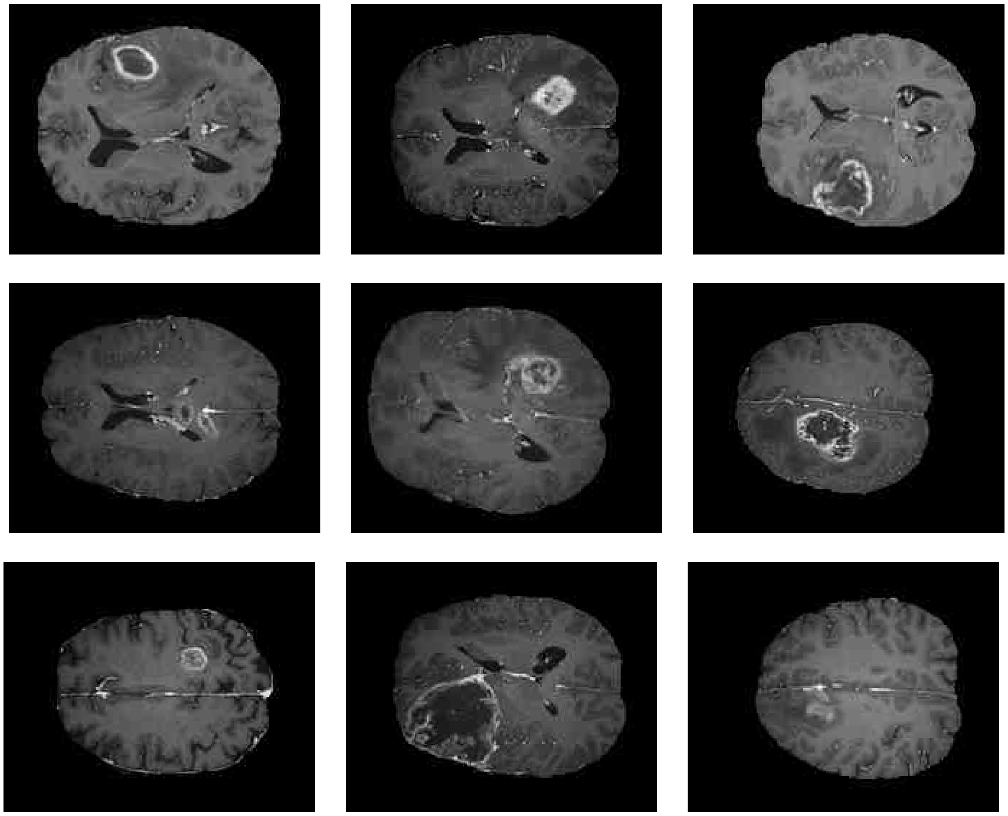

Figure 5.10: Examples of real T1c-weighted MR images

window size 45 × 45 yieldes the highest accuracy. Based on this experience, we decide to use the 45 × 45 window size in the rest of the study.

5.4.3 Tumor Segmentation Result

After a slice is recognized to have tumor, we apply the segmentation to localize the tumor area. We attain the candidate tumor regions using a sliding window that sweeps the whole brain tissues. Gabor wavelet and statistical feature sets are extracted from each instance of the window. After applying PCA for dimensionality reduction on each feature set, they are classified applying different classification approaches. Fig.5.15(a) shows the results of SVM with linear and RBF kernels for Gabor wavelet

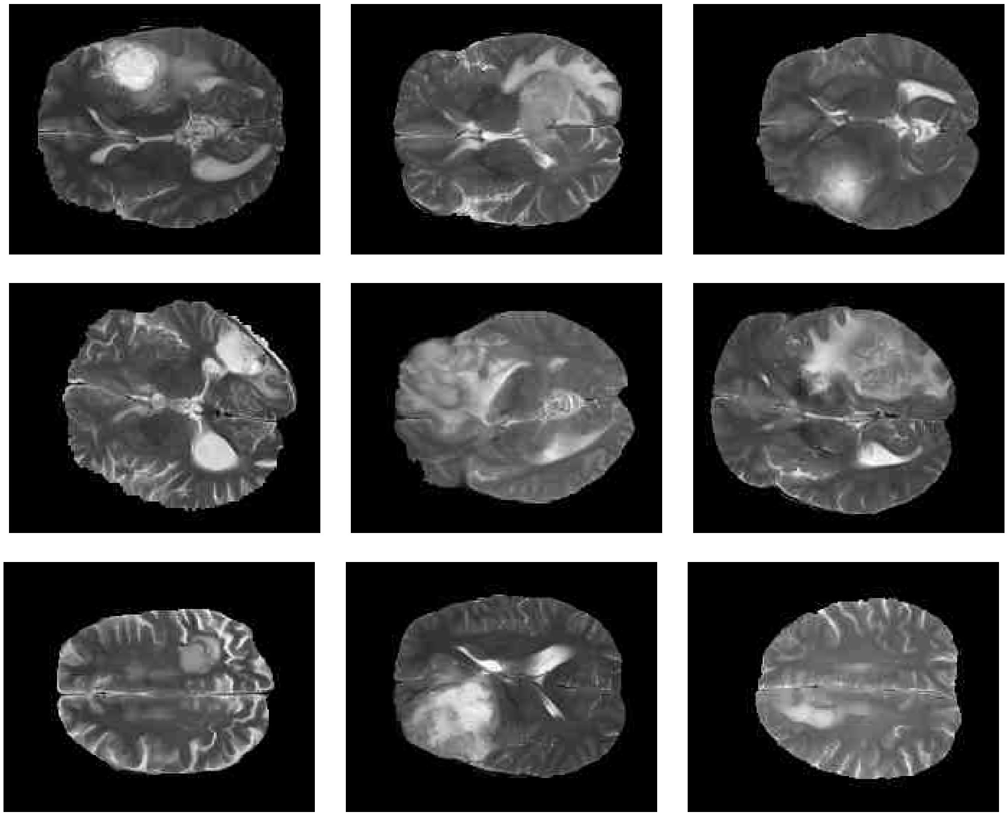

Figure 5.11: Examples of real T2-weighted MR images

and statistical features extracted from T1-w images of simulated data. The horizontal axis represents the number of features used for classification purposes, and the vertical axis shows the classification accuracy. We can see that, with only 10 first features of the PCA output the accuracy of the classifiers becomes stable. Increasing the feature vector length over 10 does not influence the accuracy rates significantly. Using 10 features, classification accuracy of SVM with linear kernel and RBF kernel are $95.1 \pm 0.2\%$ and $95.7 \pm 0.3\%$ for statistical features, and $92.2 \pm 0.5\%$, and $94.3 \pm 0.4\%$ for Gabor features, respectively.

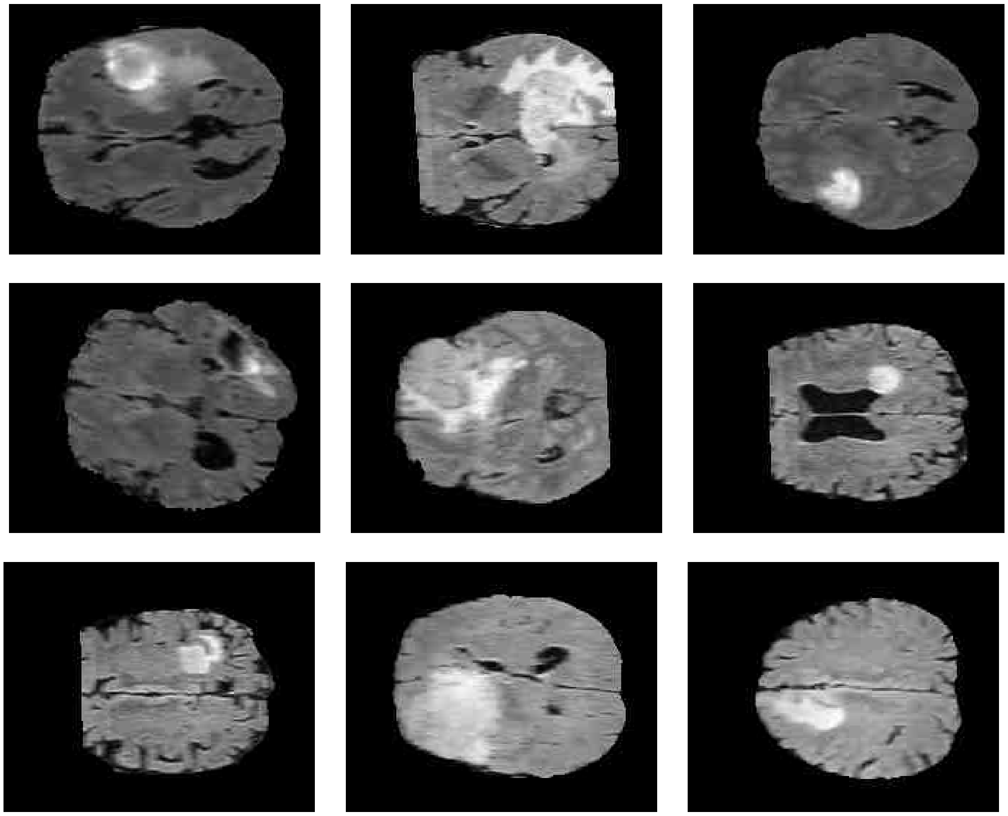

Figure 5.12: Examples of real FLAIR MR images

Classification result of kNN classifier is shown in Fig. 5.15(b). With only 10 first features of the PCA output the accuracy of the classifiers becomes stable. Using 10 features, classification accuracy of kNN with k=1 and k=7 are 89.6 ± 0.3% and 92.5 ± 0.7% for statistical features, and 87.5 ± 0.7%, and 90.7 ± 0.8% for Gabor features, respectively. Again, increasing the feature vector length over 10 does not influence the accuracy rates significantly.

Fig.5.15(c) shows the results of NSC with Gaussian and general under-sampling for Gabor wavelet and statistical features. The NSC is a technique known to be very sensitive to noise and the result is polluted with distortions. Using 15 features,

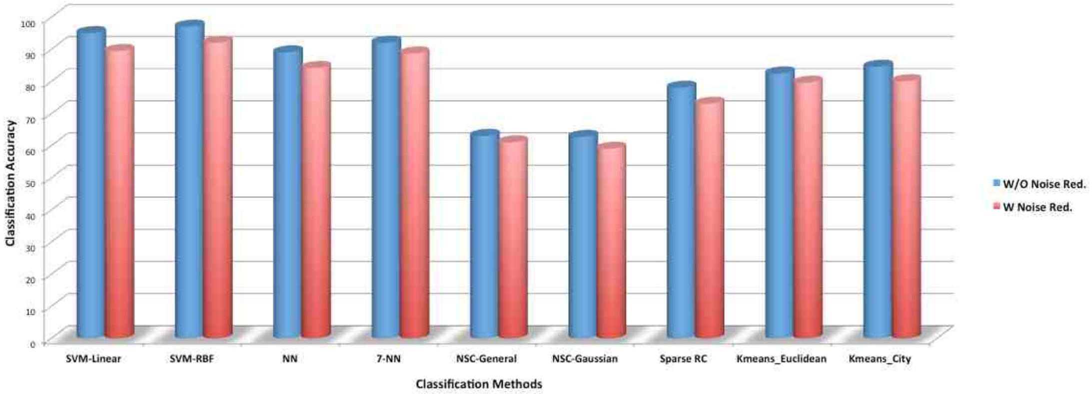

Figure 5.13: Comparison of accuracy of different classification methods using statistical features with and without noise reduction

classification accuracy of NSC-Gaussian and NSC-general are 63.5 ± 1.3%, 63.8 ± 0.8% for statistical features, and 61.8 ± 1.6%, and 64.5 ± 1.1% for Gabor features, correspondingly. In our experiments, general case outperforms the Gaussian.

Additionally, the accuracy of sparse representation classifier gets stable with applying only 12 first features of the PCA output and offers 78.1 ± 0.4% recognition rates for statistical features and 71.1 ± 0.2% for Gabor feature, as it is depicted in Fig. 5.15(d).

Next, unsupervised k-means clustering divides the feature vectors into two groups of normal and tumors. Labels achieved from k-means clustering for test group are then compared with the real labels, and the accuracy is calculated. Classification accuracy of k-means using Euclidean and city-block distances are 83.2 ± 0.1% and 85.4±0.2% for statistical features, and 69.6±0.3% and 71.3±0.2% for Gabor features, respectively.

Based on these results, statistical features and SVM with RBF kernel are used in order to segment the brain tumors. After feature extraction from each instance of

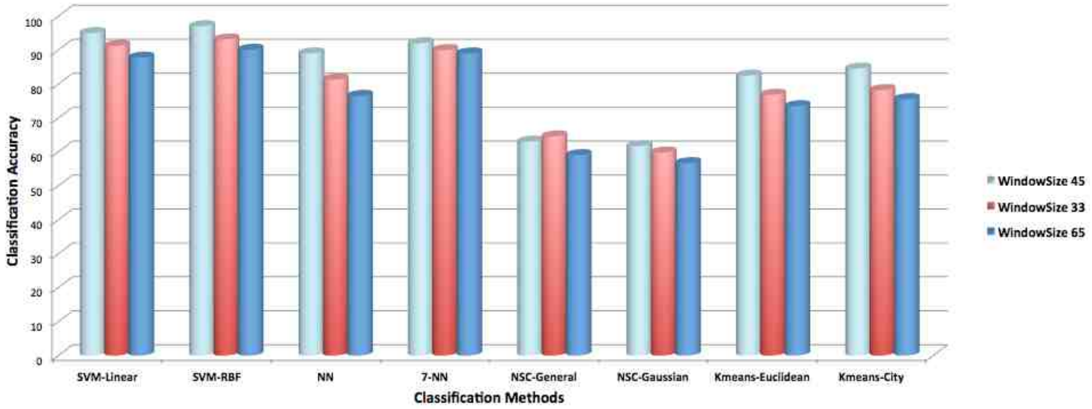

Figure 5.14: Comparison of accuracy of different classification methods for 3 different window sizes as 45, 33, and 65

the window, if the window is classified to have tumor, the central pixel of the window will be labeled as tumor. On the other hand, if it is classified as healthy, the central pixel will be labeled as healthy. Fig. 5.16 (second column) shows the result of this labeling on three sample brain slices using . As it can be seen, there are some parts of the tumor that is mistakenly labeled as healthy or some parts of the healthy tissue labeled as tumor by mistake. In order to remove these false positives/negatives, a consistency verification algorithm is applied.

A consistency verification (CV) algorithm is used to remove the false positives and false negatives. That is, we use a majority filter to alter the pixel labels that are not consistent with their neighbor labels in a certain neighborhood. For instance, if the center pixel of a window is labeled as tumor while the majority of the surrounding pixels are labeled as healthy, the center pixels label is simply switched to healthy. On the other hand, if a pixel inside the tumor area is mistakenly labeled as healthy, since the majority of the surrounding labels are tumor, it will switch to tumor. Here, consistency verification is applied in a 3×3 neighborhood window. The results of

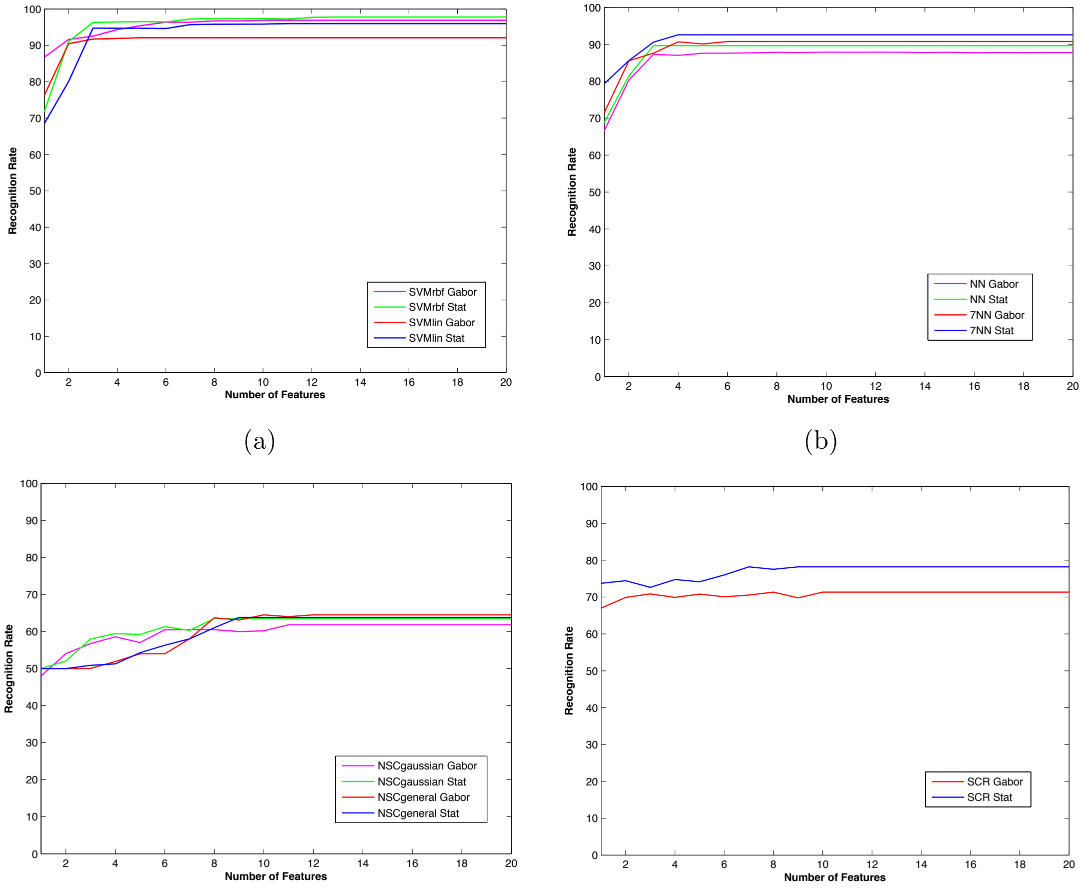

(a) (b)

(c) (d)

Figure 5.15: (a) Classification accuracy of SVM (linear and RBF kernel) for Gabor wavelet and statistical features for different numbers of features, (b) Classification accuracy of kNN (k=1 and k=7) for Gabor wavelet and statistical features for different numbers of features, (c) Classification accuracy of NSC (Gaussian and general) for Gabor wavelet and statistical features for different numbers of features, (d) Classification accuracy of sparse representation classifier for Gabor wavelet and statistical features for different numbers of feature

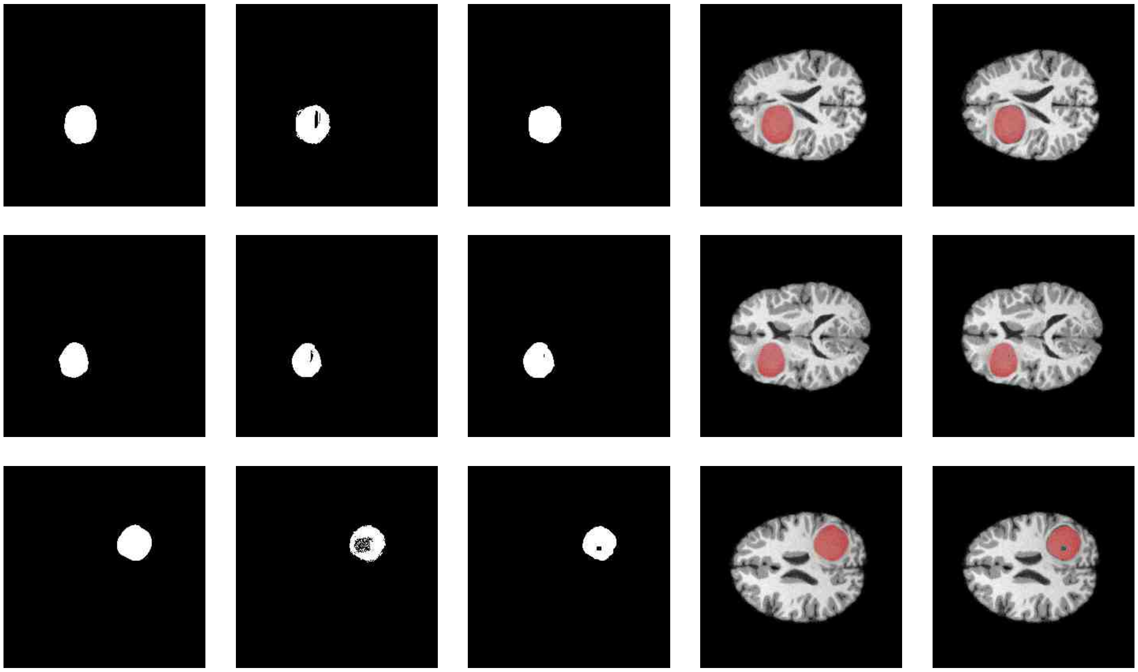

Figure 5.16: Examples of tumor lesion segmentation on T1-weighted simulated data. (first column) Golden label, (second column) segmented lesion before consistency verification, (third column) segmented lesion after consistency verification, (forth column) overlay of Golden label on the brain image, (fifth column) overlay of our segmented area on the brain image.

applying consistency verification algorithm are depicted in part (c) of Fig. 5.16. Similar results for tumor segmentation on FLAIR and T2-w MR images are depicted in Fig. 5.18.

We notice that in most cases, by increasing the number of neighbors considered in kNN algorithm the accuracy rates tend to increase which is compatible with theoretical expectation. In addition, support vector machines provide better classification accuracy rates compared to kNN, NSC, and SRC. Moreover, support vector machines with radial basis functions achieve highest estimation accuracy compared to linear and quadratic kernel functions.

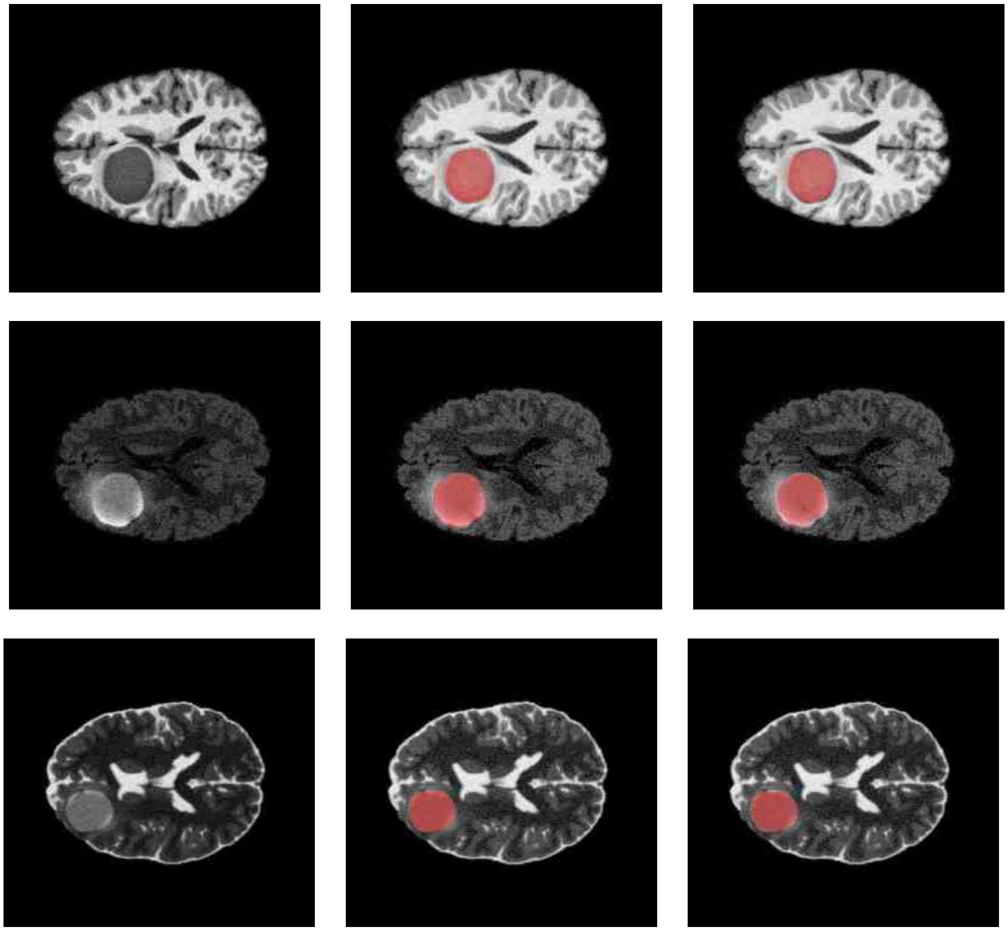

(g) (h) (i)

Figure 5.17: Examples of tumor lesion segmentation on T1-w (first row), FLAIR (second row) and T2-w (third row) simulated data. (a) original data, (b) golden label, (c) segmented lesion after consistency verification

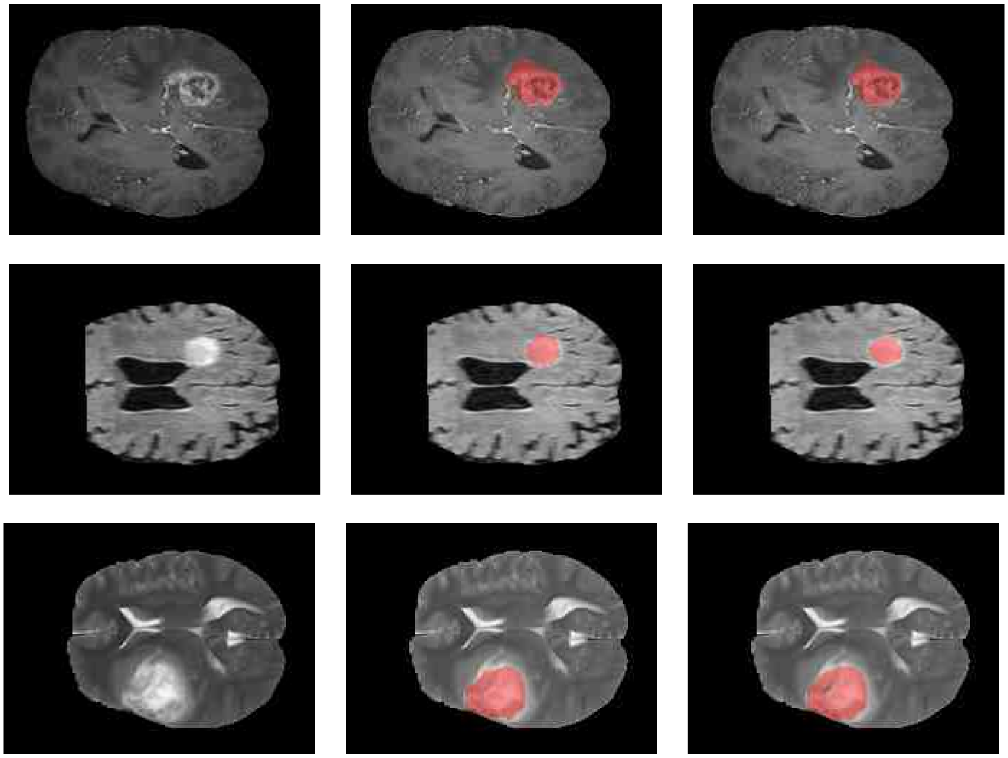

(g) (h) (i)

Figure 5.18: Examples of tumor lesion segmentation on T1-w (first row), FLAIR (second row) and T2-w (third row) real data. (a) original data, (b) golden label, (c) segmented lesion after consistency verification

Table 5.1: Comparing Stat method with other methods

Algorithm / Dep. on	[120]	[121]	[20]	[122]	[123]	[124]	[55]	[125]	[126]	SFSW
Bias correction	-	-	-	√	√	-	√	-	-	-
Registration	-	√	√	√	√	√	√	-	-	-
Multi-spectral MRI	-	√	√	√	√	-	√	-	-	-
Initial assumptions	-	-	-	√	-	-	-	-	-	-
High quality data	-	√	√	-	-	-	-	-	√	-
Manual intervention	√	-	-	-	-	-	-	-	-	-
over-segmentation	√	-	-	-	-	-	-	√	-	-
High computational complexity	-	-	-	-	√	√	√	√	√	√

5.5 Comparing Statistical Features and Gabor Features

While many techniques for feature extraction have been published, we are not aware of any convincing comparative study in the field of tumor segmentation. We evaluate the proficiency and ability of two widely used feature sets –Gabor wavelets and statistical features– in tumor segmentation domain. These two feature sets possess different abilities to give rise to accurate MRI lesion segmentation. We quantify the ability using three commonly used performance criteria: sensitivity, specificity, and accuracy that are described in Section 4.1.

Table 5.2 summarizes the classification accuracies achieved by different classifiers on simulated T1-w images described by the two different feature sets: Gabor wavelets, and statistical features. Table 5.3 and 5.4 shows the classification accuracies of the same classifiers on FLAIR and T2-weighted sequences of simulated dataset explained by two feature sets as Gabor wavelets and statistical features. Generally FLAIR images provide us with higher segmentation accuracy because they have minimal sensitivity to CSF. Therefore, the partial volume effects that cause misclassifications in T1-w images do not cause the same problem in FLAIR images. Similarly, Table 5.5 and Table 5.6 and Table 5.7 show the result of classifiers on real dataset for T1c-w, FLAIR, and T2-w images, respectively. It is clearly seen that in most of the cases statistical features provide higher accuracy than Gabor wavelets features.

Table 5.2: Classification accuracies achieved on the two different feature sets obtained from simulated T1-w images. The bolded values denote cases in which the given features set yields significantly better results than the other set (T-test with significance level of 5%).

	SVM Linear	SVM RBF	kNN K=1	kNN K=7	NSC General	NSC Gaussian	k-means Euclidean	k-means City-block	Sparse Representation
Gabor Wavelet Features	92.2 ±0.5	94.3 ±0.4	87.5 ±0.7	90.7 ±0.8	**64.5** **±1.1**	61.8 ±1.6	69.6 ±0.3	71.3 ±0.2	71.1 ±0.2
Statistical Features	**95.1** **±0.2**	**95.7** **±0.3**	**89.6** **±0.3**	**92.5** **±0.7**	63.8 ±0.8	**63.5** **±1.3**	**83.2** **±0.1**	**85.4** **±0.2**	**78.1** **±0.4**

Table 5.3: Classification accuracies achieved on the two different feature sets obtained from simulated FLAIR images. The bolded values denote cases in which the given features set yields significantly better results than the other set (T-test with significance level of 5%).

	SVM Linear	SVM RBF	kNN K=1	kNN K=7	NSC General	NSC Gaussian	k-means Euclidean	k-means City-block	Sparse Representation
Gabor Wavelet Features	95.0 ±0.2	95.6 ±0.2	93.5 ±0.3	**95.7** **±0.5**	65.1 ±1.2	64.4 ±1.7	79.3 ±0.3	82.4 ±0.2	74.8 ±0.7
Statistical Features	**95.3** **±0.3**	**95.9** **±0.4**	**94.3** **±0.1**	94.5 ±0.4	**66.8** **±1.3**	**65.2** **±0.9**	**91.4** **±0.8**	**92.9** **±0.4**	**79.1** **±0.6**

Table 5.4: Classification accuracies achieved on the two different feature sets obtained from simulated T2-w images. The bolded values denote cases in which the given features set yields significantly better results than the other set (T-test with significance level of 5%).

	SVM Linear	SVM RBF	kNN K=1	kNN K=7	NSC General	NSC Gaussian	k-means Euclidean	k-means City-block	Sparse Representation
Gabor Wavelet Features	93.1 ±0.3	**93.6** **±0.1**	89.3 ±0.2	89.7 ±0.5	62.5 ±0.8	61.3 ±1.3	74.9 ±0.4	79.7 ±0.3	70.8 ±0.4
Statistical Features	**94.8** **±0.1**	93.2 ±0.5	**91.2** **±0.4**	**92.4** **±0.3**	**64.1** **±1.2**	**63.8** **±0.9**	**79.8** **±0.2**	**86.4** **±0.5**	**76.6** **±0.6**

Table 5.5: Classification accuracies achieved on the two different feature sets obtained from real T1c-w images. The bolded values denote cases in which the given features set yields significantly better results than the other set (T-test with significance level of 5%).

	SVM Linear	SVM RBF	kNN K=1	kNN K=7	NSC General	NSC Gaussian	k-means Euclidean	k-means City-block	Sparse Representation
Gabor Wavelet Features	90.1 ±0.5	90.0 ±0.4	79.7 ±0.8	80.5 ±0.9	57.9 ±1.9	58.3 ±1.5	**71.7** **±0.1**	72.6 ±0.5	**68.2** **±0.2**
Statistical Features	**90.9** **±0.3**	**92.3** **±0.1**	**88.1** **±0.6**	**89.7** **±0.7**	**61.6** **±1.5**	**60.5** **±1.6**	71.2 ±0.4	**73.1** **±0.1**	65.5 ±0.7

Of course, the picture provided by classification accuracy can be somewhat one-sided. For better insight, therefore, Tables 5.8 to5.12 present values of three performance criteria –sensitivity, specificity and accuracy– for T1-w images of simulated dataset. It can be see that statistical features lead to significantly better results for all three criteria in the case of SVM with linear and RBF kernels, kNN (k=1), SRC, NSC with Gaussian under-sampling, and k-means clustering. In NSC with general under-sampling case, Gabor wavelets features lead to better results along all three ones. For kNN (k=7), the majority of better performances are still with statistical features. Similar experiments on FLAIR sequences of simulated data, as well as, T1-w and FLAIR images of real data are applied and similar results are achieved.

Table 5.6: Classification accuracies achieved on the two different feature sets obtained from real FLAIR images. The bolded values denote cases in which the given features set yields significantly better results than the other set (T-test with significance level of 5%).

	SVM Linear	SVM RBF	kNN K=1	kNN K=7	NSC General	NSC Gaussian	k-means Euclidean	k-means City-block	Sparse Representation
Gabor Wavelet Features	86.6 ±0.3	92.2 ±0.1	82.6 ±0.5	83.8 ±0.1	**61.5** **±1.2**	59.6 ±1.7	71.5 ±0.6	70.1 ±0.2	70.3 ±0.4
Statistical Features	**91.3** **±0.2**	**93.2** **±0.3**	**86.5** **±0.3**	**88.4** **±0.4**	60.9 ±1.6	**61.3** **±1.4**	**77.2** **±0.2**	**80.7** **±0.8**	**73.9** **±0.5**

Table 5.7: Classification accuracies achieved on the two different feature sets obtained from real T2-w images. The bolded values denote cases in which the given features set yields significantly better results than the other set (T-test with significance level of 5%).

	SVM Linear	SVM RBF	kNN K=1	kNN K=7	NSC General	NSC Gaussian	k-means Euclidean	k-means City-block	Sparse Representation
Gabor Wavelet Features	88.3 ±0.1	**92.9** **±0.3**	81.6 ±0.2	83.7 ±0.1	**64.4** **±0.9**	62.9 ±1.3	76.3 ±0.3	75.2 ±0.5	71.9 ±0.4
Statistical Features	**91.7** **±0.4**	92.4 ±0.2	**85.3** **±0.4**	**88.4** **±0.5**	63.8 ±1.7	**63.5** **±1.1**	**79.8** **±0.5**	**80.5** **±0.6**	**74.1** **±0.8**

Although Gabor wavelets are employed widely in computer vision and medical image processing, they occupy large amount of memory, and their high redundancy makes the computation heavy and slow. To get a better idea about these costs, we measured the run-times needed for the individual steps. The results summarized in Table 5.13 were measured on an Intel Xeon CPU X5472 machine at 3 GHz and with 64 GB of RAM. We should remember that this concerns T1-w images of 25 subjects, which each subject has 181 slices. Table 5.14 shows the average run time for a single slice. They indicates that statistical features in comparison with Gabor wavelet features have the potential to be highly valuable in tumor segmentation methods.

Table 5.8: Results of SVM Classifier for T1-w images of simulated dataset. The bolded values denote cases when the given features set yield significantly better results that the two other sets (T-test with significance level of 5%).

	SVM with Linear kernel			SVM with RBF kernel		
	Sensitivity	Specificity	Accuracy	Sensitivity	Specificity	Accuracy
Gabor-wavelet Features	90.6 ±0.4	91.8 ±0.9	92.2 ±0.5	95.4 ±1.3	93.9 ±0.2	94.3 ±0.4
Statistical Features	**96.3 ±0.7**	**94.8 ±0.3**	**95.1 ±0.2**	**96.2 ±0.9**	**95.7 ±0.1**	**95.7 ±0.3**

Table 5.9: Results of kNN classifier for T1-w images of simulated dataset. The bolded values denote cases when the given features set yield significantly better results that the two other sets (T-test with significance level of 5%).

	kNN (K=1)			kNN (K=7)		
	Sensitivity	Specificity	Accuracy	Sensitivity	Specificity	Accuracy
Gabor-wavelet Features	86.7 ±0.9	88.1 ±0.7	87.5 ±0.7	89.2 ±0.8	91.3 ±0.6	90.7 ±0.8
Statistical Features	**89.8 ±1.1**	**90.3 ±0.4**	**89.6 ±0.3**	**92.7 ±0.9**	**91.1 ±0.5**	**92.5 ±0.7**

5.6 Conclusion

In this chapter, a texture-based approach for tumor detection and segmentation using single-spectral MR images is presented. An integrated automated framework that is able to detect the MR images containing tumor lesion and then segment the tumor lesion is implemented on T1-weighted, T2-weighted, and FLAIR sequences. The remarkable accuracy of the proposed algorithm in tumor segmentation ($95.9 \pm 0.4\%$ for FLAIR images of simulated data, and $93.2 \pm 0.3\%$ for FLAIR images of real data) demonstrates the efficiency of this method. The proposed method detects the slices containing tumor using mutual information of histograms of two brain hemispheres. This allows it to recognize the brain hemisphere containing tumor,

Table 5.10: Results of NSC classifier for T1-w images of simulated dataset. The bolded values denote cases when the given features set yield significantly better results that the two other sets (T-test with significance level of 5%).

	NSC in Gaussian case			NSC in General case		
	Sensitivity	Specificity	Accuracy	Sensitivity	Specificity	Accuracy
Gabor-wavelet Features	60.1 ±1.3	61.3 ±0.7	61.8 ±1.6	**66.4** **±1.7**	**63.1** **±1.0**	**64.5** **±1.1**
Statistical Features	**62.9** **±1.4**	**64.8** **±0.3**	**63.5** **±1.3**	62.5 ±1.2	62.7 ±0.9	63.8 ±0.8

Table 5.11: Results of k-means classifier for T1-w images of simulated dataset. The bolded values denote cases when the given features set yield significantly better results that the two other sets (T-test with significance level of 5%).

	K-means with Euclidean distance			K-means with City block distance		
	Sensitivity	Specificity	Accuracy	Sensitivity	Specificity	Accuracy
Gabor-wavelet Features	67.7 ±1.2	71.1 ±0.9	69.6 ±0.3	70.3 ±1.5	72.1 ±0.6	71.3 ±0.2
Statistical Features	**84.2** **±1.1**	**80.3** **±0.6**	**83.2** **±0.1**	**85.2** **±1.6**	**83.3** **±0.5**	**85.4** **±0.2**

which decreases the computational process from analyzing the whole brain to just one hemisphere. In addition, it is independent of atlas registration, prior anatomical knowledge, or bias corrections that restrict the general application of many state-of-the-art methods. Note that, any inaccuracy in registration or bias correction stages will directly affect the precision of the lesion segmentation. The other benefit of the proposed method is in the use of single-spectral MRI. While using multi-spectral MR images address the intensity similarities between lesion and healthy tissues, in some of practical clinical situations only one type of anatomical MR image is collected due to time, cost, and patient situation limitations. In addition, use of multi-spectral data implies the need to ensure that each of the spectra must be properly registered.

Table 5.12: Results of SRC classifier for T1-w images of simulated dataset. The bolded values denote cases when the given features set yield significantly better results that the two other sets (T-test with significance level of 5%).

	Sparse Representation Classifier		
	Sensitivity	Specificity	Accuracy
Gabor-wavelet Features	69.5 ±1.9	74.2 ±0.8	71.1 ±0.2
Statistical Features	**74.0 ±1.6**	**80.9 ±1.3**	**78.1 ±0.4**

Table 5.13: Average run time for each step of the algorithm for 25 subjects

Algorithm Step	Processing Time
Tumor slice detection	12 minutes
Gabor-wavelet feature extraction	14 minutes
Statistical feature extraction	15 minutes
PCA on Gabor-wavelet feature	52 minutes
PCA on statistical feature	6 minutes

Additionally, despite the need of some other methods to have the initial assumptions, such as a given number of tissue classes or a multi-scale classification, this algorithm does not require any such information. This makes the proposed algorithm much more robust and more general than other methods.

As an additional study, the capability and efficacy of two different feature sets, Gabor wavelets and statistical features, in automated segmentation of brain tumor lesions in MRI images are compared. Applying gray level co-occurrence matrix, grey level run length matrix, histogram of oriented gradient, and linear binary pattern method, second-order statistical feature vectors are derived. Adding first-order statistical features to this group, a 475-dimensional statistical feature vector is obtained. On the other hand, employing the Gabor wavelet transform, in five scale and eight

Table 5.14: Average run time for each step of the algorithm for 1 slice

Algorithm Step	Processing Time
Tumor slice detection	720 ms
Gabor-wavelet feature extraction	840 ms
Statistical feature extraction	900 ms
PCA on Gabor-wavelet feature	3,120 ms
PCA on statistical feature	360 ms

orientations, an 81000-dimensional Gabor wavelet feature vector is captured. The comparison results indicate that statistical features usually offer higher accuracy than Gabor wavelet features. Moreover, statistical features have much smaller dimensionality than Gabor wavelet-based feature (475 vs. 81000). Although Gabor wavelets are employed widely in computer vision and medical image processing due to their effective directional selectivity, they occupy large amount of memory; they are highly redundant and lead to high computational costs. Even in the laboratory conditions, although the feature extraction time for both Gabor wavelet and statistical features are almost the same, the dimensionality reduction using PCA is almost eight times faster for statistical features. These observations seem to prove that statistical features are adequately enough to discriminate tumor tissues from other tissue types in T1-weighted, T2-weighted, and FLAIR images.

CHAPTER 6

A Winnow-Based Feature Selection and Contour-Based Segmentation of Brain Tumor Lesions

6.1 Motivation

Using the proposed algorithm in the previous chapter, the maximum obtained accuracy for tumor segmentation was $95.9 \pm 0.4\%$ for simulated data and $93.2 \pm 0.3\%$ for real data. In order to reduce the computational complexity and expedite the segmentation algorithm, and also to improve the system performance, some modifications are applied in the algorithm presented in previous chapter. The algorithm modifications are applied in three main phases: feature extraction, feature selection, and tumor localization.

First, the feature pool size is increased with adding other useful texture-based feature extraction techniques such as anisotropic Morlet complex wavelet transform, dual-tree complex wavelet transform, and wavelet packet decomposition. It is worth mentioning that for the first time, in this study anisotropic Morlet complex wavelet transform and dual-tree complex wavelet transform are applied in tumor segmentation study.

Adding these texture-based features to extracted statistical features from previous chapter, construct a very long feature vector. One of the efficient ways of reduction of dimensionality of data in mining the large feature sets without sacrificing class discrimination is feature selection. There are many potential benefits of feature selection like facilitating data visualization and data understanding, reducing the calculation and storage requirements, reducing training and utilization times, and defying the curse of dimensionality to improve classification performance [127]. Moreover, feature selection methods are usually fast and more efficient than feature dimensionality reduction approaches. In this section, a novel feature selection approach based on regularized Winnow algorithm (RWA) is proposed. RWA is originally a classifier, however, the low complexity of this method motivates to employ it in feature selection. While RWA classifier works with binary feature vectors, it is modified to not only work as a feature selection technique but also to be able to handle non-binary features. The presented feature selection method is fast and efficient in dealing with many irrelevant attributes.

For localizing the tumor area, a sliding window sweeps through the whole brain tissue, excluding background area, to localize candidate tumor regions. In order to decrease the calculation time, the window sweeps with the step size of five pixels. In this application, it decreases the calculation complexity by 25 times. A tumor classification approach is then applied on every instance of the window. If the window is classified to have tumor, the central pixel of the window will be labeled as tumor. On the other hand, if it is classified as healthy, the central pixel will be labeled as healthy. Then, the obtained candidate pixels determined by this method to be as tumor is used to construct the initial points for skippy greedy snake algorithm.

Skippy greedy snake algorithm is an active contour model, which performs the search in an alternate skipping way between the even and odd nodes of a snake with different step sizes. The alternative step sizes are adjusted so that the snake is less likely to be trapped at a pseudo-local minimum. The iteration process is based on a coarse-to-fine approach to improve the convergence. Specifying the proper initial points has a great influence on the accuracy and convergence speed of the skippy greedy snakes algorithm. In addition, it satisfies the requirement of human interference to manually specify initial points. Using this method, more accurate results besides less computational complexity for brain tumor segmentation are achieved.

6.2 Texture-Based Feature Extraction Method

6.2.1 Anisotropic Morlet Complex Wavelet Transform

Wavelet transform is a powerful tool in signal and image processing because of its capability in presenting aspects of data which other signal analysis techniques overlook like trends, breakdown points, discontinuities in higher derivatives, and self-similarity [38]. In mathematical point of view, a wavelet transform is an integral transform, in which the kernel is a function (wavelet) that has dense support, indicating that the function is non-zero over a finite interval and zero elsewhere [1]. This feature makes wavelet analysis an efficient tool in compression and de-noising the signal without considerable degradation, and also in identification of local characteristics of a random field.

One of the important wavelets is Morlet wavelet, which has numerous applications in signal and image processing fields. The Morlet wavelet has a form very similar to the Gabor transform. The important difference is that the window function also needs to be proportioned by a scaling parameter, while the size of window in Gabor transform is known to be fixed [128]. The standard Morlet wavelet is a complex-valued wavelet that has directionally-dependent real and imaginary parts but is isotropic in magnitude. The new fully-anisotropic Morlet wavelet that we use, is anisotropic in its real and imaginary parts and also in its magnitude.

If we want to explain it briefly, we can say:

The continuous wavelet transform of a 2D space function, $f(X)$, is defined by [129]

$$W_{\psi}f(a,b) = \int_{-\infty}^{+\infty} f(X)\bar{\psi}_{a,b}(X)dX, \tag{6.1}$$

where $W_{\psi}f(a,b)$ is the wavelet coefficient, $X = (x,y)$ is the spatial position, the overbar denotes complex conjugate, and $\psi_{a,b}(X)$ for this 2D domain is given by [130]

$$\psi_{a,b}(X) = \frac{1}{a}\psi(\frac{X-b}{a}), \tag{6.2}$$

where $\psi(X)$ is the mother wavelet, b is a shift parameter, and a is a scale parameter or dilation parameter. The normalization constant $1/a$, is defined such that the total energy of the analyzing wavelet is independent of the scale, i.e.

$$\int_{-\infty}^{+\infty} |\psi_{a,b}(X)|^2 dX = \int_{-\infty}^{+\infty} |\psi(X)|^2 dX \tag{6.3}$$

for all values of a.

As explained before, the wavelet can be any function that has a zero mean and mild decline such that it is non-zero only over a small region. Antoine et al. defined one such function called Morlet wavelet as [131]

$$\psi(X) = e^{ik_0.x}e^{-1/2(x.A^TAx)} - e^{-1/2(k_0B^TBk_0)}e^{-1/2(x.A^TAx)} \tag{6.4}$$

where k_0 is a wave vector, A is an anisotropy matrix, $B = A^{-1}$, and the superscript T denotes the matrix transpose. If $|k_0|$ is sufficiently large, i.e. $|k_0| \geq 5.5$, the second term in equation (6.4) is negligible and can be ignored. The Morlet wavelet is a directional wavelet, which is capable of analysis of different orientations of the random field. This can be accomplished by modification of equation (6.1) to include the variable orientation θ

$$W_\psi f(b,a,\theta) = \frac{1}{a}\int_{-\infty}^{+\infty} f(X)\bar{\psi}(\frac{X-b}{a},\theta)dX, \tag{6.5}$$

The only difference between equation (6.1) and equation (6.5) is that the wavelet and the wavelet coefficient in equation (6.5) are functions of the orientation angle θ.

Kumar [132] controlled the orientation of the wavelet by defining the wave vector as $k_0 = (k_0cos\theta, k_0sin\theta)$ with $k_0 \geq 5.5$ to obtain a wavelet can be rotated through an angle θ. The Morlet wavelet proposed by Kumar [132] has directionally-dependent real and imaginary parts, which allows it to identify dominant orientations in a random field. However, it is isotropic in magnitude and does not take advantage of the anisotropy of random fields. As an development, Neupauer et al. [130] presented a modified fully-anisotropic Morlet wavelet, which takes advantage of both being directional dependent in the real and imaginary part, and also being anisotropic in magnitude. It is noteworthy that strength of an anisotropic Morlet wavelet is in identification of dominant orientations in anisotropic random fields. In this wavelet both the elliptical envelope and the wave vector are rotated through an angle defined by the orientation parameter θ [1]. Fully-anisotropic Morlet complex wavelet transform (AM-CWT) is defined by Neupauer et al as:

$$\psi(x,\theta) = e^{ik_0 C.x} e^{-1/2(Cx.A^T ACx)} \tag{6.6}$$

where $k_0 = (0, k_0)$, $k_0 \geq 5.5$, $A = diag(L, 1)$. L is the anisotropy ratio, defined as the ratio of the scaling factor in the direction perpendicular to θ to the scaling factor in the θ direction. Also, C is a linear transformation matrix given by:

$$C = \begin{bmatrix} cos\theta & sin\theta \\ -sin\theta & cos\theta \end{bmatrix} \tag{6.7}$$

Using this linear transformation causes the entire wavelet rotates through an angle θ, which is defined as positive in the counterclockwise direction. Fig. 6.1 illustrates the real parts of basic, shifted, and scaled Morlet wavelet, and anisotropic wavelet.

In order to obtain powerful textural features of images, the energy of wavelet coefficients for each combination of parameters is also calculated using the equation below:

$$Energy_{a,\theta,L} = \sum_{b_y} \sum_{b_x} |C_{a,\theta,L,b_y,b_x}|^2 \tag{6.8}$$

thus, we will have 225-dimensional feature vector for each wavelet transformation with a certain dilation, angle, and anisotropy ratio (L).

6.2.2 Dual-Tree Complex Wavelet Transform

Another recently-developed and useful kind of wavelet transform is dual tree complex wavelet transform (DT-CWT), which is modified version of discrete wavelet

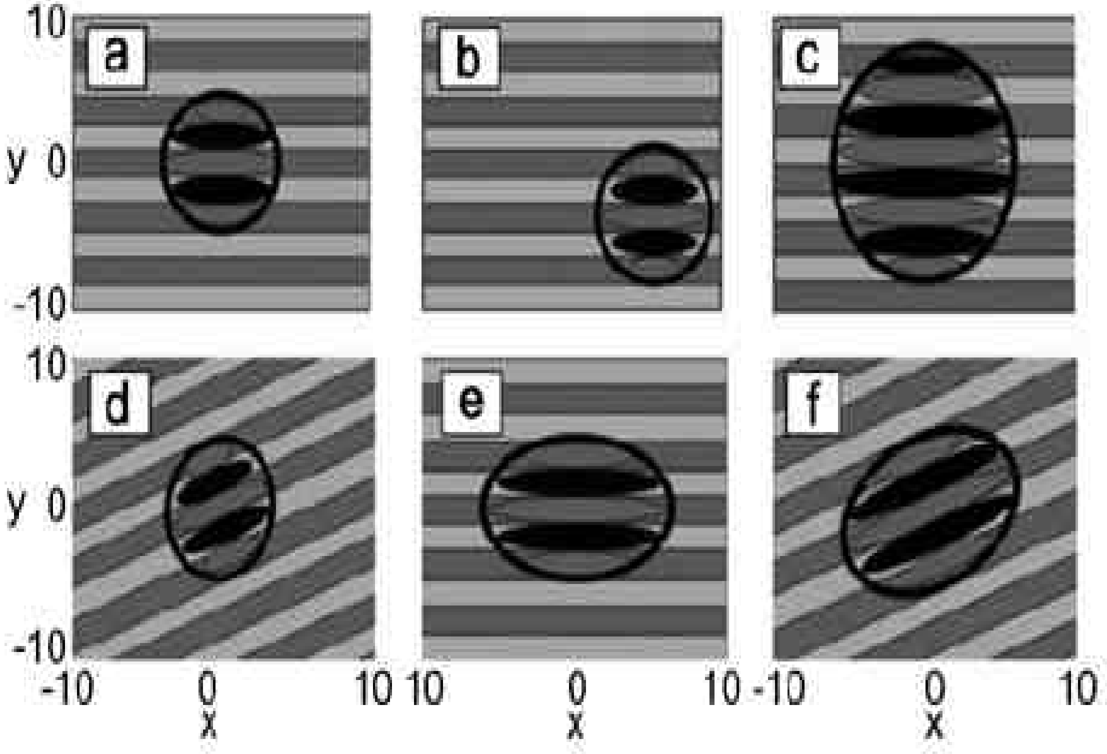

Figure 6.1: Effect of an isotropic Morlet wavelet transform parameters: (a) mother wavelet; (b) shifted wavelet ($b = [6, -4]$); (c) scaled wavelet ($a = 2$); (d) rotated wavelet ($\theta = 30$); (e) anisotropic wavelet ($\theta = 0, L = 0.5$) and (f) anisotropic wavelet ($\theta = 30, L = 0.5$). Black rings represent envelope that contains most energy of wavelet. [1].

transform (DWT). The main limitations of DWT in pattern recognition application is lack of shift invariance and poor directional selectivity because of the decimation operation during the transform [133]. The limitation of being shift variant causes a small shift in the input signal brings very different output wavelet coefficients. In order to overcome these limitations of DWT, Kingsbury [2] introduced dual-tree complex wavelet transform. This method has the following properties: 1) approximate shift invariance, 2) good directional selectivity in 2-D with Gabor-like filters (also true for higher dimensionality, m-D), 3) perfect reconstruction using short linear-phase filters, and 4) limited redundancy, independent of the number of scales, 2m : 1 for m-D. In image processing applications, this method is known to be free of checkerboard artifact, providing better angular resolution, and offering six directional wavelets (165, 135, 105, 75, 45, 15 degrees) [134]. The success of the transform is because of the two trees of real-valued wavelet filters operating on the same data in parallel. These filters are designed such that the two trees produce the real and imaginary parts of the complex-valued coefficients.

Given a 2-D image I, its wavelet transform with respect to the analyzing wavelet of ψ is:

$$I(a,\theta,b) = a^{-1}\int d^2x\bar{\psi}(a^{-1}r_{-\theta}(x-b))i(x) = a\int d^2k e^{ib.k}\widehat{\psi}(ar_{-\theta}k)\widehat{i(k)} \tag{6.9}$$

where the hat sign denotes a Fourier transform and b, a, and θ are translation, dilation, and rotation angle ($r_{-\theta}$ is the rotation matrix) of the analyzing wavelet ψ, respectively. Therefore, complex wavelet transform (CWT) of an image is a function of four variables: two position variables b_x, b_y, a dilation parameter a, and a rotation angle θ. This explains the efficiency of the CWT in treating singularities, since it unfolds them from two to four dimensions. Also, contrary to discrete wavelet transform (DWT), the wavelet function ψ, in the equation above is largely arbitrary and is not determined by the multiresolution scheme.

DT-CWT is composed of two parallel wavelet transforms, and according to the wavelet theory, the wavelet coefficients $d_a^{Re}(k)$ and scaling coefficients $c_j^{Re}(k)$ of the upper tree can be computed via inner products [135]:

$$d_a^{Re}(k) = 2^{a/2} \int_{-\infty}^{+\infty} f(X)\psi_h(2^a X - k)dX \tag{6.10}$$

$$a = 1, ..., j \tag{6.11}$$

$$c_j^{Re}(k) = 2^{j/2} \int_{-\infty}^{+\infty} f(X)\phi_h(2^j X - k)dX \tag{6.12}$$

where l is the scale factor and j is the maximum scale. $\psi(t)$ is real-valued bandpass wavelet and $\phi(t)$ is real-valued lowpass scaling function. Similarly, the coefficients of the lower tree can be computed as:

$$d_a^{Im}(k) = 2^{a/2} \int_{-\infty}^{+\infty} f(X)\psi_g(2^a X - k)dX \qquad a = 1, ..., j \tag{6.13}$$

$$c_j^{Im}(k) = 2^{j/2} \int_{-\infty}^{+\infty} f(X)\phi_g(2^j X - k)dX \tag{6.14}$$

The wavelet and the scaling of the DT-CWT coefficients can then be expressed by combining the output of the dual tree as follows:

$$d_a^{C}(k) = d_a^{Re}(k) + d_a^{Im}(k) \tag{6.15}$$

$$c_j^{C}(k) = c_j^{Re}(k) + c_j^{Im}(k) \tag{6.16}$$

In this application, the coefficients of the high-pass sub-bands of each decomposition level and lowpass sub band from the final level are used as textural features.

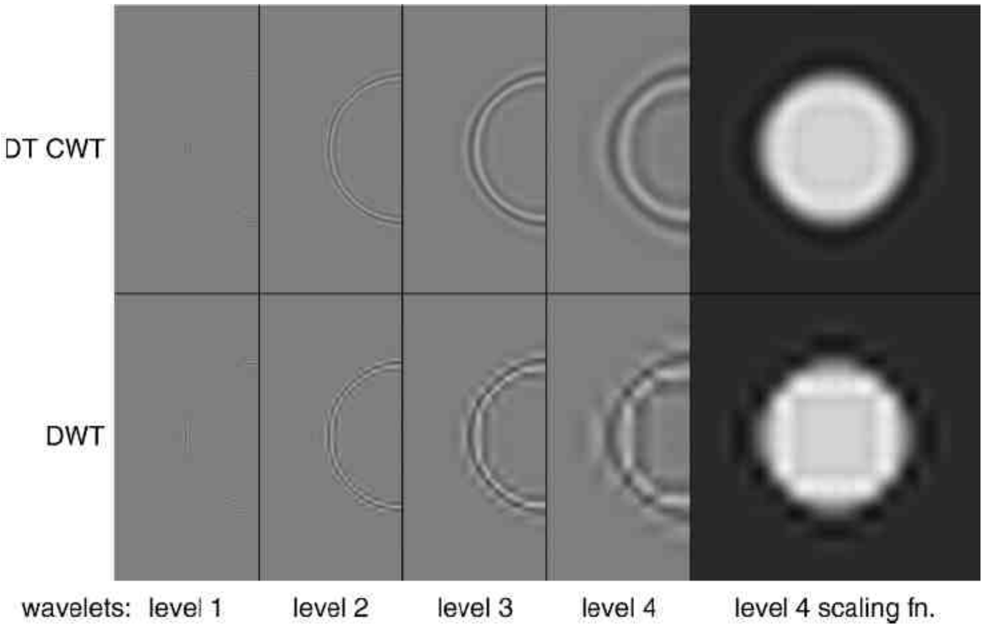

Figure 6.2: Components of the reconstructed image of a light circular disc on a dark background, for wavelets and scaling functions at levels 1 to 4, using the 2-D DT CWT (upper row) and 2-D DWT (lower row). Only half of each wavelet image is shown in order to save space. At each wavelet level, all six directional subbands are retained [2].

6.2.3 Wavelet Transform Decomposition

In two-dimensional images, the wavelet decomposition is acquired as a set of independent, spatially oriented frequency channels. The HH (as it shown is Fig. 6.3) resulting sub image corresponds to diagonal details (high frequencies in both directions - the corners), HL illustrates horizontal high frequencies (vertical edges), LH shows vertical high frequencies (horizontal edges), and the sub image LL shows the lowest frequencies, which is called approximation. In the next step of analysis, the sub image LL is decomposed with the same high pass and low pass filters, while the lowest frequency component is always in the upper left corner of the image. In each stage of the analysis, four sub images are generated whose sizes are reduced twice compared to

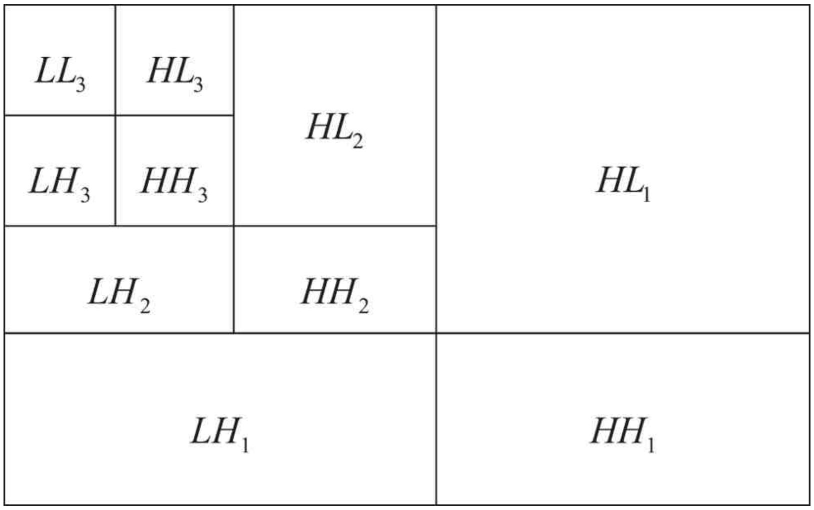

Figure 6.3: Wavelet Decomposition

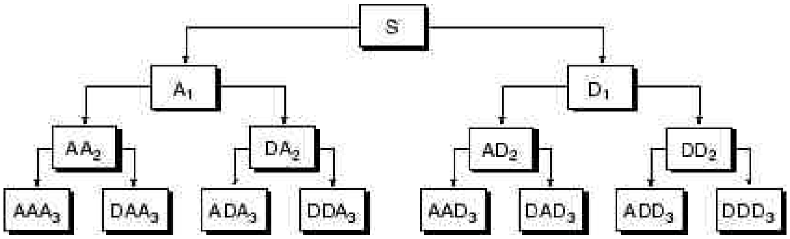

Figure 6.4: Wavelet packet transform

the former scale. Reasonable texture segmentation results can be obtained after 2 to 4 scales of wavelet decomposition. Experience proved that symmetric wavelet functions are superior to non symmetric ones because of the linear-phase property of symmetric filters [136] [137]. In this study, haar wavelet is used for wavelet decomposition.

6.2.4 Wavelet Packet Decomposition

As an extension of the standard wavelets, wavelet packets represent a generalization of the multi-resolution analysis and use the entire family of sub band decomposition to generate an over complete representation of signals. Two-dimensional discrete wavelet packet decomposition allows us to analyze an image simultaneously at different resolution levels and orientations. In 2-D discrete wavelet packet transform (2-D DWPT), an image is decomposed into one approximation and three detail images. The approximation and the detail images are then decomposed into a second-level approximation and detail images, and the process is repeated (as it is shown in Fig. 6.4). The standard 2-D DWPT can be implemented with a low-pass filter and a high-pass filter [138]. The 2-D DWPT of a $N \times M$ discrete image A up to level $P+1$ ($P \leqslant min(\log_2 n, \log_2 m)$) is recursively defined in terms of the coefficients at level p as follows:

$$C^{p+1}_{4k,(i,j)} = \sum_m \sum_n h(m)h(n)C^p_{k,(m+2i,n+2j)} \tag{6.17}$$

$$C^{p+1}_{4k+1,(i,j)} = \sum_m \sum_n h(m)g(n)C^p_{k,(m+2i,n+2j)} \tag{6.18}$$

$$C^{p+1}_{4k+2,(i,j)} = \sum_m \sum_n g(m)h(n)C^p_{k,(m+2i,n+2j)} \tag{6.19}$$

$$C^{p+1}_{4k+3,(i,j)} = \sum_m \sum_n g(m)g(n)C^p_{k,(m+2i,n+2j)} \tag{6.20}$$

where C^0_0 is the image A and k is an index of the nodes in the wavelet packet tree denoting each subband. At each step, the image C^p_k is decomposed into four quarter-size images C^{p+1}_{4k} , C^{p+1}_{4k+1} , C^{p+1}_{4k+2} , and C^{p+1}_{4k+3}.

The coefficients' energy and Shannon entropy in different subbands are computed from the subband coefficient matrix as:

$$Energy_p(k) = \sum_i \sum_j |C^p_{k,(i,j)}|^2 \tag{6.21}$$

$$Entropy_p(k) = -\sum_i \sum_j |C^p_{k,(i,j)}|^2 \log |C^p_{k,(i,j)}|^2 \tag{6.22}$$

Where $Energy_p(k)$ and $Entropy_p(k)$ are the energy and entropy of the image projected onto the subspace at node (p, k). The entropy of each sub band provides a measure of the image characteristics in that sub band. The energy distribution has important discriminatory properties for images and as such can be used as a feature for texture classification. From equation above, it follows that the wavelet entropy is minimum when the image represents an ordered activity characterized by a narrow frequency distribution, whereas the entropy is high when an image contains a broad spectrum of frequency distribution. In this study, Haar mother wavelet was employed to decompose the images to second level of wavelet packet decomposition and Shannon entropies of images at each sub band have been used as image features. Also energies and entropies of sub bands of wavelet decomposition are calculated.

6.3 Feature Selection Using Modified Regularized Winnow Algorithm

Feature selection and feature dimensionality reduction is an important step in machine learning procedure. The focus of feature selection is to select a subset of variables from the input which can efficiently describe the input data while reduces the effect of noise or irrelevant variables, and still provides good prediction results [127]. Feature selection helps in understanding data, reducing computation complexity, reducing the effect of curse of dimensionality, and improving the classifier performance [139].

Winnow algorithm [140, 141] is a binary classifier, which learns linear threshold hypotheses. The algorithm is specialized for binary inputs and is a multiplicative update algorithm which is proved to be appropriate for problems with many irrelevant attributes.

Working with Winnow algorithm, one of the concern is its convergence. Littlestone et al. in [140] show that its convergence is guaranteed for linearly separable data. However, in practical applications, many of data may not always be linearly separable. Zhang [142] sugessted a modification of Winnow which extends its application for linearly non-separable case, and makes a reliable probability estimate. The basic idea is about modification of the original Winnow algorithm to solve a regularized optimization problem. The result of modified Winnow algorithm converges both in the linearly separable case and in the linearly non-separable case. Consider the binary classification problem: to determine a label $y \in \{-1, 1\}$ associated with an input vector x. We need to find a weight vector w and a threshold θ such that $w^T x < \theta$ if its label $y = -1$ and $w^T x \geq \theta$ if its label $y = 1$. For simplicity, θ is assumed to be zero in many applications. The θ restriction does not cause problems in practice since one can always append a constant feature to the input data x, which offsets the effect of θ. Given a set of labeled data $(x_1, y_1), ..., (x_n, y_n)$, this algorithm updates the weight vector w by going through the training data repeatedly. when the algorithm is not able to correctly classify an example, the weight vector is updated.

The Winnow algorithm (with just positive weight) uses multiplicative update: if the linear discriminant function with current weight vector w^{i-1} misclassifies an input training vector x^i with true label y^i, then each component j of the weight vector w^i is updated as:

$$w_j^i \quad \longleftarrow \quad w_j^{i-1} exp(\eta x_j^i y^i) \tag{6.23}$$

where $\eta > 0$ is the learning rate parameter. The initial weight vector can be taken as $w_j = \mu_j > 0$, where μ is a prior which is typically chosen to be uniform (one).

For facing convergence problem for linearly non-separable data, one may partially solve the problem by decreasing the learning rate parameter η during the updates. However, this is not clear what is the best way to do so. Therefore in practice, it is perplexing to implement this idea properly.

Zhang et al. [142] converted Winnow algorithm into a numerical optimization problem that is able to handle linearly non-separable data. Instead of looking at one example at a time as in an online formulation, Zhang incorporated all examples at the same time. A linear weight $\hat{w}$ is defined as:

$$\hat{w} \;=\; arg \;\; \min_{w} \left[\sum_j w_j ln \frac{w_j}{e\mu_j} + c \sum_{i=1}^{n} f(w^T x^i y^i) \right] \tag{6.24}$$

where

$$f(v) = \begin{cases} -2v & v < -1 \\ \frac{1}{2}(v-1)^2 & v \in \{1, 1\} \\ 0 & v > 1 \end{cases} \tag{6.25}$$

and $c > 0$ is a given parameter called the regularization parameter. The optimal solution $\hat{w}$ of the above optimization problem can be derived from the solution $\hat{\alpha}$ of the following dual optimization problem:

$$\begin{aligned} &\hat{\alpha} = \max_{\alpha} \sum_i \left[\alpha^i - \tfrac{1}{2c}(\alpha^i)^2\right] - \sum_j \mu_j exp(\sum_i \alpha^i x_j^i y^i) \\ &s.t.\ \ \alpha^i \in [0, 2c] \quad (i = 1, ..., n). \end{aligned} \tag{6.26}$$

The j-th component of $\hat{w}$ is given by

$$\hat{w}_j = \mu_j exp(\sum_{i=1}^{n} \hat{\alpha}^i x_j^i y^i) \tag{6.27}$$

A Winnow-like update rule can be derived for the dual regularized Winnow formulation. At each data point (x^i, y^i), all $\alpha_k s$ with $k \neq i$ are calculated, and α^i is updated to approximately maximize the dual objective functional using gradient ascent:

$$\alpha^i \ \rightarrow \ max(\ min(\ 2c\ ,\ \alpha^i + \eta(1 - \frac{\alpha^i}{c} - w^T x^i y^i)\ )\ ,\ 0\ ) \tag{6.28}$$

where

$$w_j = \mu_j exp(\sum_{i=1}^{n} \alpha^i x_j^i y^i) \tag{6.29}$$

The dual variable α is initialized to be zero, which corresponds to $w = \mu$. Then α and w are updated by repeatedly going over the data sequentially from $i = 1, ..., n$. The α^i is memorized and when the same point is revisited in later iterations, the memorized α^i is applied in the formula.

Littlestone [140] shows that the original Winnow method was robust to irrelevant features in that the number of mistakes it makes to obtain a classifier (in the separable case) depends only logarithmically on the dimensionality of the feature space.

Generalization bounds of regularized Winnow that are similar to the mistake bound of the original Winnow (in the sense of logarithmic dependent on the dimensionality) have been given by Zhang [143]. These results imply that the new method, while it can properly handle non-separable data, shares similar theoretical advantages of Winnow in that it is also robust to irrelevant features.

As it was mentioned before, regularized Winnow algorithm is a classifier for binary input. Using Winnow algorithm as a feature selection method, the problem we have is the non-binary extracted features from brain MR images. For facing this issue, we quantize each feature to be either zero or one. The threshold value that is used for quantization is determined by finding the median of the values of each feature such that half of the samples have values less than the threshold and the other half greater than the threshold. Since the number of healthy and tumor samples are equal, in the ideal case, i.e., the most discriminating feature, either zero or one will be assigned to the same class. Quantizing each feature into two levels as zero and one, we will obtain a binary feature vector suitable for regularized Winnow algorithm. Note that the obtained threshold values are used to quantize the feature vectors of the testing samples. After applying the Winnow algorithm, the weights assigned for the features represent the discriminative power of each feature. Feature selection can be done by selecting the most discriminative feature. This feature selection method has the advantage of being fast and efficient in dealing with many irrelevant attributes.

6.4 Skippy Greedy Snake Algorithm

Snake is an active contour model (ACM) and a energy-minimizing spline guided by external constraint forces and influenced by image forces that pull it toward features such as lines and edges [144]. The snake is a method of contour representation with a number of nodes $\upsilon(s)$, called snaxels, where s is the normalized arc length in the range $0 < s < 1$ [3]. The convergence is governed by two energy functions, the internal energy $E_{internal}$ and the external energy $E_{external}$, which are defined based on the template properties and the image properties, respectively. $E_{internal}$ consists of two terms, the continuity force and the curvature force, denoted as E_{cont} and E_{curv}, respectively. The energy functional to be minimized for a snake with N snaxels is as follows [3]:

$$\sum_{i=0}^{N-1} E(\upsilon(i), j) = \sum_{i=0}^{N-1} \left\{ \begin{array}{l} \alpha_i E_{count}(\upsilon(i), j) \\ +\beta_i E_{curv}(\upsilon(i), j) \\ -\gamma_i E_{image}(\upsilon(i), j) \end{array} \right\}. \tag{6.30}$$

where j refers to the G_p neighboring pixel positions under examination with step size δ_k which is based on a pixel search pattern (p), around the i^{th} snaxel, where $j = j \pm \delta_k$, $\delta \in 0, \pm 1, ...$ The snaxel movement is to choose the pixel in the neighborhood that minimize the equation 6.30. For the traditional snakes (greedy snake algorithm), step size is $\delta \in 0, \pm 1, ...$, which means that all the pixels are at the first degree neighborhood relation at all directions. The coefficients α, β, and γ are weighting factors that control the relative importance of the continuity energy, bending energy, and image forces, respectively. The continuity energy $E_{cont}(\upsilon(i), j)$ is approximated as the first-order continuity function of the snaxels with

$$E_{count}(\upsilon(i), j) = \frac{|d_{avr} - d_{\upsilon(i)-\upsilon((i+1),j)}|}{max\{|d_{avr} - d_{\upsilon(i)-\upsilon((i+1),j)}|\}} \tag{6.31}$$

where $d_{\upsilon(i)-\upsilon((i+1),j)}$ refers to the distance between the two consecutive snaxels $\upsilon(i)$ and $\upsilon(i+1,j)$. The average distance between the adjacent pixels is as follows:

$$d_{avr} = (1/N)\sum_{i=0}^{N-1} d_{\upsilon(i)-\upsilon((i+1),j)} \tag{6.32}$$

E_{cont} is the degree of uniformity of the distance distribution between adjacent snaxels of a contour. When the distances between the adjacent snaxels are close to the average distance d_{avr}, $E_{cont}(\upsilon(i),j)$ approaches zero. d_{avr} is updated at the end of each iteration.

The continuity term encourages the snaxels to be evenly spaced, while the curvature energy indicates the degree to which a snaxel is being bent with respect to its two adjacent snaxels. E_{curv} is calculated as follows:

$$E_{curv}(\upsilon(i),j) = \frac{|\upsilon(i-1) - 2\upsilon(i,j) + \upsilon(i+1)|}{max\{|\upsilon(i-1) - 2\upsilon(i,j) + \upsilon(i+1)|\}} \tag{6.33}$$

These two energy terms are normalized by the respective largest values in the neighborhood. The counteracting energy functional $E_{image}(\upsilon(i),j)$, which is also to be normalized, is defined based on the local gradient magnitude as follows:

$$E_{image}(\upsilon(i),j) = \frac{I(\upsilon(i),j)}{max(I(\upsilon(i),j)) - min(I(\upsilon(i),j))} \tag{6.34}$$

where $I(\upsilon(i),j)$ represents the intensity gradient at the point j of the snaxel $\upsilon(i)$ with a step size of $\pm\delta$, and and $min(I)$ and $max(I)$ are the minimum and maximum gradients for all G_p pixels in the neighborhood. The new position of the snaxels is the one that results in the maximum reduction of the total energy based on 6.30.

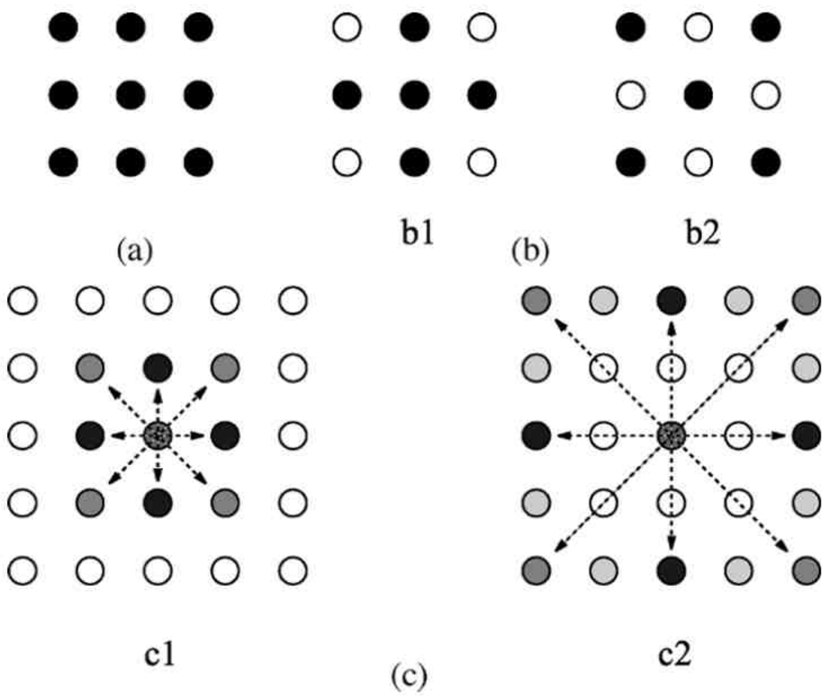

Figure 6.5: Black pixels are examined for a possible local minimum (a) in GSA, (b) in FGSA alternating between the patterns b1 and b2, and (c) in the case of SGSA, the step sizes of adjacent snaxels are alternated between the step size $\delta_0 = 1$ in c1 and $\delta_1 = 2$ in c2 [3].

Greedy snake algorithm (GSA) [145] and fast greedy snake algorithm (FGSA) [146] search for the new position of a snaxel based on search patterns with a step size δ equal to 1. In the case of the GSA, the energy functional is computed at each snaxel for its current pixel and for its eight neighboring pixels, to determine its new position in an iteration. Therefore, the number of neighboring pixels examined is 9, as shown in Fig. 6.5(a). The FGSA employs two patterns that are swapped alternately at successive iterations, so the number of pixels examined is reduced to 5. One FGSA search pattern has a cross pattern shape and the other has a diagonal pattern shape, as illustrated in Fig. 6.5(b) [3].

The main limitation of snake algorithm is possibility of getting trapped around an undesired local minimum due to the slithering behavior of convergence [3,147]. In this sense, FGSA has the advantage of introducing a perturbation type of behavior. Nevertheless, FGSA still has a high probability of being trapped around an undesirable local minimum. Possible methods of escaping from the local minima include the exploration of all possible positions of the snake and the application of simulated annealing. However, these approaches are too computational for practical applications. Possible solutions to alleviate the effect of local minima are to smooth the images with either a median or Gaussian filter with a large window size, and to increase the step size of the search windows. In fact, a snaxel in FGSA cannot move in a straight path because of the use of alternate patterns. The maximum cost occurs when the routing path is a vertical or a horizontal straight line. In this case, the number of iterations required will be doubled, and, therefore, the advantage of reducing pixels to be examined will disappear.

Skippy greedy snake algorithm introduced by Sakalli et al. [3] uses two different step sizes as denoted by δ_0 and δ_1. The step sizes of even and odd ordered snaxels alternate between $\delta_0 = 1$ and $\delta_1 = 2$ at each iteration. The step size of the search can be set to a higher value if the neighboring pixels are highly correlated, which is the case pointed out for natural images [148]. Therefore, the pixels in the vicinity of the current snaxel can be searched in a skipped way. However, it is possible that a pixel position which can produce a smaller value of energy functional might be skipped. This implies that the step sizes should be selected in such a way that all possible positions can be reached by the snaxels, particularly in the fine tuning stage. For the same reason, if the step sizes are chosen to be large, then alternate step sizes between adjacent snaxels moving in shorter step sizes will probably prevent the snaxels from going astray. Using this idea, the pixels that are skipped during the large step size will be examined with the small step size in the reverse direction.

In comparison of FGSA and SGSA, it is seen that FGSA requires a higher number of iterations, while SGSA a fewer iterations [3]. The efficiency achieved by FGSA is due to the fact that a less number of pixels are examined in a larger area for any search pattern. When the reduction in pixel numbers to be examined is taken into account, the FGSA has a computational efficiency of 1.2 to 1.35 times of GSA. The SGSA achieves a higher efficiency level, reaching 1.5 times of GSA when the number of iterations exceeds 20. Therefore, the computational efficiency of the skippy greedy snake algorithm is higher than that of the fast GSA.

The common factor which is important in three snake algorithms is specifying appropriate initial points. Determining suitable initial points has a great impact on the accuracy of snake algorithm in segmentation. In this study, we apply skippy greedy snake algorithm for last step of the proposed segmentation system. Appropriate initial points are established using the determined region as tumor lesion by third step of the system.

6.5 System Approach

Skippy greedy snake algorithm in capable of segmenting the tumor area however the algorithm's accuracy and performance depends significantly on its initial points. In this chapter, a novel algorithm is presented to automatically find proper initial points which not only obviates the requirement of manual interference but also increase the accuracy and speed of optimization convergence. The same methods as

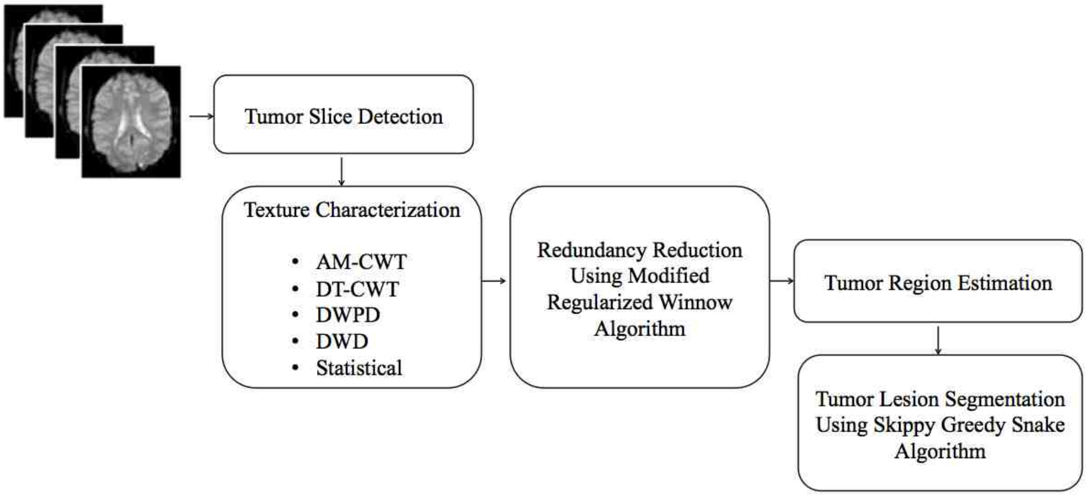

Figure 6.6: System overview

mentioned in previous chapter are used for tumor slice detection and MRI intensity normalization. After detection of a slice containing tumor lesion, it is fed into the segmentation stage, which localizes the tumor area. The candidate tumor regions are obtained using a sliding window with step size of 5 pixels, which sweeps through the whole brain tissue. A tumor classification approach is then applied on every instance of the window. If the window is classified to have tumor, the central pixel of the window will be labeled as tumor. On the other hand, if it is classified as healthy, the central pixel will be labeled as healthy. The obtained candidate pixels determined by our method to be as tumor lesion are used to construct the initial points for active contour model implemented with skippy greedy snake algorithm. The system overview is depicted in Fig. 6.6

6.5.1 Windowing

In order to create the training set, we automatically crop random windows from each selected hemisphere containing tumor. Having the brain midline and borderline helps us to restrict the windows to just cover the brain tissue and not the background. For the testing step, a same size sliding window sweeps all over the brain, excluding the background area. The sweeping steps of sliding window are 5 pixels. The computation complexity of sliding window presented in the previous chapter is reduced by 25 times in this application. A set of statistical and wavelet features are extracted using the aforementioned feature extraction methods from each instance of the sliding window.

6.5.2 Feature Aggregation

Different statistical and wavelet features are extracted from each instance of the window. Wavelet features are extracted using DT-CWT, AM-CWT, wavelet decomposition and wavelet packet decomposition, as described in Section 6.2.

We use Yl, Yh, and $Yscale$ features from Dual Tree complex wavelet transformation, where Yl is a cell array including the lowpass sub band from the final level, Yh is a cell array containing the highpass subband for each level and $Yscale$ is a cell array containing the lowpass coefficients at every scale. The length of the Dual Tree feature vector is 180.

Morlet-wavelet features are extracted by applying Morlet-wavelet kernels with two different scales and eight orientations. Including wavelet energy feature, the length of feature vector is 1616.

Table 6.1: Brain tumor segmentation accuracy using different feature sets on T1-w images of simulated data

	NN		3-NN		5-NN		7-NN	
Feature Type	Acc.	Dim.	Acc.	Dim.	Acc.	Dim.	Acc.	Dim.
DT-CWT	93.25	180	93.37	180	93.63	180	93.64	180
AM-CWT	94.16	1616	94.02	1616	93.95	1616	93.92	1616
DWPT	91.93	128	91.78	128	91.71	128	91.59	128
DWT	93.42	273	93.55	273	93.68	273	93.66	273
Statistical	89.6	475	90.1	475	91.9	475	92.5	475
Total	90.1	2672	90.22	2672	91.36	2672	91.6	2672
Winnow	92.3	70	92.72	100	92.85	100	93.2	100

Table 6.2: Brain tumor segmentation accuracy using different feature sets on FLAIR images of real data

	NN		3-NN		5-NN		7-NN	
Feature Type	Acc.	Dim.	Acc.	Dim.	Acc.	Dim.	Acc.	Dim.
DT-CWT	88.02	180	88.14	180	88.37	180	88.41	180
AM-CWT	90.05	1616	90.09	1616	90.11	1616	90.24	1616
DWPT	88.38	128	88.26	128	88.16	128	88.12	128
DWT	87.55	273	87.59	273	87.62	273	87.65	273
Statistical	86.5	475	86.9	475	87.7	475	88.4	475
Total	87.08	2672	88.35	2672	88.35	2672	88.48	2672
Winnow	90.5	70	90.8	100	91.3	100	91.5	100

Table 6.3: Tumor segmentation results using WWSS method

	Simulated T1	Simulated FLAIR	Simulated T2	Real T1	Real FLAIR	Real T2
Sensitivity	86.4 ± 0.6	90.64 ± 0.4	88.1 ± 0.3	78.65 ± 0.2	84.92 ± 0.4	77.43 ± 0.2
Specificity	98.8 ± 0.1	97.78 ± 0.5	97.31 ± 0.4	97.49 ± 0.1	95.12 ± 0.2	96.35 ± 0.5
Accuracy	96.6 ± 0.2	96.8 ± 0.3	96.1 ± 0.1	93.4 ± 0.4	93.8 ± 0.1	92.3 ± 0.2
Similarity Index	92.33 ± 0.1	91.38 ± 0.3	91.18 ± 0.1	85.72 ± 0.2	84.4 ± 0.4	83.23 ± 0.5

Table 6.4: Comparing tumor segmentation accuracy using WWSS method and our previous method

	Simulated T1	Simulated FLAIR	Simulated T2	Real T1	Real FLAIR	Real T2
Method in chapter 5	95.7 ± 0.3	95.9 ± 0.4	94.8 ± 0.1	92.3 ± 0.1	93.2 ± 0.3	91.7 ± 0.4
Current Method	96.6 ± 0.2	96.8 ± 0.3	96.1 ± 0.1	93.4 ± 0.4	93.8 ± 0.1	92.3 ± 0.2

The length of the feature vector achieved from applying 2D wavelet packet decomposition on each window is 128. In addition, using 2D wavelet transform decomposition on each window results in creating a 273 dimensional feature vector.

The total wavelet feature vector is a 2197-dimensional feature vector. In addition to wavelet features, the statistical features including 7 first-order statistical features, 20 GLRLM features, 112 GLCM features, 80 HOG features, and 256 LBP features, which makes a 475-dimentional statistical feature vector is added to feature pool. Concatenation of statistical and wavelet features creates a 2672-dimensional feature vector.

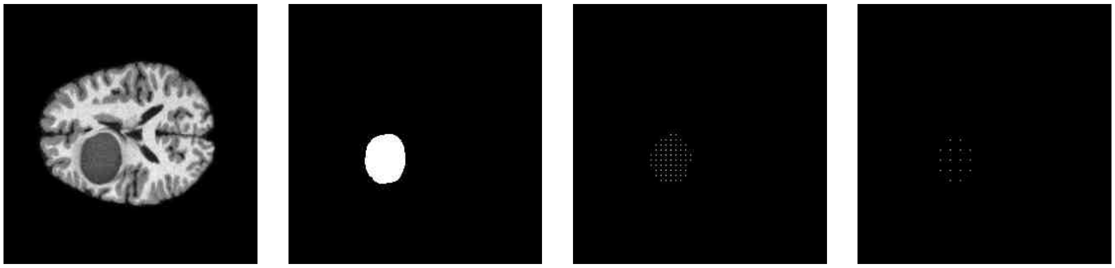

Figure 6.7: Examples of tumor lesion segmentation on simulated T1-w sample. (a) original data, (b) golden label, (c) segmented tumor using sliding window with 5 pixels steps, (d)segmented tumor using sliding window with 10 pixels steps

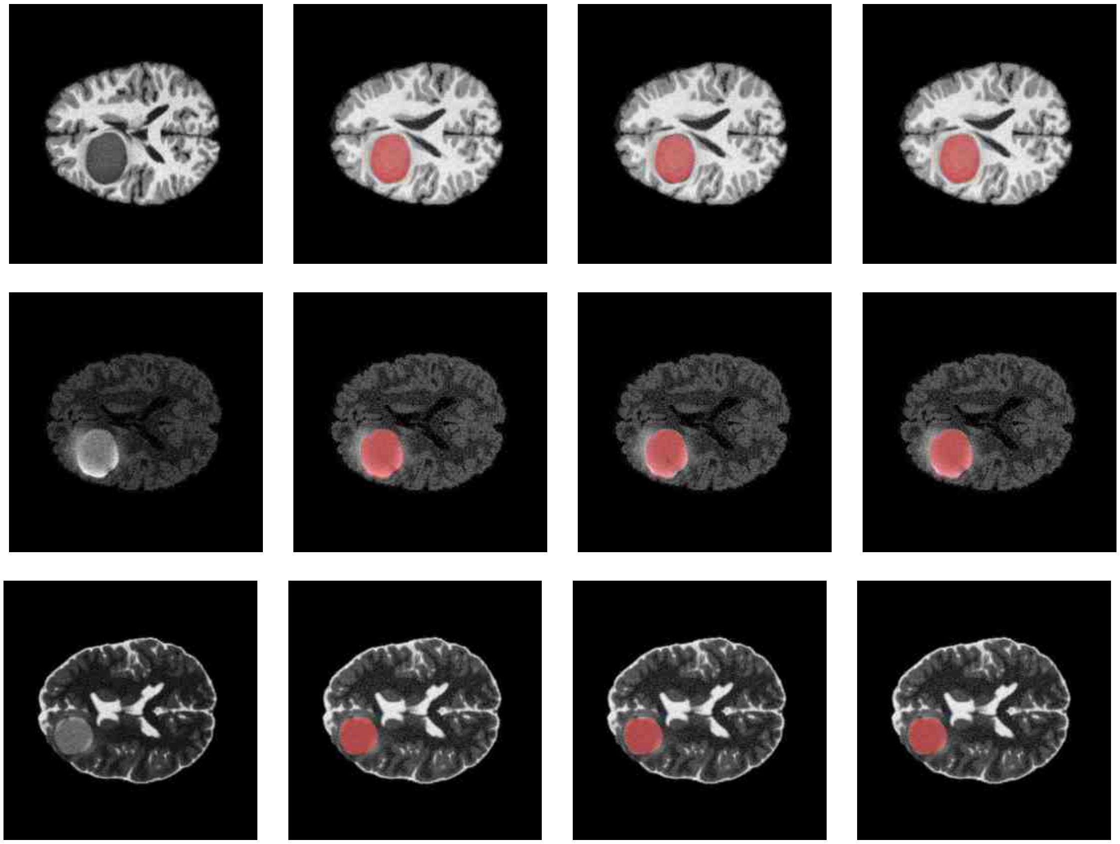
(i) (j) (k)

Figure 6.8: Examples of tumor lesion segmentation on T1-w (first row), FLAIR (second row) and T2-w (third row) simulated data. (a) original data, (b) golden label, (c) segmented lesion after consistency verification, (d)segmented lesion using snake algorithm

6.5.3 Feature Selection and Classifications

After a slice is recognized to have tumor, segmentation step is applied to localize tumor area. The candidate tumor regions are acquired using a sliding window that sweeps the whole brain tissues with 5 pixels step size. In comparison with previous chapter, using 5 pixels step size causes to reduce computational time by 25 times. Different Wavelet feature sets are extracted from each instance of the window. After applying modified regularized Winnow algorithm for feature selection on each feature

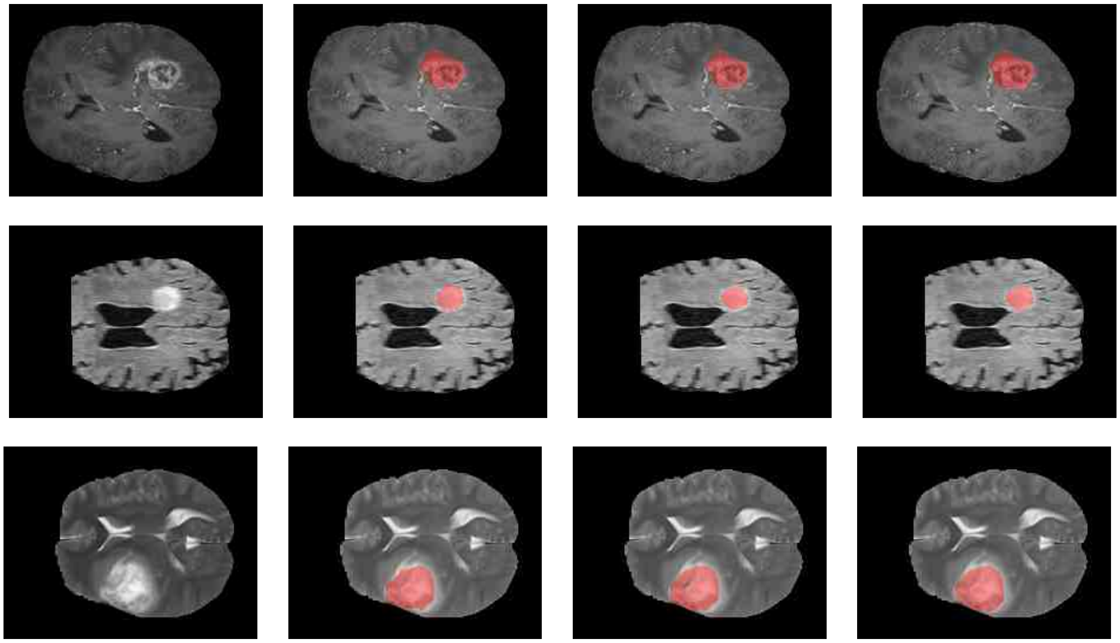

(i) (j) (k) (l)

Figure 6.9: Examples of tumor lesion segmentation on T1-w (first row), FLAIR (second row) and T2-w (third row) simulated data. (a) original data, (b) golden label, (c) segmented lesion after consistency verification, (d)segmented lesion using snake algorithm

set, they are classified into either tumor or healthy. If the window is classified to have tumor, the central pixel of the window is labeled as tumor. On the other hand, if it is classified as healthy, the central pixel is labeled as healthy. For classification, k nearest neighborhood is applied on both real and simulated data. The results are represented in Table 6.1 and Table 6.2 for simulated and real data, respectively.

The candidate pixels obtained from kNN classifier are used in constructing the initial points of skippy greedy snakes algorithm. Fig. 6.7 depicts segmented tumor using sliding window with 5 and 10 pixels steps. Greedy snake is an ACM and an energy-minimizing spline guided by external constraint forces and influenced by image forces that pull it towards features such as lines and edges [144]. Energy function

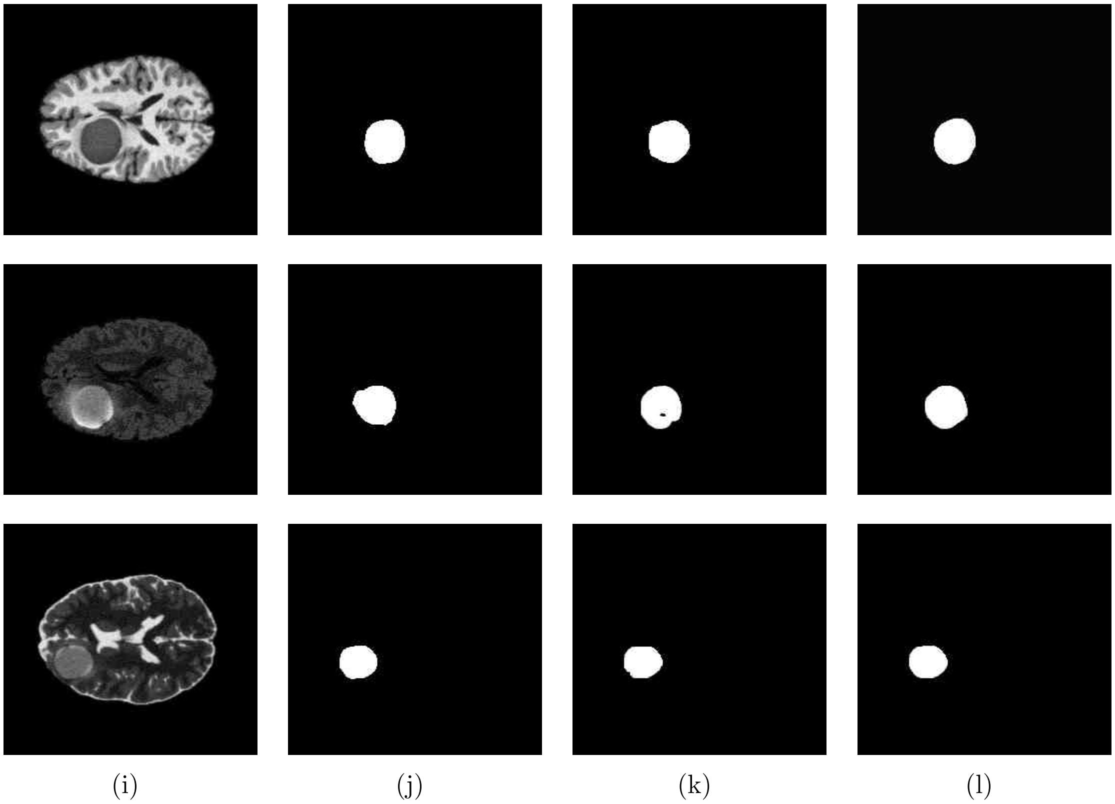

Figure 6.10: Examples of tumor lesion segmentation on T1-w (first row), FLAIR (second row) and T2-w (third row) simulated data. (a) original data, (b) golden label, (c) segmented lesion using sliding window after consistency verification, (d)segmented lesion using snake algorithm

consists of three components as: continuity, curvature, and gradient. Each of these components is weighted by a specified parameter to make the total energy. In this algorithm, initial points need to be defined in the region of interest. The initial points are usually in the shape of an elliptic contour, which is specified manually. This is considered as one of the main limitations of snake algorithm. The location of the initial points are updated through an iterative process. Energy function for each point in a local neighborhood is calculated. Each point moves to the point with lowest energy function. This procedure repeats until termination condition met, which can be

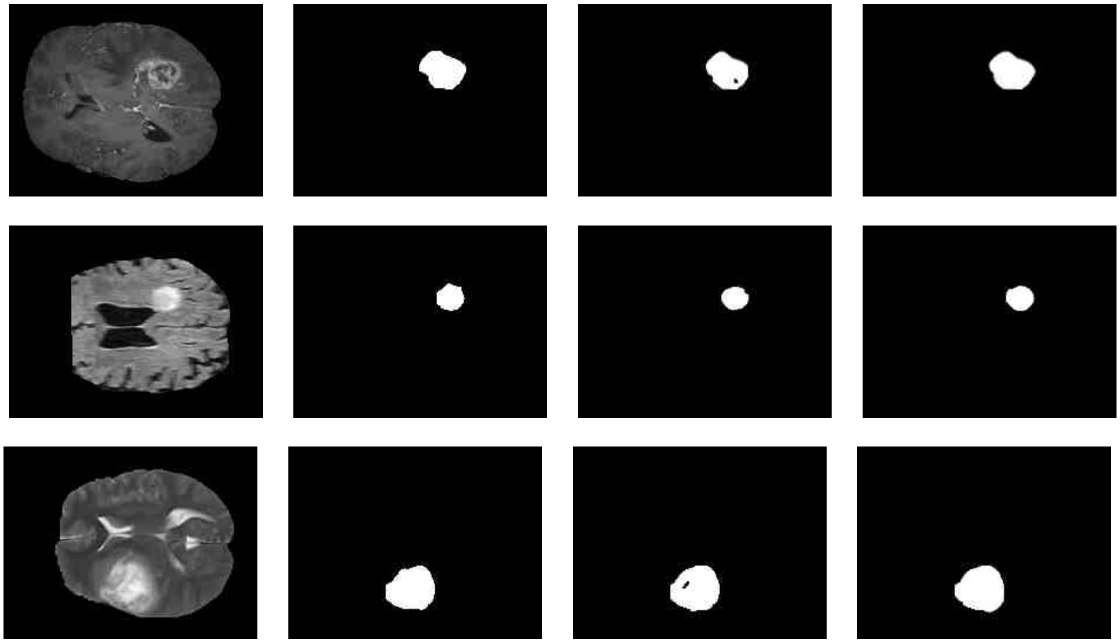
(i) (j) (k) (l)

Figure 6.11: Examples of tumor lesion segmentation on T1-w (first row), FLAIR (second row) and T2-w (third row) real data. (a) original data, (b) golden label, (c) segmented lesion using sliding window after consistency verification, (d)segmented lesion using snake algorithm

either a defined number of iterations, or stability of the position of the points. Specifying the proper initial points has a great influence on the accuracy and convergence speed of the skippy greedy snakes algorithm. In addition, it satisfies the requirement of human interference to manually specify initial points. The proposed approach labels some pixels to be in the tumor region, which determines the approximate tumor area. Peripheral shape obtained from outside boundary of the segmented tumor are used as initial points of skippy greedy snakes algorithm. This method facilitate the tumor segmentation procedure and decrease the computational complexity. The average required time for tumor segmentation in each detected image using previous chapter method is around 2630ms, while applying the current method the average

Table 6.5: Comparing WWSS method with other methods

Algorithm Dep. on	[120]	[121]	[20]	[122]	[123]	[124]	[55]	[125]	[126]	[149]	WWSS
Bias correction	-	-	-	√	√	-	√	-	-	-	-
Registration	-	√	√	√	√	√	√	-	-	-	-
Multi-spectral MRI	-	√	√	√	√	-	√	-	-	-	-
Initial assumptions	-	-	-	√	-	-	-	-	-	-	-
High quality data	-	√	√	-	-	-	-	-	√	-	-
Manual intervention	√	-	-	-	-	-	-	-	-	-	-
over-segmentation	√	-	-	-	-	-	-	√	-	-	-
High computational complexity	-	-	-	-	√	√	√	√	√	√	-

time is around 140ms. The processing time decrement is very valuable in facing large database. Fig 6.8 and Fig 6.9 show samples of tumor segmentation on T1-w, FLAIR, and T2-w images of simulated and real data, respectively. Each row includes a sample of the original data, the golden label of tumor, segmented lesion after consistency verification, and segmented lesion using snake algorithm. In order to make the differences more visible, Fig 6.10 and Fig 6.11 show the segmented region corresponding to the samples illustrated in Fig 6.8 and Fig 6.9. It is seen that the snake algorithm has provided better results than previous method. The obtained segmentation accuracy is presented in Table 6.3. It is worthy to note that specificity has a higher value than sensitivity in this experiment. The comparison of this method and method presented in previous chapter is shown in Table 6.4. Applying this technique, besides higher accuracy, the computational complexity is considerably decreased. Table 7.2 shows the comparison of the current method, which is called WWSS with other well-known techniques.

6.6 Conclusion

This chapter presents a new method to accelerate and improve the brain tumor segmentation accuracy of the previous framework. In order to reduce the computational complexity and expedite the segmentation algorithm, and also to improve the system performance, some modifications are applied in the segmentation algorithm presented in previous chapter. The algorithm modifications are applied in three main phases: feature extraction, feature selection, and tumor localization. Beside other texture-based feature extraction methods mentioned in previous chapter, fully anisotropic complex wavelet, and dual tree complex wavelet transform are employed for feature extraction on brain MR images. It is worth mentioning that for the first time, anisotropic Morlet complex wavelet transform and dual-tree complex wavelet transform are applied in tumor segmentation study. These features are capable of extracting directional texture information and presenting trends, breakdown points, discontinuities in higher derivatives, and self-similarity of brain MR images. Adding these features to the existed feature pool increases the size of feature pool excessively. For defying the curse of dimensionality, a novel feature selection technique based on regularized Winnow algorithm is presented. RWA is originally a classifier, however, the low complexity of this method motivates to employ it in feature selection. While RWA classifier works with binary feature vectors, it is modified to not only work as a feature selection technique but also to be able to handle non-binary features. The presented feature selection method is fast and efficient in dealing with many irrelevant features. For localizing the tumor area, a sliding window as explained in the previous chapter is used. The difference is here the sliding window sweeps through whole brain tissue with step size of five pixels. It decreases the calculation complexity by 25 times. A tumor classification approach is then applied on every instance of the window. Then, the obtained candidate pixels determined by this method to be as tumor are used to construct the initial points for skippy greedy Snake algorithm, which is a contour-based algorithm. Specifying the appropriate initial points has a great influence on the accuracy and convergence speed of the skippy greedy snakes algorithm. In addition, it satisfies the requirement of human interference to manually specify initial points. More accurate results are obtained for brain tumor segmentation.

As it was mentioned earlier segmentation methods can be categorized into three general groups as contour-based, region-based, and texture-based approaches [4]. This method is a combination of texture-based and contour-based algorithms. Similar to previous system, this system is independent of atlas registration, prior anatomical knowledge, bias corrections, and multi-spectral MR images. Additionally, it is fully automatic, and does not require manual initialization. Despite some other methods that need to have the initial assumptions, such as a given number of tissue classes or a multi-scale classification, this algorithm does not need any such information. This makes the proposed algorithm much more robust and more general than other methods. Comparing with the previous system, it is more computationally efficient and provides higher segmentation accuracy.

CHAPTER 7

Brain Tumor Segmentation Using Multi-Spectral MR Images Based on Canonical Correlation Analysis

7.1 Introductory Remarks

Using the algorithm proposed in the previous chapter, the maximum obtained accuracy for tumor segmentation was 96.8% for the database of simulated MR images and 93.8% for the database of real MR images. In order to improve the system performance for the real MR data, a multi-spectral approach based on information fusion using canonical correlation analysis (CCA) is presented in this chapter.

As it was mentioned in the previous chapters, the intensity similarities between brain lesions and some normal tissues result in confusion within the algorithm. For example, if the lesion is inside the white matter (WM), there is overlapping intensity distributions between white matter lesion (WML) and grey matter (GM). In order to overcome this problem, many researchers use multi-spectral MR images for lesion identification [20–29].

In the application of brain tumor segmentation, a typical system can be divided into four main modules:

- Capturing the raw data
- Feature extraction module, which processes the data to extract a feature set that is a compact representation of the trait
- Matching module, which employs a classifier to compare the extracted probe feature set with the templates in the gallery set to generate matching scores
- Decision module, which uses the matching scores to recognize the probe template [150].

In a multimodal system, information reconciliation can occur in any of the aforementioned modules.

- Fusion at the data or feature level: Either the data itself or the feature sets originating from multiple sensors/sources are fused.
- Fusion at the match score level: The scores generated by multiple classifiers pertaining to different modalities are combined.
- Fusion at the decision level: The final output of multiple classifiers are consolidated via techniques such as majority voting [151].

Lesion segmentation systems that integrate information at an early stage of processing are believed to be more effective than those systems which perform integration at a later stage. Since the feature set contains richer information about the input data than the matching score or the output decision of a matcher, fusion at the feature level is expected to provide better recognition results. Most studies apply the information fusion in the decision level, because fusion at feature level is difficult to achieve in practice. The main reason for this is incompatibility of feature sets of the various modalities. Fusion at the decision level is considered to be rigid due to the availability of limited information. Thus, fusion at the match score level is usually preferred, as it is relatively easy to access and combine the scores presented by the different modalities [150].

Even though analysis of several sets of data, either of the same type as in multitask or multisubject data, or of different type or nature as in multimodal data, is prevalent in many fields like biometric or biomedical studies, it is still a challenging problem in biomedical image analysis because of the rich nature of the data made available by different imaging modalities [152]. Since each modality or sequence has its own advantages and data content, fusion of data from different modalities or sequences promises to provide a better understanding of the problem. The main purpose of analyzing multiple modalities is to utilize the common as well as unique information from complementary modalities to reach better understanding.

In this study, feature level fusion is used to combine information from two MRI sequences. Canonical correlation analysis (CCA) as a well-known tool for feature level fusion is employed. It is worth mentioning that for the first time CCA is applied for combining MRI sequences in order to segment tumor. CCA is one of the statistical methods dealing with the mutual relationships between two random vectors, and it has the same importance as principal component analysis (PCA) and linear discriminant analysis (LDA) in multivariate statistical analysis. It is one of the valuable multi-data processing methods. In recent years, CCA has been applied to several fields such as signal processing, computer vision, neural network and speech recognition [153]. Even though data fusion increases computational complexity of the segmentation algorithm, it results in higher accuracy. That is a trade-off between accuracy and computational cost.

In order to create the training set, random windowing method explained in Chapter 5 is used for cropping brain tissue from each selected hemisphere containing tumor. The only difference is that for each window instance, the corresponding region in other MR sequence is also attained at the same time. Different statistical and wavelet features are extracted from the cropped brain tissues. The feature vectors attained from two different MRI contrast mechanisms are then fused using CCA. The fused feature vectors are used to train the classifier.

For the test step, a sliding window of the same size sweeps all over the brain tissue simultaneously in two different MR sequences. Two sets of features are extracted from the corresponding window instance using the aforementioned feature extraction methods. CCA is used to fuse the extracted features from two different MR images. After data fusion, support vector machines classifier labels the window either as healthy or tumor. The label is assigned to the central pixel of the window.

7.2 Canonical Correlation Analysis

Canonical correlation analysis, developed by H. Hotelling [154], is a way of measuring the linear relationship between two multidimensional variables [155]. It finds two bases, one for each variable, that are optimal with respect to correlations, and at the same time, it finds the corresponding correlations. In other words, it seeks for two bases in which the correlation matrix between the variables is diagonal and the correlations on the main diagonal are maximized. The dimensionality of these new bases is equal to or less than the smallest rank of the two variables.

An important property of canonical correlations is that they are invariant with respect to affine transformations of the variables. This is the most important difference between CCA and ordinary correlation analysis, which highly depends on the basis in which the variables are described. Although it has been a standard tool in statistical analysis, and used in economics, meteorology and even in classification of malt whisky, CCA is surprisingly unknown in the fields of machine learning and signal processing.

Let $X = (x_1, x_2, ..., x_n) \in \mathbb{R}^{p \times n}$ and $Y = (y_1, y_2, ..., y_n) \in \mathbb{R}^{q \times n}$ be two sets of feature vectors of length p and q extracted from n samples. CCA aims to find two sets of basis vectors, w_x and w_y for the two sets of variables X and Y, such that the correlation between the projections of the two variables into these canonical vectors $x_i^* = w_x^T(x_i - \bar{x})$ and $y_i^* = w_y^T(y_i - \bar{y})$, $i = 1, 2, ..., n$ are mutually maximized. In other words, if ρ is defined as below, ρ needs to be maximized.

$$\rho = \frac{E[xy]}{(E[x^2]E[y^2])^{1/2}} = \frac{E[w_x^T X Y w_y]}{(E[w_x^T X X^T w_x] E[w_y^T Y Y^T w_y])^{1/2}} \,. \tag{7.1}$$

Hence, it is equal as

$$\rho = \frac{w_x^T C_{xy} w_y}{(w_x^T C_{xx} w_x w_y^T C_{yy} w_y)^{1/2}} \,, \tag{7.2}$$

where $C_{xx} \in \mathbb{R}^{p \times p}$ and $C_{yy} \in \mathbb{R}^{q \times q}$ are the within-set covariance matrices of x and y, respectively, while $C_{xy} \in \mathbb{R}^{p \times q}$ is the between-set covariance matrix.

Let

$$A = \begin{pmatrix} 0 & C_{xy} \\ C_{yx} & 0 \end{pmatrix}, B = \begin{pmatrix} C_{xx} & 0 \\ 0 & C_{yy} \end{pmatrix} \,, \tag{7.3}$$

the canonical vectors w_x and w_y can be obtained as the solution of the following eigenvalue equation [156]:

$$Aw = \lambda B w \,, \tag{7.4}$$

where λ is the eigenvalue and $w = (w_x, w_y)$. Note that the number of non-zero solution to 7.2 is d which is not greater than the smallest of p and q, i.e., $d \leq min(p, q)$.

One of the ways to solve 7.2 is Singular Value Decomposition (SVD). The canonical vectors w_x and w_y can be obtained by value decomposition of the matrix L defined as below:

$$L = C_{xx}^{-1/2} C_{xy} C_{yy}^{-1/2} \in \mathbb{R}^{p \times q} \,. \tag{7.5}$$

Let $L = UDV^T$ be the SVD of L, where $U = (u_1, u_2, ..., u_p)$ and $V = (v_1, v_2, ..., v_q)$ are the eigenvector matrices, the canonical vectors can be obtained as:

$$w_{xi} = C_{xx}^{-1/2} u_i \tag{7.6}$$

$$w_{yi} = C_{yy}^{-1/2} v_i \,. \tag{7.7}$$

Once w_x and w_y are obtained, the dimensionality reduction of the original data can be performed in the form of $X^R = W_x^T (X - \bar{X})$ and $Y^R = W_y^T (Y - \bar{Y})$, where $\bar{X}$ and $\bar{X}$ are the means of X and Y, respectively. $W_x^T = [w_{x1}, w_{x2}, ..., w_{xd}]$ and $W_y^T = [w_{y1}, w_{y2}, ..., w_{yd}]$ denote two projective matrices whose columns correspond to the first d largest common eigenvalues of 7.4. As a result, both X^R and Y^R are of size $d \times n$ respectively.

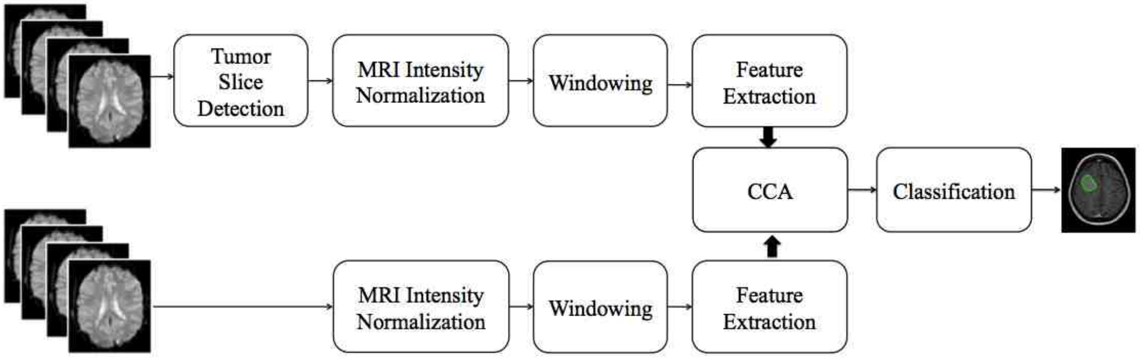

Figure 7.1: Framework of the proposed system

As defined in [153], feature-level fusion is performed either by concatenation or summation of the transformed feature vectors:

$$Z_1 = \begin{pmatrix} X^* \\ Y^* \end{pmatrix} = \begin{pmatrix} W_x^T X \\ W_y^T Y \end{pmatrix} = \begin{pmatrix} W_x & 0 \\ 0 & W_y \end{pmatrix}^T \begin{pmatrix} X \\ Y \end{pmatrix}, \tag{7.8}$$

or

$$Z_2 = X^* + Y^* = W_x^T X + W_y^T Y = \begin{pmatrix} W_x \\ W_y \end{pmatrix}^T \begin{pmatrix} X \\ Y \end{pmatrix}, \tag{7.9}$$

where Z_1 and Z_2 are called the Canonical Correlation Discriminant Features (CCDFs).

7.3 System Overview

The system overview is depicted in Fig. 7.1. The following sections provide the details about the steps shown in the framework.

7.3.1 Detection of Tumor Slices

In order to detect images containing tumors, the same method described in chapter 5 is used. The main idea is based on histogram asymmetry between the two brain hemispheres. Two brain hemispheres are separated by finding the longest diameter as the brain midline. In order to find histogram asymmetry, the mutual information between histograms of two hemispheres is calculated. If the mutual information falls below a certain threshold, the imageis recognized to contain tumor. Here, the number of slices in all sequences are equal and corresponding slices represent the image of same brain region. Owing this fact, tumor detection is applied to just one MR contrast mechanism. If one slice in one MR sequence is detected to have tumor, the corresponding slices in the other sequences are considered to have tumor as well.

7.3.2 MRI Intensity Normalization

The same methods mentioned in chapter 5 are used for MRI intensity normalization.

7.3.3 Windowing

After tumor slice detection, in order to populate the training data, random windows located all around the brain area are cropped. If the central pixel of the window falls in the tumor region, it is labeled as tumor and otherwise is labeled as healthy.

In order to populate the training set, random windows located all around the brain area are cropped. If the central pixel of the window falls in the tumor region, it is labeled as tumor and otherwise is labeled as healthy. The only difference is that for each window instance, the corresponding region in other MR sequence is also attained at the same time. In order to have corresponding regions from different MR images, the images need to be aligned. MRI registration is used to automatically align different MR sequences to a common coordinate system. One common method is using intensity-based image registration. Unlike some other techniques, it does not find features or use control points. Intensity-based registration is often well-suited for medical and remotely sensed imagery [157].

Using a window, a region of interest is cropped in corresponding sequences. That is, if an area is cropped in one MR sequence, the corresponding area in the second MR sequence is also cropped simultaneously. Therefore, for a single region of interest, we have two input images from two MR sequences. For the test step, a same size sliding window sweeps all over the brain tissue in different MR sequences and selects corresponding regions in the same way explained for the training part.

For this experiment, combination of two MR images are processed. These combinations are as following:

T1-w and T2-w,

T1-w and FLAIR,

T2-w and FLAIR.

7.3.4 Feature Aggregation

Different statistical and wavelet features are extracted from corresponding regions of interest in two MR sequences. Wavelet features are extracted using DT-CWT, AM-CWT, wavelet decomposition and wavelet packet decomposition, as described in Section 6.2.

Yl, Yh, and $Yscale$ features from Dual Tree complex wavelet transformation, are extracted where Yl is a cell array including the low-pass sub-band from the final level, Yh is a cell array containing the high-pass sub-band for each level and $Yscale$ is a cell array containing the low-pass coefficients at every scale.

Morlet-wavelet features are extracted by applying Morlet-wavelet kernels with two different scales and eight orientations.

The length of the feature vector achieved from applying 2D wavelet packet decomposition on each window is 128. In addition, using 2D wavelet transform decomposition on each window results in creating a 273 dimensional feature vector.

The total wavelet feature vector is a 2197-dimensional feature vector. In addition to wavelet features, the statistical features including 7 first-order statistical features is added to feature pool. Statistical feature vector includes 20 GLRLM features, 112 GLCM features, 80 HOG features, and 256 LBP features, which makes a 475-dimentional vector. Concatenation of statistical and wavelet features creates a 2672-dimensional feature vector.

7.3.5 Feature Fusion and Classifications

After a slice is recognized to have tumor, segmentation step is applied to segment the tumor area. The candidate tumor regions are acquired using a sliding window that sweeps through the whole brain tissue. The sliding window selects a region of interest in corresponding slices in two MR sequences. It means that for a single region of interest, we have two input images cropped from two MR sequences.

Different features are extracted from each region of interest in two MR images at the same time. After applying PCA to reduce the dimensionality of the feature vectors, CCA is employed for feature fusion. Then, the fused features are classified into either tumor or healthy using SVM classifier. Seventy percent of data are randomly chosen for training set, and the rest is used for testing. If the region of interest is classified to have tumor, the central pixel of the window is labeled as tumor. On the

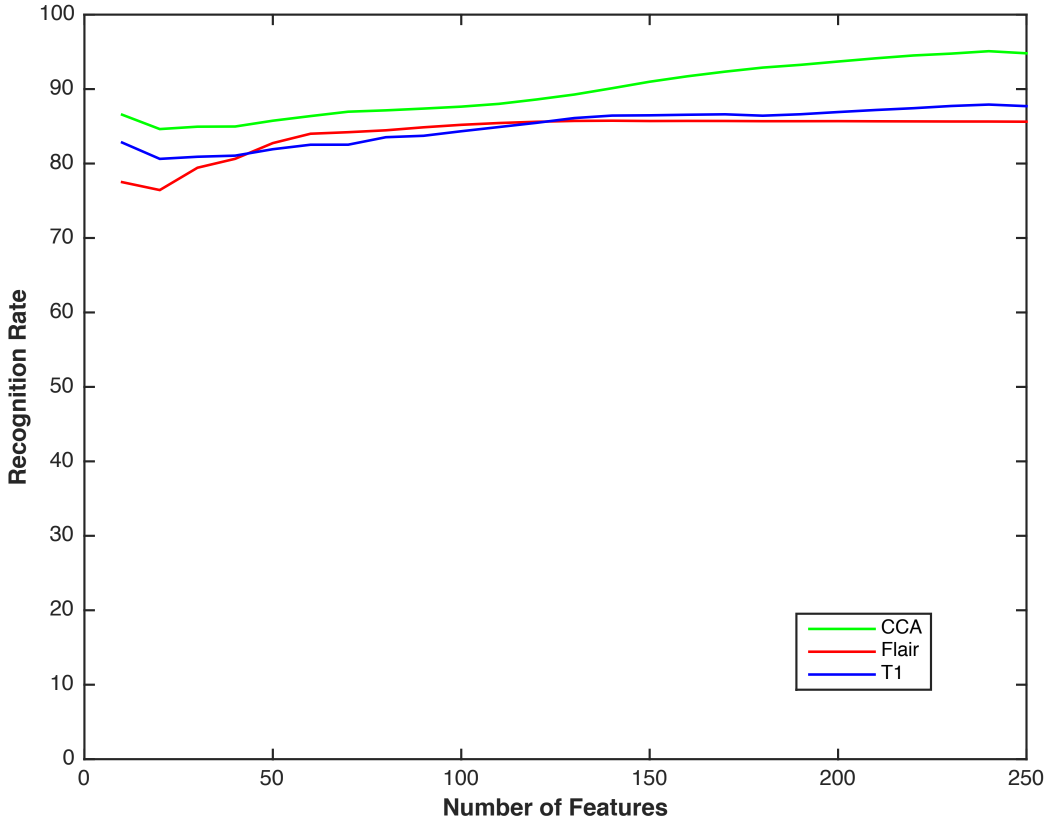

Figure 7.2: Tumor segmentation accuracy of fused T1-w and FLAIR

other hand, if it is classified as healthy, the central pixel is labeled as healthy. The classification results are depicted in Fig. 7.2, Fig. 7.3, and Fig. 7.4. It is seen that fusion of two MRI sequences using CCA outperforms the classification results of using other two MRI sequences separately, regardless of the number of features employed.

A consistency verification algorithm is used to remove the false positives and false negatives. As it was explained in 5.4.3, consistency verification algorithm is a majority filter to alter the pixel labels that are not consistent with their neighbor labels in a certain neighborhood. Here, consistency verification is applied in a 3×3 neighborhood window. Segmented lesions in two MR sequences are shown in Fig.

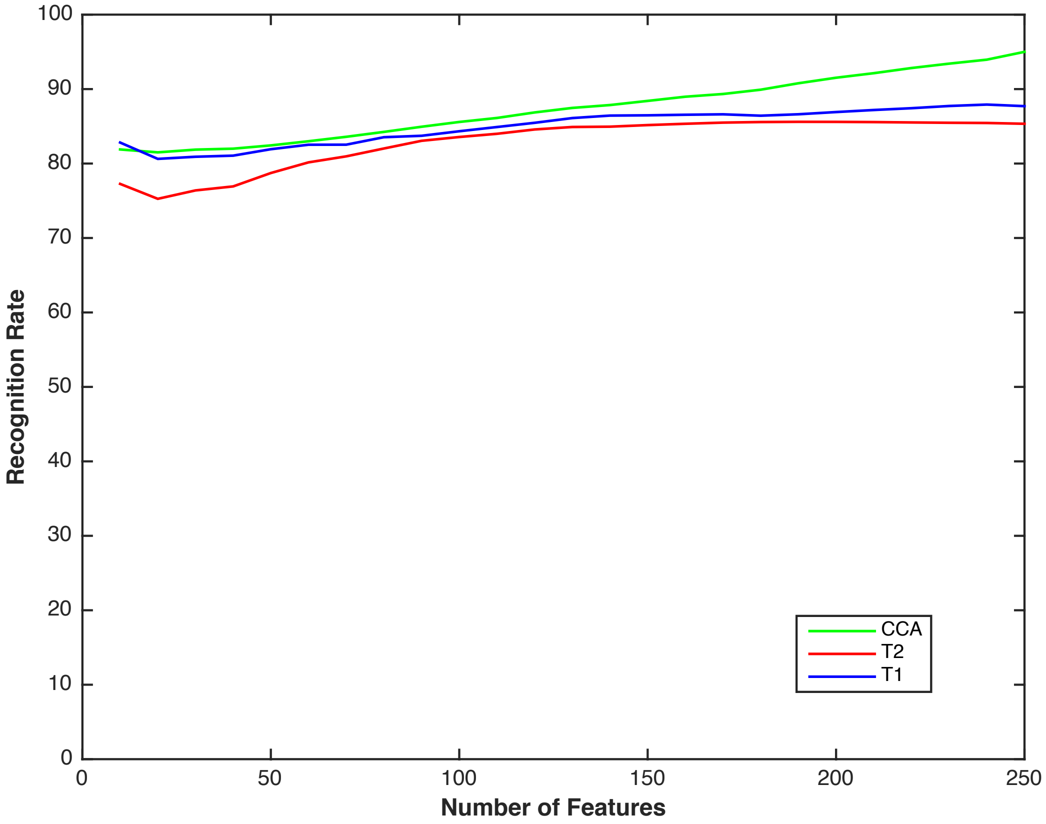

Figure 7.3: Tumor segmentation accuracy of fused T1-w and T2-w

7.5. The segmentation results achieved from current method are shown in Table 7.1. The comparison of this method and methods presented in previous chapters is shown in Table 7.2. It is seen that achieved accuracies from the current proposed method is higher than the accuracies from the proposed previous methods.

7.4 Conclusion

In order to improve tumor segmentation accuracy for real data, we have presented CCA-based approach for feature-level fusion of two MR contrast mechanisms. Using this method, we take advantage of complementary information of different MR images.

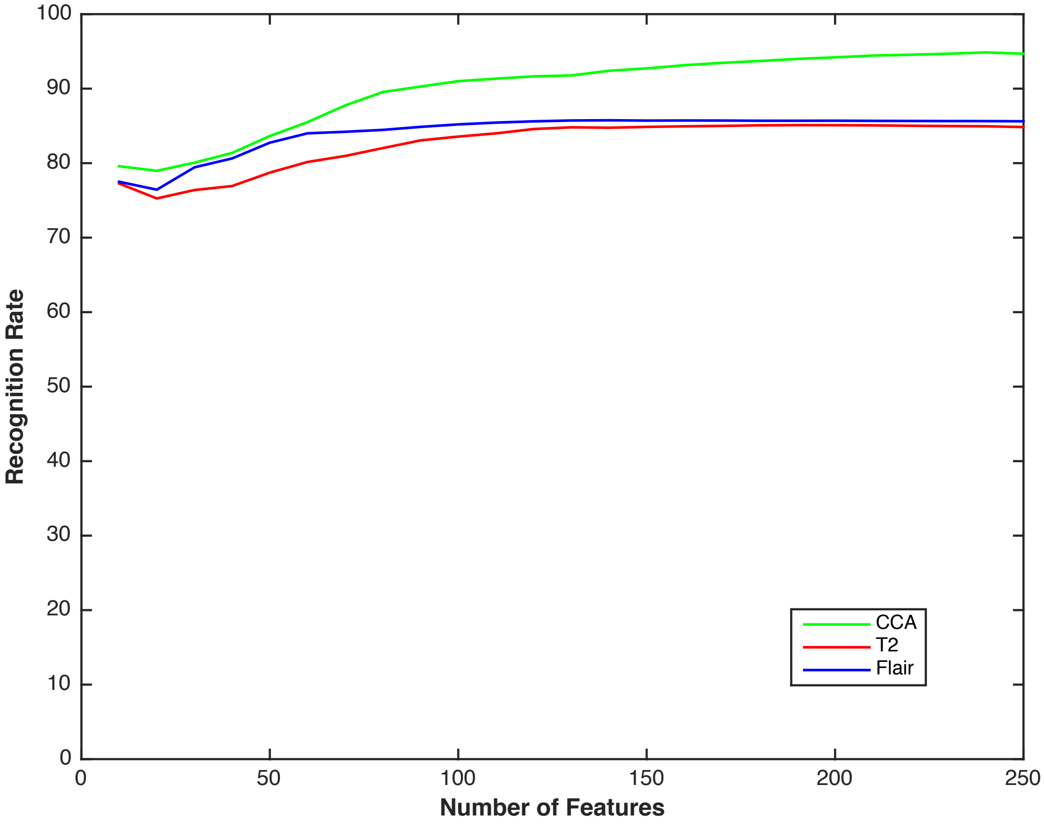

Figure 7.4: Tumor segmentation accuracy of fused T2-w and FLAIR

After registration of different MR images to make them aligned, using the method mentiond in chapter 5, the slices containing tumor are recognized. Since the number of slices in all sequences are equal and corresponding slices represent the image of same brain region, tumor detection is applied to just one MR contrast mechanism. If one slice in one MR sequence is detected to have tumor, the corresponding slices in other sequences are considered to have tumor as well.

After tumor slice detection, histogram normalization method is applied to normalize MRI intensity of MR images. In order to populate the training data, random windows located all around the brain area are cropped. If the central pixel of the

Table 7.1: Tumor segmentation accuracy using CCA method

	Real T1 and T2	Real T1 and FLAIR	Real T2 and FLAIR
Current Method	95.1 ± 0.3	95.8 ± 0.2	95.4 ± 0.4

Table 7.2: Comparing tumor segmentation accuracy using fusion method and our previous methods

	Real T1	Real FLAIR	Real T2
Method in chapter 5	92.3 ± 0.1	93.2 ± 0.3	91.7 ± 0.4
Method in chapter 6	93.4 ± 0.4	93.8 ± 0.1	92.3 ± 0.2
	Real T1 and T2	Real T1 and FLAIR	Real T2 and FLAIR
Method in chapter 7	95.1 ± 0.3	95.8 ± 0.2	95.4 ± 0.4

window falls in the tumor region, it is labeled as tumor and otherwise is labeled as healthy. Testing is applied on unseen slices using the sliding window approach presented in chapter 5. Using a window, a region of interest is cropped in corresponding brain area in two MRI contrast mechanisms simultaneously. Therefore, for a single region of interest, we have two input images, which are from two MR sequences. Different features are extracted from corresponding regions of interest in two MR sequences. In order to fuse the extracted features, canonical correlation analysis is applied. After applying CCA, the fused features are classified into either tumor or healthy using SVM. If the region of interest is classified to have tumor, the central pixel of the window is labeled as tumor. On the other hand, if it is classified as healthy, the central pixel is labeled as healthy. It is worth mentioning that for the first time CCA is applied for combining MRI sequences in order to segment tumors. Even though data fusion increases computational complexity of the segmentation algorithm, it results in higher accuracy. Therefore, it is a trade-off between the accuracy and the computational complexity, and it can be useful in the applications in which the accuracy is more important than the computational cost.

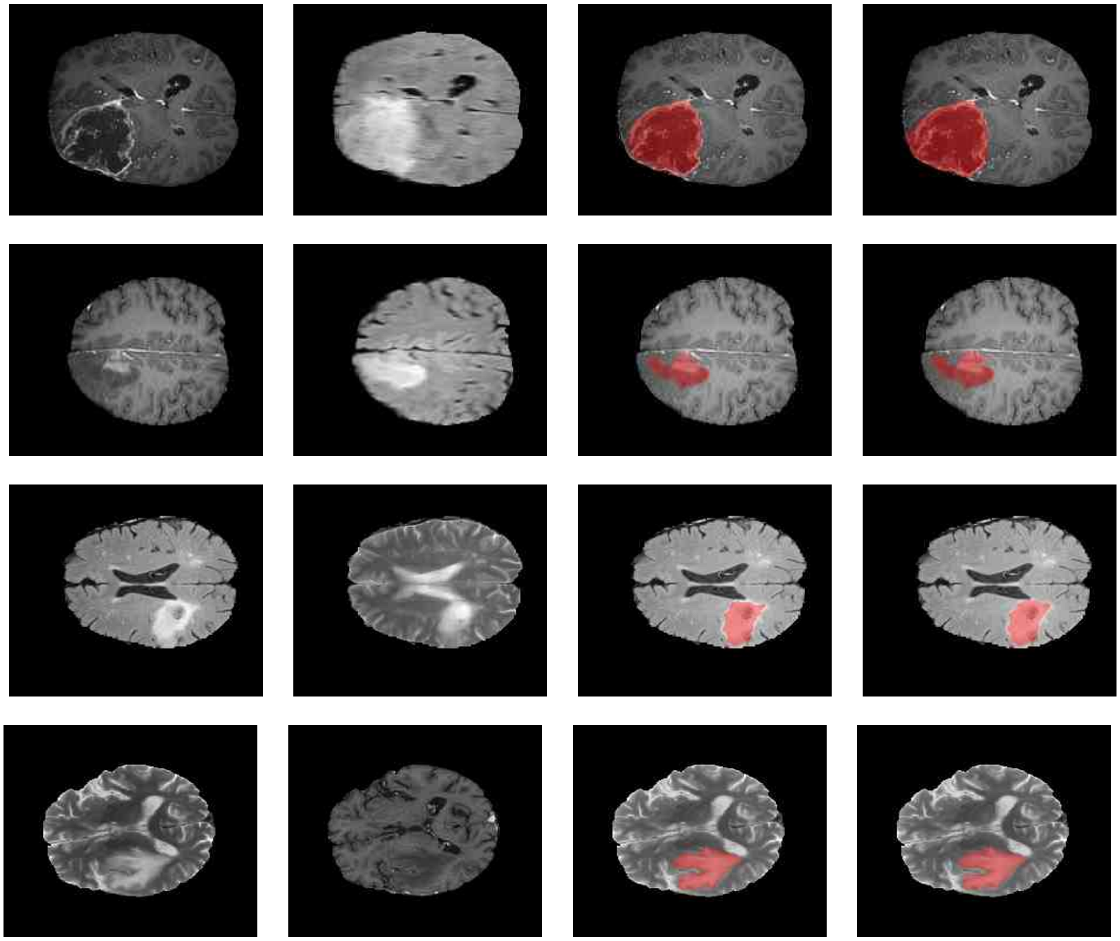

Figure 7.5: Examples of tumor lesion segmentation on database with real MR images. (first and second columns) database images, (third column) ground truth, (forth column) segmented lesion after consistency verification using current technique. In first and second row, T1 and FLAIR are fused. In third row, T2 and FLAIR are fused. In forth row, T1 and T2 are fused.

CHAPTER 8

Conclusion

Using computer vision and machine learning techniques, four methods are developed for brain lesion detection and segmentation in magnetic resonance medical images. Most of the methods discussed and reported in brain lesion segmentation field suffer from dependencies on multi-spectral MRI data, multi-scale classification, local or global registration, or high-resolution and non-noisy data. Other limitations for some methods are their high computational complexity and not being fully automated. To address the above-mentioned shortcomings, in the first stage of this study, a novel method for stroke lesion detection and segmentation in the brain MR images is proposed in **chapter 4**. The method is called the histogram-based gravitational optimization algorithm (HGOA), which is based on applying enhanced gravitational optimization algorithm on histogram analysis results using single-spectral MR images. This algorithm uses histogram-based techniques to determine the initial set of brain segments, then applies a gravitational optimization-based algorithm to reduce the number of segments, and finally uses thresholding to detect the tumor or stroke lesion.

This system is independent of atlas registration, prior anatomical knowledge, bias corrections, and multi-spectral MR images. The other advantage is in the use of single-spectral MRI. While using multi-spectral MR images address the intensity similarities between lesion and healthy tissues, it has some drawbacks and limitations. In some of practical clinical situations only one type of anatomical MR image is collected due to time and cost and patient situation limitations. In addition, use of multi-spectral data implies the need to ensure that each of the spectra must be properly registered and aligned. It is worthy of mention that the algorithm is fully automatic and computationally light as it involves the application of a single algorithm for both lesion detection and segmentation. Additionally, despite some other methods requirements to have the initial assumptions, such as a given number of tissue classes or a multi-scale classification, our algorithm does not require any such information. The experimental results on both database of synthetic and real MR images show that the proposed algorithm provides an accuracy of almost 91.5% for stroke lesions and 88% for brain tumor lesions. This compares well with the other algorithms without suffering from some of the deficiencies as stated earlier. The accuracy and computational simplicity of HGOA method make it suitable as an additional tool for the clinician. Moreover, the automated segmentation can be used to calculate the lesion volumes and track them more consistently in the treatment progress.

The major shortcoming of the proposed method is that it is incapable of detection of hardly visible lesions ($< 1cm^3$). Another shortcoming is the presence of false positives, which affects the recognition rate, especially in the tumor lesion segmentation.

For increasing tumor segmentation accuracy, an integrated automated framework, which is able to detect the MR images containing tumor lesion and segment the tumor lesion is presented in **chapter 5**. Since texture-based brain characterization has been proven to be an effective way of brain analysis, a texture-based automated approach is presented and experimented on T1-weighted, T2-weighted, and FLAIR MRI sequences. The tumor slice detection technique is based on mutual information of histograms of two brain hemispheres. The tumor segmentation technique is based on region-based and texture-based classification using a sliding window, which sweeps through the brain tissues. The remarkable accuracy of this algorithm in tumor segmentation (95.9 ± 0.4 for simulated database, and 93.2 ± 0.3 for real database) demonstrates the efficiency of the proposed method. Comparing with the previous results, higher segmentation accuracy for brain tumor lesions is achieved. Similar to the previous approach, this method is also independent of atlas registration, prior anatomical knowledge, bias corrections, and multi-spectral MRI.

As an additional study, we also compare the capability and efficacy of two different feature sets, i.e., Gabor wavelets and statistical features, in automated segmentation of brain tumor lesions in MRI images. Applying gray level co-occurrence matrix, grey level run length matrix, histogram of oriented gradient, and linear binary pattern method, second-order statistical feature vectors are derived. Adding first-order statistical features to this group, a 475-dimensional statistical feature vector is obtained. On the other hand, employing the Gabor wavelet transform, in five scale and eight orientations, an 81000-dimensional Gabor wavelet feature vector is captured. The comparison results indicate that statistical features usually offer higher accuracy than Gabor wavelet features. Moreover, statistical features have much smaller dimensionality than Gabor wavelet-based feature (475 vs. 81000). Although Gabor wavelets are employed widely in computer vision and medical image processing due to their effective directional selectivity, they occupy large amount of memory; they are highly redundant and lead to high computational costs. Even in the laboratory conditions, although the feature extraction time for both Gabor wavelet and statistical features are almost the same, the dimensionality reduction using PCA is almost eight times faster for statistical features. These observations seem to prove that statistical features are adequately enough to discriminate tumor tissues from other tissue types using MRI images.

In **chapter 6**, the system presented in chapter 5 is enhanced to accelerate the procedure, reduce the computational complexity, and increase the brain tumor segmentation accuracy. The algorithm modifications are applied in three phases as feature extraction, feature selection, and tumor localization. Fully anisotropic complex wavelet transform, dual tree complex wavelet transform, wavelet transform decomposition, and wavelet packet decomposition are employed for texture-based feature extraction of brain MR images. The anisotropic Morlet complex wavelet transform and dual-tree complex wavelet transform are applied for the first time in tumor segmentation study. These features are capable of extracting directional texture information and presenting trends, breakdown points, discontinuities in higher derivatives, and self-similarity in brain MR images. Adding these features to the existed feature pool increases the size of feature pool excessively. For defying the curse of dimensionality, a new feature selection technique based on regularized Winnow algorithm is proposed. While RWA classifier works with binary feature vectors, it is modified to not only work as a feature selection technique but also to be able to handle non-binary features.

For localizing the tumor area, a sliding window sweeps through the whole brain tissue to localize candidate tumor regions with the step size of five pixels. It decreases the calculation complexity and expedites the segmentation procedure. A tumor classification approach is then applied on every instance of the window to label the window central pixel as healthy or tumor. The obtained candidate pixels determined by this method to be as tumor lesion is used to construct the initial points for skippy greedy snake algorithm. Specifying the appropriate initial points has a great influence on the accuracy and convergence speed of the skippy greedy snakes algorithm. In addition, it obviates the requirement of human interference to manually specify initial points. This algorithm achieves more accurate segmentation results (95.9 ± 0.4 for simulated database, and 93.2 ± 0.3 for real database) with less computational cost.

Methods presented in **chapter 5** and **chapter 6** have some advantages as following: They are independent of atlas registration, prior anatomical knowledge, or bias corrections that restrict the general application of many state-of-the-art methods. Reliance on atlas registration in other algorithms implies that their accuracy is dependent on how well the atlas is constructed and how well the registration algorithm can register the test data to the atlas. Prior anatomical knowledge dependence implies that such algorithms must be trained to incorporate such information, which can lead to error. The need for bias correction in many other algorithms also introduces errors into the data to be analyzed, and therefore adds inaccuracy and difficulties with consistency of the final results. The other contribution is in the use of single-spectral MRI. Due to registration requirement of multi-spectral MRI study, failure to do the registration can result in misalignment of suspected lesions in the different spectra. Additionally, despite some other methods requirements to have the initial assumptions, such as a given number of tissue classes or a multi-scale classification, the algorithms do not require any such information. And finally, these methods are fully automatic.

In order to improve tumor segmentation accuracy in the database of real MR images, we have presented a canonical correlation analysis-based approach for feature-level fusion of two MR contrast mechanisms in **chapter 7**. Using this method, we take advantage of complementary information of two MR sequences. After registration of different MR images to make them aligned, using the method mentioned in chapter 5, the slices containing tumor are recognized. In order to populate the training data, random windows located all around the brain area are cropped. If the majority of pixels of the window fall in the tumor region, the window is labeled as tumor and otherwise is labeled as healthy. Testing is applied on unseen slices using the sliding window approach presented in chapter 5. In this case of multiple sequences, the window selects a region of interest in corresponding sequences simultaneously. That is, for a single region of interest, there are two input images from two MR sequences. Feature vectors are extracted from corresponding regions of interest in both sequences. In order to fuse the extracted features, canonical correlation analysis is applied. The fused feature vectors are fed into a support vector machines classifier and all the pixels in the brain area are labeled either healthy or tumor. Consistency verification as a post-processing is applied on the labeled image to remove false positives and false negatives. The accuracy of the proposed algorithm is calculated by comparing the resulting label image with the golden label provided by the database.

It is worth mentioning that for the first time CCA is applied for combining information extracted from MRI sequences in order to segment tumors. Even though data fusion increases computational complexity of the segmentation algorithm, it results in higher accuracy. The segmentation accuracy of 95.8 ± 0.2 is achieved for the database of real MR images.

As future work, we will focus on enhancing the performance of the method in case of very small lesions can be focused. Moreover, working on reduction of false positives, beyond the use of the consistency verification algorithm can be considered. The capability of the proposed method in detection of other type of brain lesion such as lesions caused by injury and dementia can also be evaluated.

Bibliography

[1] B. S. Aghazadeh, S. Ansari, R. Pidaparti, and K. Najarian, "Non-Invasive Estimation of Intracranial Pressure in Traumatic Brain Injury Using Fully-Anisotropic Morlet Wavelet Transform and Support Vector Regression," *Biomedical Engineering Letters*, vol. 3, no. 3, pp. 190–197, 2013.

[2] N. Kingsbury, "Complex Wavelets for Shift Invariant Analysis and Filtering of Signals," *Applied and Computational Harmonic Analysis*, vol. 10, no. 3, pp. 234–253, 2001.

[3] M. Sakalli, K.-M. Lam, and H. Yan, "A Faster Converging Snake Algorithm to Locate Object Boundaries," *IEEE Transactions on Image Processing*, vol. 15, no. 5, pp. 1182–1191, 2006.

[4] A. Kharrat, N. Benamrane, M. Ben Messaoud, and M. Abid, "Detection of Brain Tumor in Medical Images," in *Signals, Circuits and Systems*. IEEE, 2009, pp. 1–6.

[5] K.-m. Lee and W. N. Street, "Dynamic Leaning of Shape for Automatic Object Recognition," in *17th ICML-2000 Workshop*.

[6] http://www.cbtrus.org/2012-NPCR-SEER/CBTRUS_Report_2004-2008_3-23-2012.pdf, accessed: 2014-10-28.

[7] http://www.strokeassociation.org/STROKEORG/AboutStroke/Impact-of-Stroke-Stroke-statistics_UCM_310728_Article.jsp, accessed: 2014-10-18.

[8] A. W. Toga, P. M. Thompson, M. S. Mega, K. L. Narr, and R. E. Blanton, "Probabilistic Approaches for Atlasing Normal and Disease-Specific Brain Variability," *Anatomy and Embryology*, vol. 204, no. 4, pp. 267–282, 2001.

[9] S. Shen, A. J. Szameitat, and A. Sterr, "Detection of Infarct Lesions from Single MRI Modality Using Inconsistency Between Voxel Intensity and Spatial Location: a 3-D Automatic Approach," *IEEE Transactions on Information Technology in Biomedicine*, vol. 12, no. 4, pp. 532–540, 2008.

[10] D. Mortazavi, A. Z. Kouzani, and H. Soltanian-Zadeh, “Segmentation of Multiple Sclerosis Lesions in MR Images: A Review,” *Neuroradiology*, vol. 54, no. 4, pp. 299–320, 2012.

[11] S. Shen, W. Sandham, M. Granat, and A. Sterr, “MRI Fuzzy Segmentation of Brain Tissue Using Neighborhood Attraction with Neural Network Optimization,” *IEEE Transactions on Information Technology in Biomedicine*, vol. 9, no. 3, pp. 459–467, 2005.

[12] Y. Kabir, M. Dojat, B. Scherrer, F. Forbes, and C. Garbay, “Multimodal MRI Segmentation of Ischemic Stroke Lesions,” in *Engineering in Medicine and Biology Society*. IEEE, 2007, pp. 1595–1598.

[13] J. A. Fiez, H. Damasio, and T. J. Grabowski, “Lesion Segmentation and Manual Warping to a Reference Brain: Intra-and Interobserver Reliability,” *Human Brain Mapping*, vol. 9, no. 4, pp. 192–211, 2000.

[14] L. Lemieux, G. Hagemann, K. Krakow, and F. G. Woermann, “Fast, Accurate, and Reproducible Automatic Segmentation of the Brain in T1-Weighted Volume MRI Data,” *Magnetic Resonance in Medicine*, vol. 42, no. 1, pp. 127–135, 1999.

[15] H. Tang, E. Wu, Q. Ma, D. Gallagher, G. Perera, and T. Zhuang, “MRI Brain Image Segmentation by Multi-Resolution Edge Detection and Region Selection,” *Computerized Medical Imaging and Graphics*, vol. 24, no. 6, pp. 349–357, 2000.

[16] A.-C. Liew and H. Yan, “An Adaptive Spatial Fuzzy Clustering Algorithm for 3-D MR Image Segmentation,” *IEEE Transactions on Medical Imaging*, vol. 22, no. 9, pp. 1063–1075, 2003.

[17] K. Van Leemput, F. Maes, D. Vandermeulen, and P. Suetens, “Automated Model-Based Tissue Classification of MR Images of the Brain,” *IEEE Transactions on Medical Imaging*, vol. 18, no. 10, pp. 897–908, 1999.

[18] D. L. Pham and J. L. Prince, “Adaptive Fuzzy Segmentation of Magnetic Resonance Images,” *IEEE Transactions on Medical Imaging*, vol. 18, no. 9, pp. 737–752, 1999.

[19] D.-Q. Zhang and S.-C. Chen, “A Novel Kernelized Fuzzy C-Means Algorithm with Application in Medical Image Segmentation,” *Artificial Intelligence in Medicine*, vol. 32, no. 1, pp. 37–50, 2004.

[20] M. C. Clark, L. O. Hall, D. B. Goldgof, R. Velthuizen, F. R. Murtagh, and M. S. Silbiger, “Automatic Tumor Segmentation Using Knowledge-Based Techniques,” *IEEE Transactions on Medical Imaging*, vol. 17, no. 2, pp. 187–201, 1998.

[21] P. Anbeek, K. L. Vincken, G. S. Van Bochove, M. J. Van Osch, and J. van der Grond, "Probabilistic Segmentation of Brain Tissue in MR Imaging," *Neuroimage*, vol. 27, no. 4, pp. 795–804, 2005.

[22] B. R. Sajja, S. Datta, R. He, M. Mehta, R. K. Gupta, J. S. Wolinsky, and P. A. Narayana, "Unified Approach for Multiple Sclerosis Lesion Segmentation on Brain MRI," *Annals of Biomedical Engineering*, vol. 34, no. 1, pp. 142–151, 2006.

[23] S. Datta, B. R. Sajja, R. He, J. S. Wolinsky, R. K. Gupta, and P. A. Narayana, "Segmentation and Quantification of Black Holes in Multiple Sclerosis," *Neuroimage*, vol. 29, no. 2, pp. 467–474, 2006.

[24] K. Van Leemput, F. Maes, D. Vandermeulen, A. Colchester, and P. Suetens, "Automated Segmentation of Multiple Sclerosis Lesions by Model Outlier Detection," *IEEE Transactions on Medical Imaging*, vol. 20, no. 8, pp. 677–688, 2001.

[25] F. B. Mohamed, S. Vinitski, C. F. Gonzalez, S. H. Faro, F. A. Lublin, R. Knobler, and J. E. Gutierrez, "Increased Differentiation of Intracranial White Matter Lesions by Multispectral 3D-Tissue Segmentation: Preliminary Results," *Magnetic Resonance Imaging*, vol. 19, no. 2, pp. 207–218, 2001.

[26] A. Achiron, S. Gicquel, S. Miron, and M. Faibel, "Brain MRI Lesion Load Quantification in Multiple Sclerosis: A Comparison Between Automated Multispectral and Semi-Automated Thresholding Computer-Assisted Techniques," *Magnetic Resonance Imaging*, vol. 20, no. 10, pp. 713–720, 2002.

[27] B. Alfano, A. Brunetti, M. Larobina, M. Quarantelli, E. Tedeschi, A. Ciarmiello, E. M. Covelli, and M. Salvatore, "Automated Segmentation and Measurement of Global White Matter Lesion Volume in Patients with Multiple Sclerosis," *Journal of Magnetic Resonance Imaging*, vol. 12, no. 6, pp. 799–807, 2000.

[28] A. P. Zijdenbos, B. M. Dawant, R. A. Margolin, and A. C. Palmer, "Morphometric Analysis of White Matter Lesions in MR Images: Method and Validation," *IEEE Transactions on Medical Imaging*, vol. 13, no. 4, pp. 716–724, 1994.

[29] J. K. Udupa, L. Wei, S. Samarasekera, Y. Miki, M. A. van Buchem, and R. I. Grossman, "Multiple Sclerosis Lesion Quantification Using Fuzzy-Connectedness Principles," *IEEE Transactions on Medical Imaging*, vol. 16, no. 5, pp. 598–609, 1997.

[30] N. Zhang, S. Ruan, S. Lebonvallet, Q. Liao, and Y. Zhu, "Kernel Feature Selection to Fuse Multi-Spectral MRI Images for Brain Tumor Segmentation," *Computer Vision and Image Understanding*, vol. 115, no. 2, pp. 256–269, 2011.

[31] Y.-T. Hsiao, C.-L. Chuang, J.-A. Jiang, and C.-C. Chien, "A Novel Optimization Algorithm: Space Gravitational Optimization," in *Systems, Man and Cybernetics*, vol. 3. IEEE, 2005, pp. 2323–2328.

[32] M. J. Lyons, J. Budynek, A. Plante, and S. Akamatsu, "Classifying Facial Attributes Using a 2-D Gabor Wavelet Representation and Discriminant Analysis," in *Automatic Face and Gesture Recognition.* IEEE, 2000, pp. 202–207.

[33] P. Yang, S. Shan, W. Gao, S. Z. Li, and D. Zhang, "Face Recognition Using Ada-Boosted Gabor Features," in *Automatic Face and Gesture Recognition.* IEEE, 2004, pp. 356–361.

[34] S. B. Antel, D. L. Collins, N. Bernasconi, F. Andermann, R. Shinghal, R. E. Kearney, D. L. Arnold, and A. Bernasconi, "Automated Detection of Focal Cortical Dysplasia Lesions Using Computational Models of Their MRI Characteristics and Texture Analysis," *Neuroimage*, vol. 19, no. 4, pp. 1748–1759, 2003.

[35] A. Zizzari, U. Seiffert, B. Michaelis, G. Gademann, and S. Swiderski, "Detection of Tumor in Digital Images of the Brain," *JIP*, vol. 2, p. 1, 2001.

[36] G. Castellano, L. Bonilha, L. Li, and F. Cendes, "Texture Analysis of Medical Images," *Clinical Radiology*, vol. 59, no. 12, pp. 1061–1069, 2004.

[37] R. Lerski, K. Straughan, L. Schad, D. Boyce, S. Blüml, and I. Zuna, "VIII. MR Image Texture AnalysisAn Approach to Tissue Characterization," *Magnetic Resonance Imaging*, vol. 11, no. 6, pp. 873–887, 1993.

[38] C. Dwith, V. Angoth, and A. Singh, "Wavelet Based Image Fusion for Detection of Brain Tumor," *International Journal of Image, Graphics and Signal Processing*, vol. 5, no. 1, p. 25, 2013.

[39] B. A. Abdullah, "Segmentation of Multiple Sclerosis Lesions in Brain MRI," 2012.

[40] D. Miller, R. Grossman, S. Reingold, and H. McFarland, "The Role of Magnetic Resonance Techniques in Understanding and Managing Multiple Sclerosis." *Brain*, vol. 121, no. 1, pp. 3–24, 1998.

[41] M. H. Levitt and R. Freeman, "Nmr Population Inversion Using a Composite Pulse," *Journal of Magnetic Resonance*, vol. 33, no. 2, pp. 473–476, 1979.

[42] D. Wicks, P. Tofts, D. Miller, G. de Boulay, A. Feinstein, R. Sacares, I. Harvey, R. Brenner, and W. McDonald, "Volume Measurement of Multiple Sclerosis Lesions with Magnetic Resonance Images," *Neuroradiology*, vol. 34, no. 6, pp. 475–479, 1992.

[43] D. Goldberg-Zimring, A. Achiron, S. Miron, M. Faibel, and H. Azhari, "Automated Detection and Characterization of Multiple Sclerosis Lesions in Brain MR Images," *Magnetic Resonance Imaging*, vol. 16, no. 3, pp. 311–318, 1998.

[44] L. Wang, H. Lai, G. J. Barker, D. H. Miller, P. S. Tofts *et al.*, "Correction for Variations in MRI Scanner Sensitivity in Brain Studies with Histogram Matching," *Magnetic Resonance in Medicine*, vol. 39, no. 2, pp. 322–327, 1998.

[45] C. Pachai, Y. Zhu, J. Grimaud, M. Hermier, A. Dromigny-Badin, A. Boudraa, G. Gimenez, C. Confavreux, and J. Froment, "A Pyramidal Approach for Automatic Segmentation of Multiple Sclerosis Lesions in Brain MRI," *Computerized Medical Imaging and Graphics*, vol. 22, no. 5, pp. 399–408, 1998.

[46] P. Anbeek, K. L. Vincken, M. J. van Osch, R. H. Bisschops, and J. van der Grond, "Automatic Segmentation of Different-Sized White Matter Lesions by Voxel Probability Estimation," *Medical Image Analysis*, vol. 8, no. 3, pp. 205–215, 2004.

[47] ——, "Probabilistic Segmentation of White Matter Lesions in MR Imaging," *NeuroImage*, vol. 21, no. 3, pp. 1037–1044, 2004.

[48] M. Kamber, R. Shinghal, D. L. Collins, G. S. Francis, and A. C. Evans, "Model-Based 3-D Segmentation of Multiple Sclerosis Lesions in Magnetic Resonance Brain Images," *IEEE Transactions on Medical Imaging*, vol. 14, no. 3, pp. 442–453, 1995.

[49] A. Zijdenbos, R. Forghani, and A. Evans, "Automatic Quantification of MS Lesions in 3D MRI Brain Data Sets: Validation of INSECT," in *Medical Image Computing and Computer-Assisted Intervention.* Springer, 1998, pp. 439–448.

[50] S. K. Warfield, K. H. Zou, and W. M. Wells, "Simultaneous truth and performance level estimation (STAPLE): an algorithm for the validation of image segmentation," *IEEE Transactions on Medical Imaging*, vol. 23, no. 7, pp. 903–921, 2004.

[51] S. K. Warfield, M. Kaus, F. A. Jolesz, and R. Kikinis, "Adaptive, template moderated, spatially varying statistical classification," *Medical Image Analysis*, vol. 4, no. 1, pp. 43–55, 2000.

[52] O. Freifeld, H. Greenspan, and J. Goldberger, "Multiple Sclerosis Lesion Detection Using Constrained GMM and Curve Evolution," *Journal of Biomedical Imaging*, vol. 2009, p. 14, 2009.

[53] W. M. Wells III, W. E. L. Grimson, R. Kikinis, and F. A. Jolesz, "Adaptive Segmentation of MRI Data," *IEEE Transactions on Medical Imaging*, vol. 15, no. 4, pp. 429–442, 1996.

[54] B. H. Menze, K. Van Leemput, D. Lashkari, M.-A. Weber, N. Ayache, and P. Golland, "A Generative Model for Brain Tumor Segmentation in Multi-Modal Images," in *Medical Image Computing and Computer-Assisted Intervention.* Springer, 2010, pp. 151–159.

[55] S. Ruan, S. Lebonvallet, A. Merabet, and J. Constans, "Tumor Segmentation from a Multispectral MRI Images by Using Support Vector Machine Classification," in *4th IEEE International Symposium on Biomedical Imaging.* IEEE, 2007, pp. 1236–1239.

[56] Z. Lao, D. Shen, D. Liu, A. F. Jawad, E. R. Melhem, L. J. Launer, R. N. Bryan, and C. Davatzikos, "Computer Assisted Segmentation of White Matter Lesions in 3D MR Images Using Support Vector Machine," *Academic Radiology*, vol. 15, no. 3, pp. 300–313, 2008.

[57] T. Chen and D. Metaxas, "Gibbs Prior Models, Marching Cubes, and Deformable Models: A Hybrid Framework for 3D Medical Image Segmentation," in *Medical Image Computing and Computer-Assisted Intervention.* Springer, 2003, pp. 703–710.

[58] C.-H. Lee, M. Schmidt, A. Murtha, A. Bistritz, J. Sander, and R. Greiner, "Segmenting Brain Tumors with Conditional Random Fields and Support Vector Machines," in *Computer Vision for Biomedical Image Applications.* Springer, 2005, pp. 469–478.

[59] N. Zhang, S. Ruan, S. Lebonvallet, Q. Liao, and Y. Zhu, "Multi-Kernel SVM Based Classification for Brain Tumor Segmentation of MRI Multi-Sequence," in *ICIP.* IEEE, 2009, pp. 3373–3376.

[60] F. Admasu, S. Al-Zubi, K. Toennies, N. Bodammer, and H. Hinrichs, "Segmentation of Multiple Sclerosis Lesions from MR Brain Images Using the Principles of Fuzzy-Connectedness and Artificial Neuron Networks," in *International Conference on Image Processing*, vol. 2. IEEE, 2003, pp. II–1081.

[61] X. Li, S. Bhide, and M. Kabuka, "Labeling of MR Brain Images Using Boolean Neural Network," *IEEE Transactions on Medical Imaging*, vol. 15, no. 5, pp. 628–638, 1996.

[62] E. Kischell, N. Kehtarnavaz, G. Hillman, H. Levin, M. Lilly, and T. Kent, "Classification of Brain Compartments and Head Injury Lesions by Neural Networks Applied to MRI," *Neuroradiology*, vol. 37, no. 7, pp. 535–541, 1995.

[63] M. Ozkan, B. M. Dawant, and R. J. Maciunas, "Neural-Network-Based Segmentation of Multi-Modal Medical Images: A Comparative and Prospective Study," *IEEE Transactions on Medical Imaging*, vol. 12, no. 3, pp. 534–544, 1993.

[64] G. R. Hillman, C.-W. Chang, H. Ying, T. A. Kent, and J. Yen, "Automatic System for Brain MRI Analysis Using a Novel Combination of Fuzzy Rule-Based and Automatic Clustering Techniques," in *Medical Imaging.* International Society for Optics and Photonics, 1995, pp. 16–25.

[65] A. Namasivayam and L. O. Hall, "Integrating Fuzzy Rules into the Fast, Robust Segmentation of Magnetic Resonance Images," in *Biennial Conference of Fuzzy Information.* IEEE, 1996, pp. 23–27.

[66] W. Menhardt and K.-H. Schmidt, "Computer Vision on Magnetic Resonance Images," *Pattern Recognition Letters*, vol. 8, no. 2, pp. 73–85, 1988.

[67] S. Dellepiane, G. Venturi, and G. Vernazza, "A fuzzy model for the processing and recognition of MR pathological images," in *Information Processing in Medical Imaging.* Springer, 1991, pp. 444–457.

[68] D. N. Metaxas, Z. Qian, X. Huang, R. Huang, T. Chen, and L. Axel, "Hybrid Deformable Models for Medical Segmentation and Registration," in *Control, Automation, Robotics and Vision.* IEEE, 2006, pp. 1–6.

[69] H. Cai, R. Verma, Y. Ou, S.-k. Lee, E. R. Melhem, and C. Davatzikos, "Probabilistic Segmentation of Brain Tumors Based on Multi-Modality Magnetic Resonance Images," in *Biomedical Imaging: From Nano to Macro.* IEEE, 2007, pp. 600–603.

[70] M. B. Cuadra, C. Pollo, A. Bardera, O. Cuisenaire, J.-G. Villemure, and J. Thiran, "Atlas-Based Segmentation of Pathological MR Brain Images Using a Model of Lesion Growth," *IEEE Transactions on Medical Imaging*, vol. 23, no. 10, pp. 1301–1314, 2004.

[71] F. Yang, T. Jiang, W. Zhu, and F. Kruggel, "White Matter Lesion Segmentation from Volumetric MR Images," in *Medical Imaging and Augmented Reality.* Springer, 2004, pp. 113–120.

[72] K. B. Prakash, V. Gupta, H. Jianbo, and W. L. Nowinski, "Automatic Processing of Diffusion-Weighted Ischemic Stroke Images Based on Divergence Measures: Slice and Hemisphere Identification, and Stroke Region Segmentation," *International Journal of Computer Assisted Radiology and Surgery*, vol. 3, no. 6, pp. 559–570, 2008.

[73] E. A. Stamatakis and L. K. Tyler, "Identifying Lesions on Structural Brain Images Validation of the Method and Application to Neuropsychological Patients," *Brain and Language*, vol. 94, no. 2, pp. 167–177, 2005.

[74] S. Srivastava, F. Maes, D. Vandermeulen, W. V. Paesschen, P. Dupont, and P. Suetens, "Feature-Based Statistical Analysis of Structural MR Data for Automatic Detection of Focal Cortical Dysplastic Lesions," *NeuroImage*, vol. 27, no. 2, pp. 253–266, 2005.

[75] H. Khotanlou, O. Colliot, and I. Bloch, “Automatic Brain Tumor Segmentation Using Symmetry Analysis and Deformable Models,” in *International Conference on Advances in Pattern Recognition ICAPR*, 2007, pp. 198–202.

[76] J. J. Corso, E. Sharon, S. Dube, S. El-Saden, U. Sinha, and A. Yuille, “Efficient Multilevel Brain Tumor Segmentation with Integrated Bayesian Model Classification,” *IEEE Transactions on Medical Imaging*, vol. 27, no. 5, pp. 629–640, 2008.

[77] W. Dou, S. Ruan, Y. Chen, D. Bloyet, and J.-M. Constans, “A Framework of Fuzzy Information Fusion for the Segmentation of Brain Tumor Tissues on MR Images,” *Image and vision Computing*, vol. 25, no. 2, pp. 164–171, 2007.

[78] M. Prastawa, E. Bullitt, S. Ho, and G. Gerig, “A Brain Tumor Segmentation Framework Based on Outlier Detection,” *Medical Image Analysis*, vol. 8, no. 3, pp. 275–283, 2004.

[79] D. N. Kennedy, C. Haselgrove, N. Makris, D. M. Goldin, M. H. Lev, D. Caplan, and V. S. Caviness, “WebParc: a Tool for Analysis of the Topography and Volume of Stroke from MRI,” *Medical & Biological Engineering & Computing*, vol. 48, no. 3, pp. 215–228, 2010.

[80] Y.-H. Mah, R. Jager, C. Kennard, M. Husain, and P. Nachev, “A New Method for Automated High-Dimensional Lesion Segmentation Evaluated in Vascular Injury and Applied to the Human Occipital Lobe,” *Cortex*, 2012.

[81] S. Mujumdar, R. Varma, and L. Kishore, “A Novel Framework for Segmentation of Stroke Lesions in Diffusion Weighted MRI Using Multiple b-Value Data,” in *Pattern Recognition.* IEEE, 2012, pp. 3762–3765.

[82] N. Hevia Montiel, C. Rosso, N. Chupin, S. Deltour, E. Bardinet, D. Dormont, Y. Samson, and S. Baillet, “Automatic Prediction of Infarct Growth in Acute Ischemic Stroke from MR Apparent Diffusion Coefficient Maps,” *Academic Radiology*, vol. 15, no. 1, pp. 77–83, 2008.

[83] S. Shen, A. J. Szameitat, and A. Sterr, “VBM Lesion Detection Depends on the Normalization Template: a Study Using Simulated Atrophy,” *Magnetic Resonance Imaging*, vol. 25, no. 10, pp. 1385–1396, 2007.

[84] W. Li, J. Tian, E. Li, and J. Dai, “Robust Unsupervised Segmentation of Infarct Lesion from Diffusion Tensor MR Images Using Multiscale Statistical Classification and Partial Volume Voxel Reclassification,” *NeuroImage*, vol. 23, no. 4, pp. 1507–1518, 2004.

[85] M. A. Jacobs, P. Mitsias, H. Soltanian-Zadeh, S. Santhakumar, A. Ghanei, R. Hammond, D. J. Peck, M. Chopp, and S. Patel, “Multiparametric MRI Tissue Characterization in Clinical Stroke With Correlation to Clinical Outcome Part 2,” *Stroke*, vol. 32, no. 4, pp. 950–957, 2001.

[86] H. Soltanian-Zadeh, P. Mitsias, M. Khalighi, M. Lu, H. Ebadian, J. Ewing, Q. Zhao, S. Patel, and M. Chopp, "Relationships among ISODATA, DWI, MTT, and T2 Lesions in Stroke," in *Proc. Intl. Soc. Mag. Reson. Med*, vol. 11, 2003, p. 2245.

[87] A. L. Martel, S. J. Allder, G. S. Delay, P. S. Morgan, and A. R. Moody, "Measurement of Infarct Volume in Stroke Patients Using Adaptive Segmentation of Diffusion Weighted MR Images," in *Medical Image Computing and Computer-Assisted Intervention–MICCAI99*. Springer, 1999, pp. 22–31.

[88] Y. Han, E. Li, J. Tian, J. Chen, H. Wang, and J. Dai, "The Application of Diffusion-and Perfusion-Weighted Magnetic Resonance Imaging in the Diagnosis and Therapy of Acute Cerebral Infarction," *International journal of Biomedical Imaging*, vol. 2006, 2006.

[89] S. Mujumdar, "Detection and Segmentation of Stroke Lesions from Diffusion Weighted MRI Data of the Brain," Ph.D. dissertation, International Institute of Information Technology Hyderabad, 2013.

[90] http://www.strokeassociation.com.au/, accessed: 2014-10-28.

[91] N. Nabizadeh, N. John, and C. Wright, "Histogram-Based Gravitational Optimization Algorithm on Single MR Modality for Automatic Brain Lesion Detection and Segmentation," *Expert Systems with Applications*, 2014.

[92] R. C. Gonzales and R. E. Woods, "Digital Image Processing, 2-nd Edition," 2002.

[93] E. M. Haacke, R. W. Brown, M. R. Thompson, and R. Venkatesan, "Magnetic Resonance Imaging," *Physical Principles and Sequence Design*, 1999.

[94] H. Li, B. Manjunath, and S. K. Mitra, "Multisensor Image Fusion Using the Wavelet Transform," *Graphical Models and Image Processing*, vol. 57, no. 3, pp. 235–245, 1995.

[95] M. B. A. Haghighat, A. Aghagolzadeh, and H. Seyedarabi, "Multi-Focus Image Fusion for Visual Sensor Networks in DCT Domain," *Computers & Electrical Engineering*, vol. 37, no. 5, pp. 789–797, 2011.

[96] M. Jacobs, S. Patel, P. Mitsias, H. Soltanian-Zadeh, D. Peck, and A. Ghanei, "Unsupervised Segmentation of Clinical Stroke with Multiparameter MRI," in *Proc. Intl. Soc. Mag. Reson. Med*, vol. 8, 2000, p. 669.

[97] S. Ahmed, K. M. Iftekharuddin, and A. Vossough, "Efficacy of Texture, Shape, and Intensity Feature Fusion for Posterior-Fossa Tumor Segmentation in MRI," *IEEE Transactions on Information Technology in Biomedicine*, vol. 15, no. 2, pp. 206–213, 2011.

[98] Y.-h. Liu, M. Muftah, T. Das, L. Bai, K. Robson, and D. Auer, "Classification of MR Tumor Images Based on Gabor Wavelet Analysis," *Journal of Medical and Biological Engineering*, vol. 32, no. 1, pp. 22–28, 2012.

[99] S. Ghanavati, J. Li, T. Liu, P. S. Babyn, W. Doda, and G. Lampropoulos, "Automatic Brain Tumor Detection in Magnetic Resonance Images," in *9th IEEE International Symposium on Biomedical Imaging (ISBI).* IEEE, 2012, pp. 574–577.

[100] G. Mirajkar and B. Barbadekar, "Automatic Segmentation of Brain Tumors from MR Images Using Undecimated Wavelet Transform and Gabor Wavelets," in *2010 17th IEEE International Conference on Electronics, Circuits, and Systems.* IEEE, 2010, pp. 702–705.

[101] E. I. Zacharaki, S. Wang, S. Chawla, D. Soo Yoo, R. Wolf, E. R. Melhem, and C. Davatzikos, "Classification of Brain Tumor Type and Grade Using MRI Texture and Shape in a Machine Learning Scheme," *Magnetic Resonance in Medicine*, vol. 62, no. 6, pp. 1609–1618, 2009.

[102] G. L. Qurat-Ul-Ain, S. B. Kazmi, M. A. Jaffar, and A. M. Mirza, "Classification and Segmentation of Brain Tumor Using Texture Analysis," *Recent Advances in Artificial Intelligence, Knowledge Engineering and Data Bases*, pp. 147–155, 2010.

[103] X. Xuan and Q. Liao, "Statistical Structure Analysis in MRI Brain Tumor Segmentation," in *Image and Graphics.* IEEE, 2007, pp. 421–426.

[104] G. Srinivasan and G. Shobha, "Statistical Texture Analysis," in *Proceedings of World Academy of Science, Engineering and Technology*, vol. 36, 2008, pp. 1264–1269.

[105] J. Sklansky, "Image Segmentation and Feature Extraction," *IEEE Transactions on Systems, Man and Cybernetics*, vol. 8, no. 4, pp. 237–247, 1978.

[106] W.-Y. Ma and B. S. Manjunath, "Texture Features and Learning Similarity," in *IEEE Computer Society Conference on Computer Vision and Pattern Recognition.* IEEE, 1996, pp. 425–430.

[107] T. Ojala, M. Pietikäinen, and D. Harwood, "A Comparative Study of Texture Measures with Classification Based on Featured Distributions," *Pattern Recognition*, vol. 29, no. 1, pp. 51–59, 1996.

[108] W. Chen, R. Smith, N. Nabizadeh, K. Ward, C. Cockrell, J. Ha, and K. Najarian, "Texture Analysis of Brain CT Scans for ICP Prediction," in *Image and Signal Processing.* Springer, 2010, pp. 568–575.

[109] J. S. Weszka and A. Rosenfeld, "A Comparative Study of Texture Measures for Terrain Classification," *NASA STI*, vol. 76, p. 13470, 1975.

[110] R. W. Conners and C. A. Harlow, "A Theoretical Comparison of Texture Algorithms," *IEEE Transactions on Pattern Analysis and Machine Intelligence*, no. 3, pp. 204–222, 1980.

[111] F. M. Valckx and J. M. Thijssen, "Characterization of Echographic Image Texture by Cooccurrence Matrix Parameters," *Ultrasound in Medicine & Biology*, vol. 23, no. 4, pp. 559–571, 1997.

[112] R. M. Haralick, K. Shanmugam, and I. H. Dinstein, "Textural Features for Image Classification," *IEEE Transactions on Systems, Man and Cybernetics*, no. 6, pp. 610–621, 1973.

[113] J. P. Jones and L. A. Palmer, "An Evaluation of the Two-Dimensional Gabor Filter Model of Simple Receptive Fields in Cat Striate Cortex," *Journal of Neurophysiology*, vol. 58, no. 6, pp. 1233–1258, 1987.

[114] D. C. Burr, M. C. Morrone, and D. Spinelli, "Evidence for Edge and Bar Detectors in Human Vision," *Vision Research*, vol. 29, no. 4, pp. 419–431, 1989.

[115] M. Haghighat, S. Zonouz, and M. Abdel-Mottaleb, "Identification Using Encrypted Biometrics," in *Computer Analysis of Images and Patterns*. Springer, 2013, pp. 440–448.

[116] M. B. A. Haghighat, A. Aghagolzadeh, and H. Seyedarabi, "A Non-Reference Image Fusion Metric Based on Mutual Information of Image Features," *Computers & Electrical Engineering*, vol. 37, no. 5, pp. 744–756, 2011.

[117] C. Loizou, M. Pantziaris, I. Seimenis, and C. Pattichis, "Brain MR Image Normalization in Texture Analysis of Multiple Sclerosis," in *Information Technology and Applications in Biomedicine*. IEEE, 2009, pp. 1–5.

[118] J. Wright, A. Y. Yang, A. Ganesh, S. S. Sastry, and Y. Ma, "Robust Face Recognition via Sparse Representation," *IEEE Transactions on Pattern Analysis and Machine Intelligence*, vol. 31, no. 2, pp. 210–227, 2009.

[119] http://martinos.org/qtim/miccai2013/index.html, accessed: 2014-10-18.

[120] P. Gibbs, D. Buckley, S. Blackband, and A. Horsman, "Tumour Volume Determination from MR Images by Morphological Segmentation," *Physics in Medicine and Biology*, vol. 41, no. 11, p. 2437, 1996.

[121] W. Phillips II, R. Velthuizen, S. Phuphanich, L. Hall, L. Clarke, and M. Silbiger, "Application of Fuzzy C-Means Segmentation Technique for Tissue Differentiation in MR Images of a Hemorrhagic Glioblastoma Multiforme," *Magnetic Resonance Imaging*, vol. 13, no. 2, pp. 277–290, 1995.

[122] L. M. Fletcher-Heath, L. O. Hall, D. B. Goldgof, and F. R. Murtagh, "Automatic Segmentation of Non-Enhancing Brain Tumors in Magnetic Resonance Images," *Artificial Intelligence in Medicine*, vol. 21, no. 1, pp. 43–63, 2001.

[123] K. M. Iftekharuddin, J. Zheng, M. A. Islam, and R. J. Ogg, "Fractal-Based Brain Tumor Detection in Multimodal MRI," *Applied Mathematics and Computation*, vol. 207, no. 1, pp. 23–41, 2009.

[124] S. Bauer, L.-P. Nolte, and M. Reyes, "Segmentation of Brain Tumor Images Based on Atlas-Registration Combined with a Markov-Random-Field Lesion Growth Model," in *Biomedical Imaging: From Nano to Macro, 2011 IEEE International Symposium on.* IEEE, 2011, pp. 2018–2021.

[125] R. Ratan, S. Sharma, and S. Sharma, "Multiparameter Segmentation and Quantization of Brain Tumor from MR Images," *Indian Journal of Science and Technology*, vol. 2, no. 2, pp. 11–15, 2009.

[126] S. Chen and D. Zhang, "Robust Image Segmentation Using FCM with Spatial Constraints Based on New Kernel-Induced Distance Measure," *IEEE Transactions on Systems, Man, and Cybernetics, Part B: Cybernetics*, vol. 34, no. 4, pp. 1907–1916, 2004.

[127] I. Guyon and Elisseeff, "An Introduction to Variable and Feature Selection," *The Journal of Machine Learning Research*, vol. 3, pp. 1157–1182, 2003.

[128] M. L. Praneethchandran, M. Majumder, and K. Ramachandran, "Laplace and Morlet Wavelet Analysis for Gear Fault Diagnosis: A Comparative Study."

[129] I. Daubechies *et al.*, *Ten Lectures on Wavelets.* SIAM, 1992, vol. 61.

[130] R. M. Neupauer and K. L. Powell, "A Fully-Anisotropic Morlet Wavelet to Identify Dominant Orientations in a Porous Medium," *Computers & Geosciences*, vol. 31, no. 4, pp. 465–471, 2005.

[131] J.-P. Antoine, P. Carrette, R. Murenzi, and B. Piette, "Image Analysis with Two-Dimensional Continuous Wavelet Transform," *Signal Processing*, vol. 31, no. 3, pp. 241–272, 1993.

[132] P. Kumar, "A Wavelet Based Methodology for Scale-Space Anisotropic Analysis," *Geophysical Research Letters*, vol. 22, no. 20, pp. 2777–2780, 1995.

[133] R. Yu, "Theory of Dual-Tree Complex Wavelets," *IEEE Transactions on Signal Processing*, vol. 56, no. 9, pp. 4263–4273, 2008.

[134] I. W. Selesnick and K. Y. Li, "Video Denoising Using 2D and 3D Dual-Tree Complex Wavelet Transforms," in *Optical Science and Technology.* International Society for Optics and Photonics, 2003, pp. 607–618.

[135] I. W. Selesnick, R. G. Baraniuk, and N. C. Kingsbury, "The Dual-Tree Complex Wavelet Transform," *IEEE Signal Processing Magazine*, vol. 22, no. 6, pp. 123–151, 2005.

[136] C. S. Lu, P. C. Chung, and C. F. Chen, "Unsupervised Texture Segmentation Via Wavelet Transform," *Pattern Recognition*, vol. 30, no. 5, pp. 729–742, 1997.

[137] A. Materka, M. Strzelecki *et al.*, "Texture Analysis Methods–A Review," *Technical University of Lodz, Institute of Electronics*, pp. 9–11, 1998.

[138] A. Laine and J. Fan, "Texture Classification by Wavelet Packet Signatures," *IEEE Transactions on Pattern Analysis and Machine Intelligence*, vol. 15, no. 11, pp. 1186–1191, 1993.

[139] G. Chandrashekar and F. Sahin, "A Survey on Feature Selection Methods," *Computers & Electrical Engineering*, vol. 40, no. 1, pp. 16–28, 2014.

[140] N. Littlestone, "Learning Quickly When Irrelevant Attributes Abound: A New Linear-Threshold Algorithm," *Machine Learning*, vol. 2, no. 4, pp. 285–318, 1988.

[141] A. J. Grove and D. Roth, "Linear Concepts and Hidden Variables," *Machine Learning*, vol. 42, no. 1-2, pp. 123–141, 2001.

[142] T. Zhang, F. Damerau, and D. Johnson, "Text Chunking Based on a Generalization of Winnow," *The Journal of Machine Learning Research*, vol. 2, pp. 615–637, 2002.

[143] T. Zhang, "Regularized Winnow Methods," *Advances in Neural Information Processing Systems*, pp. 703–712, 2001.

[144] M. Kass, A. Witkin, and D. Terzopoulos, "Snakes: Active Contour Models," *International Journal of Computer Vision*, vol. 1, no. 4, pp. 321–331, 1988.

[145] D. J. Williams and M. Shah, "A Fast Algorithm for Active Contours and Curvature Estimation," *CVGIP: Image Understanding*, vol. 55, no. 1, pp. 14–26, 1992.

[146] K.-M. Lam and H. Yan, "Fast Algorithm for Locating Head Boundaries," *Journal of Electronic Imaging*, vol. 3, no. 4, pp. 351–359, 1994.

[147] A. A. Amini, S. Tehrani, and T. E. Weymouth, "Using Dynamic Programming for Minimizing the Energy of Active Contours in the Presence of Hard Constraints," in *Computer Vision*, 1988, pp. 95–99.

[148] N. S. Jayant and P. Noll, "Digital Coding of Waveforms: Principles and Applications to Speech and Video," *Englewood Cliffs, NJ*, pp. 115–251, 1984.

[149] N. Nabizadeh and M. Kubat, "Brain Tumors Detection and Segmentation in MR Images: Gabor Wavelet vs. Statistical Features," *Computers & Electrical Engineering*, 2015.

[150] A. Ross and A. Jain, *Multimodal Biometrics: An Overview.* na, 2004.

[151] Y. A. Zuev and S. Ivanov, "The Voting as a Way to Increase the Decision Reliability," *Journal of the Franklin Institute*, vol. 336, no. 2, pp. 361–378, 1999.

[152] N. M. Correa, T. Adali, Y.-O. Li, and V. D. Calhoun, "Canonical Correlation Analysis for Data Fusion and Group Inferences," *Signal Processing Magazine, IEEE*, vol. 27, no. 4, pp. 39–50, 2010.

[153] Q.-S. Sun, S.-G. Zeng, Y. Liu, P.-A. Heng, and D.-S. Xia, "A New Method of Feature Fusion and its Application in Image Recognition," *Pattern Recognition*, vol. 38, no. 12, pp. 2437–2448, 2005.

[154] H. Hotelling, "Relations Between Two Sets of Variates," *Biometrika*, pp. 321–377, 1936.

[155] M. Borga, "Canonical Correlation: a Tutorial," *On line tutorial http://people. imt. liu. se/magnus/cca*, vol. 4, 2001.

[156] P. Yu, D. Xu, and H. Zhou, "Feature Level Fusion Using Palmprint and Finger Geometry Based on Canonical Correlation Analysis," in *Advanced Computer Theory and Engineering*, vol. 5. IEEE, 2010, pp. V5–260.

[157] http://www.mathworks.com/help/images/registering-multimodal-mri-images.html?refresh=true, accessed: 2015-03-8.